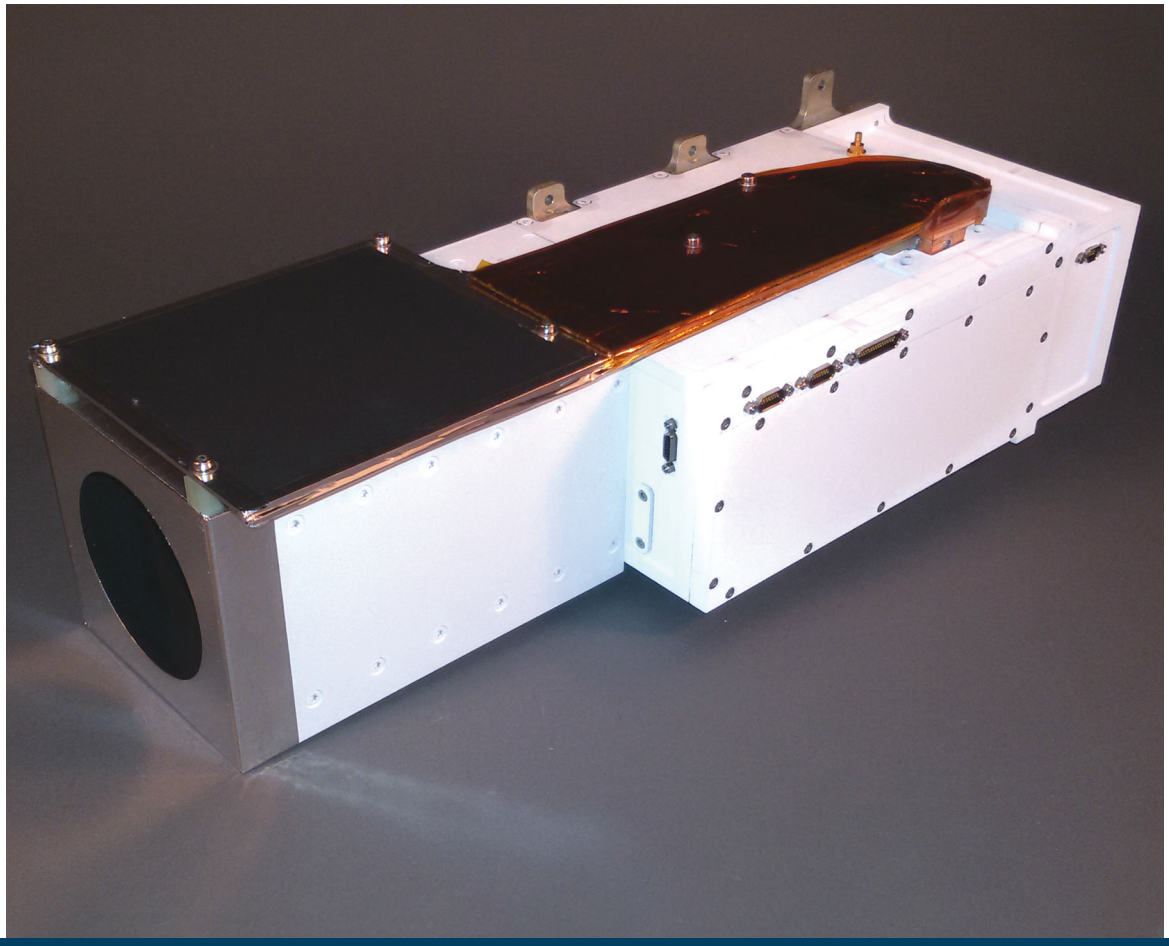

Study on a miniaturized satellite payload for atmospheric temperature measurements

Jilin Liu

Energie & Umwelt / Energy & Environment
Band / Volume 468
ISBN 978-3-95806-415-7

Mitglied der Helmholtz-Gemeinschaft

JÜLICH
Forschungszentrum

Schriften des Forschungszentrums Jülich
Reihe Energie & Umwelt / Energy & Environment Band / Volume 468

Forschungszentrum Jülich GmbH
Institut für Energie- und Klimaforschung
Stratosphäre (IEK-7)

Study on a miniaturized satellite payload for atmospheric temperature measurements

Jilin Liu

Schriften des Forschungszentrums Jülich
Reihe Energie & Umwelt / Energy & Environment Band / Volume 468

ISSN 1866-1793 ISBN 978-3-95806-415-7

Bibliografische Information der Deutschen Nationalbibliothek.
Die Deutsche Nationalbibliothek verzeichnet diese Publikation in der
Deutschen Nationalbibliografie; detaillierte Bibliografische Daten
sind im Internet über http://dnb.d-nb.de abrufbar.

Herausgeber und Vertrieb:	Forschungszentrum Jülich GmbH Zentralbibliothek, Verlag 52425 Jülich Tel.: +49 2461 61-5368 Fax: +49 2461 61-6103 zb-publikation@fz-juelich.de www.fz-juelich.de/zb
Umschlaggestaltung:	Grafische Medien, Forschungszentrum Jülich GmbH
Druck:	Grafische Medien, Forschungszentrum Jülich GmbH
Copyright:	Forschungszentrum Jülich 2019

Schriften des Forschungszentrums Jülich
Reihe Energie & Umwelt / Energy & Environment, Band / Volume 468

D 468 (Diss. Wuppertal, Univ., 2019)

ISSN 1866-1793
ISBN 978-3-95806-415-7

Vollständig frei verfügbar über das Publikationsportal des Forschungszentrums Jülich (JuSER)
unter www.fz-juelich.de/zb/openaccess.

ABSTRACT

The atmospheric temperature reflects the thermal balance of the atmosphere and is a valuable indicator of climate change. It has been widely recognized that the atmospheric gravity wave activity has a profound effect on the large-scale circulation, thermal and constituent structures in the mesosphere and lower thermosphere (MLT). Temperature distribution in this region is an essential component to identify and quantify gravity waves. Observation from remote sensing instruments on satellite platforms is an effective way to measure the temperature in the MLT region.

A miniaturized satellite payload is developed to measure the atmospheric temperature in the MLT region via observing the O_2A-band emission. Following a Boltzmann distribution, the relative intensities of the emission lines can be used to derive the temperature profile. Based on the spatial heterodyne spectroscopy, this instrument is capable of resolving individual emission lines in the O_2A-band for the spatial and spectral information simultaneously. The monolithic and compact feature of this spectrometer makes it suitable for operating on satellite platforms.

In this work, the characterization of the instrument is investigated for the purpose of simultaneously measuring multiple emission lines of the O_2A-band. The instrument is explored through a series of experimental methods, providing characteristics of the instrument and evaluation of its performance. In spatial and spectral domain, Level-0 and Level-1 data processors are developed to convert the raw data to the calibrated spectral

radiance for further temperature and gravity wave characterization.

Within this framework, the performance of the utilized detector is evaluated along with its radiation tolerance in space environment. In the processor, the detector artifacts are corrected based on the measurements in laboratory or in space. The radiometric response of the instrument is characterized on a pixel-by-pixel basis using a blackbody. An interferogram distortion correction algorithm is developed to correct for the spatial and phase distortion induced by the detector optics. Further, localized phase distortion correction is implemented to correct for the remaining phase error. Unwanted ghost emission lines are removed based on two dimensional Fourier transform. In the spectral domain, the processing steps mainly consist of wavelength calibration and instrument spectral response correction, including filter response correction and modulation efficiency correction.

As an in-orbit verification, the AtmoSHINE instrument was successfully deployed in space on 22th of December, 2018. In the first test phase, the functionality and the performance of the instrument in space were verified. The detector dark current measurement in orbit is consistent with the ground-based results. Based on the the calibration procedures and the developed data processing algorithms, the O_2A-band emission lines can be successfully resolved. A cross-verification of the AtmoSHINE limb radiance profile with other satellite payload measurements indicates that the radiometric performance of the instrument is within the expectation.

The retrieved temperature parameters are studied with respect to different number of samples and different objective functions in the optimization. This work verifies the ability of the instrument to derive the atmospheric temperature in the MLT region and its potential application in gravity wave detections.

Contents

Chapter 1

Introduction

1.1 Research background

1.1.1 Atmospheric structure

Looking at the Earth from outer space, the atmosphere shall be compared to a light transparent veil in an uninterrupted movement. The environment for most of the human activities so far is limited to the bottom layer of the atmosphere, the upper edge of the atmosphere is connected to the space. The atmosphere protects the Earth's surface from direct exposure to solar radiation, especially ultraviolet (UV) light. It also reduces the occurrence of extreme temperature difference throughout the day. The composition of the atmosphere, the temperature and other physical properties vary significantly with height. According to the temperature distribution, the atmosphere is generally divided into different layers, namely troposphere, stratosphere, mesosphere and thermosphere (Figure 1.1). The boundary regions that act as the barriers in between are called the tropopause, stratopause and mesopause, where the vertical temperature gradient changes its sign.

The troposphere, according to its Greek word *tropein*, is the region

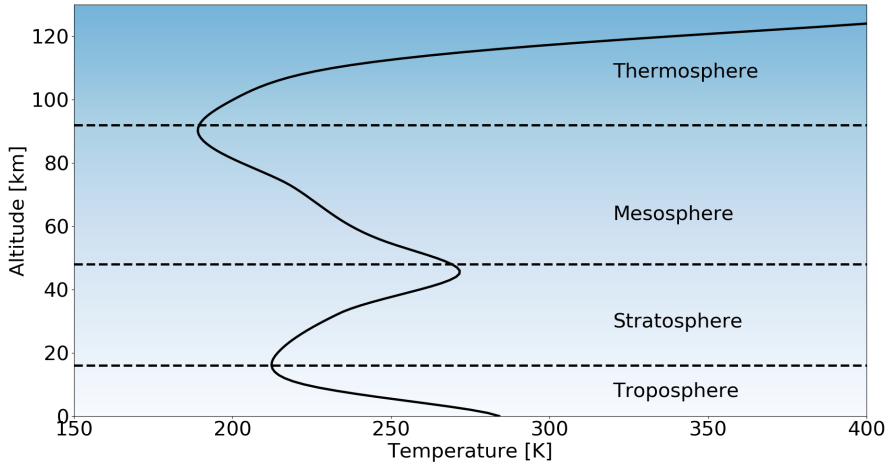

Figure 1.1: Atmosphere temperature structure up to 130 km. The profile is extracted from the MSIS model at 40°N 60°E on Mar 22, 2012.

with the most frequent mixing activities. This layer contains approximately three-quarters of the total air mass and almost all of the water vapor and aerosols. The upper bound of the troposphere changes with latitude and season: the troposphere extends from the Earth surface up to around 8 km in the polar regions and 18 km in the tropics. In this layer, the decreasing temperature with the increasing height is mainly due to the adiabatic cooling effect with a lapse rate of about -6.5 K/km.

The stratosphere extends from the upper tropopause to an altitude of about 50 km. The airflow in this region is very stable, no strong vertical convective activity happens. The mixing effect between the troposphere and the stratosphere is also very weak. In the stratosphere, the water concentration drops rapidly due to the "water trap" effect induced by the low temperature in the tropopause region. The gradual temperature increase with height is mainly associated with the absorption of ultraviolet solar radiation by ozone molecules, the ozone mixing ratio profile has its maximum around 30 to 35 km.

The mesosphere covers an altitude range of around 50 - 85 km, the temperature is again continuously decreasing and the minimum temperature is achieved at the top of this layer. As the temperature decreases with the increasing altitude, the mesosphere supports strong motions in the vertical direction. Since the atmospheric density of the mesosphere is very low, its thermal structure is strongly influenced by solar UV radiation absorption of ozone and oxygen for the heating effect, and the infrared radiation emitted by carbon dioxide for the cooling effect.

Above the mesosphere is the thermosphere, this layer extends up to 500-600 km altitude. The gases in this layer are partly ionized due to the absorption of short wave (<0.175 μm) solar UV radiation by oxygen and nitrogen molecules. The air in this area is extreme sparse, therefore the thermosphere temperature mainly describes the kinetic energy of the molecules and atoms. Due to the absorption effect and the low density, its temperature can change significantly, sometimes several hundred Kelvins during the day.

1.1.2 Remote sensing of the Earth atmosphere

Remote sensing of the atmosphere is the key to better understanding atmospheric processes, which are important for weather and climate. The term *remote sensing* refers to the technique of collecting information about the objects at certain distance. Within this concept, the information of the atmosphere is propagated to the instrument by means of electromagnetic radiation. Therefore, deriving the atmospheric information from the radiation characteristics measured by the instrument requires a retrieval process. Passive remote sensing technique detects energy that is naturally available, such as the radiation from a natural source (sun, moon, stars) after reflection or scattering, or the detectable energy that is naturally emitted by the atmosphere (e.g. thermal infrared). An active remote sensing instrument emits radiation (e.g. laser) toward the target to be investigated, the reflected radiation is then detected and measured by the sensor.

The remote sensing technique can be carried out on different platforms, e.g. ground, rocket, balloon, aircraft and satellite. Ground based measurements are taken near to the location of the observed targets and typically offer continuous observations with good temporal resolution (*Wang*, 2010; *Kalicinsky et al.*, 2016; *Melo et al.*, 2001). However, ground-based observations lack of providing measurements of atmospheric variables over the ocean and is only rarely available in rural regions. Due to the scattering effect of sunlight some ground based optical instruments are also restricted by the clear-sky condition during the observation at nighttime.

Sounding rockets and balloons are important tools for atmospheric research, they provide the unique access for in-situ measurements in the height range between 25 and 150 km (*Offermann*, 1987; *Kokin and Lysenko*, 1994; *Barth*, 1966; *Smit et al.*, 2007). These experiments are suitable for addressing atmospheric processing on small spatial scales. The local snapshot property makes these measurements a natural complement to the validation and co-analysis of model calculation and satellite measurements. High flying balloons cover a broad range of altitudes for the atmospheric measurements, especially in the 22-40 km region, which is higher than the altitude reached by a normal aircraft (*Mauersberger*, 1981; *Hofmann et al.*, 1990; *Smit et al.*, 2007).

Airborne remote sensing can offer very high spatial resolution images during a period of time (*Riese et al.*, 2014). Manned and increasingly unmanned aircraft, with their ability to maneuver and cruise over an area, can provide much denser spatial and temporal coverage (*Ungermann et al.*, 2011; *Kaufmann et al.*, 2015). The maintenance of sensors and the change of configuration can easily be made on aircraft platforms. The coverage area is smaller compared to space-borne instrument, and the cost per unit area of ground coverage is relatively high.

As satellite technology becomes more reliable and less cost prohibitive, remote sensing of the atmosphere from a satellite platform is becoming a feasible opportunity. Depending on direction and viewing geometry, the spatial resolution of a space-borne remote sensing instrument in the

vertical is often limited to the range of kilometers. In return, the payload on board a satellite has vast potential. High resolution global coverage can be achieved within relatively short time. Geostationary satellites offer high temporal resolution meanwhile the global coverage ability is limited, satellites on low earth orbits (LEO) can provide opportunity for twice-daily sampling globally.

Over the past decades, many satellite-borne instruments aimed to measure the Earth's atmosphere. The WINDII instrument (1991-2003) on board the Upper Atmosphere Research Satellite (UARS) measured the atmospheric wind, temperature and airglow lines between 80 and 300 km utilizing the phase stepping Michelson interferometry technique (*Shepherd et al.*, 1993). The SABER instrument (2001-) on the Thermosphere Ionosphere Mesosphere Energetics Dynamics (TIMED) satellite measures the atmosphere using multiple channel broadband limb-scanning infrared radiometer in the spectral range between 1.27 μm and 17 μm, providing vertical profile measurements of temperature and key species (*Russell et al.*, 1999). The primary mission goal of the SCIAMACHY spectrometer (2002-2012) aboard ESA's ENVIronmental SATellite (ENVISAT) was to perform global measurements of trace gases covering the spectral range from 240 to 1700 nm, from the troposphere to the mesosphere (*Bovensmann et al.*, 1999). Other satellite payloads like the High Resolution Doppler Imager (HRDI) (1991-2005) and the Optical Spectrograph and InfraRed Imager System (OSIRIS) were also launched ten or twenty years ago and provided useful data for atmospheric studies.

As the lifetime of these payloads have come or will come to end, a gap in the atmospheric observation, especially in the mesosphere and lower thermosphere (MLT) region, will occur in upcoming years. In less than a decade, small satellite missions play an increasingly compelling role in space-based scientific programs, especially the satellite complied with CubeSat standard (*Mehrparvar et al.*, 2014). The ongoing miniaturization techniques of optical and electronic parts and the use of Commercial-off-the-shelf (COTS) components enable tailor scientific instruments to be implemented on such platform (*Selva and Krejci*, 2012). Advantages in

terms of overall low cost, mission flexibility and rapid deployment into space allow more advancing investigations to be completed under reasonable cost budget. In this regard, this type of satellite instruments opens a new path toward space exploration (*Norton et al.*, 2014).

1.2 Instrument introduction

1.2.1 AtmoSHINE for mesospheric temperature measurements

Temperature trends in the mesosphere have gained increasing attention in recent years since there is substantial evidence that the temperature variation in this region is much larger compared to the variation in the troposphere and stratosphere. The MLT region is known as the coldest region in the terrestrial atmosphere, where the temperature gradient changes from negative to positive at the mesopause. Due to the upwelling air induced adiabatic cooling in the summer season and the downwelling air induced adiabatic heating, the summer mesopause is considerably cooler than the winter mesopause. The dynamic processes play an import role in governing the thermal structure in this regions.

In the mesosphere, the summer-to-winter pole circulation is driven by gravity waves that propagate from the troposphere into the mesosphere where the momentum and energy are deposited due to convective instabilities. As one of the least explored dynamical process in the middle and upper atmosphere for climate modeling, the gravity wave characteristics can be estimated by measuring perturbations of the mean atmosphere. Popular parameters used for the gravity wave estimation are the temperature, pressure, wind, airglow, etc. The most popular measurement technique to observe vertically resolved temperature and gravity wave parameters globally is limb sounding from LEO satellites.

The utilization of O_2A-band emissions centered around 762 nm is

considered to be a suitable way of obtaining the MLT temperature (*Ortland et al.*, 1998; *Sheese et al.*, 2010). The radiation stems from an altitude range of about 50-130 km during daytime and 85-102 km during nighttime. Since the relative intensities of the emission lines follow a Boltzmann distribution (Figure 1.2), their corresponding ratios can be used to derive the kinetic temperature without strict radiometric calibration. These emissions are located at near infrared region, which can be measured by silicon based CCD or CMOS detectors, therefore no active cooling equipment is required. This detection technique simplifies the instrument design considerably and enables the deployment of such a payload on a small satellite platform.

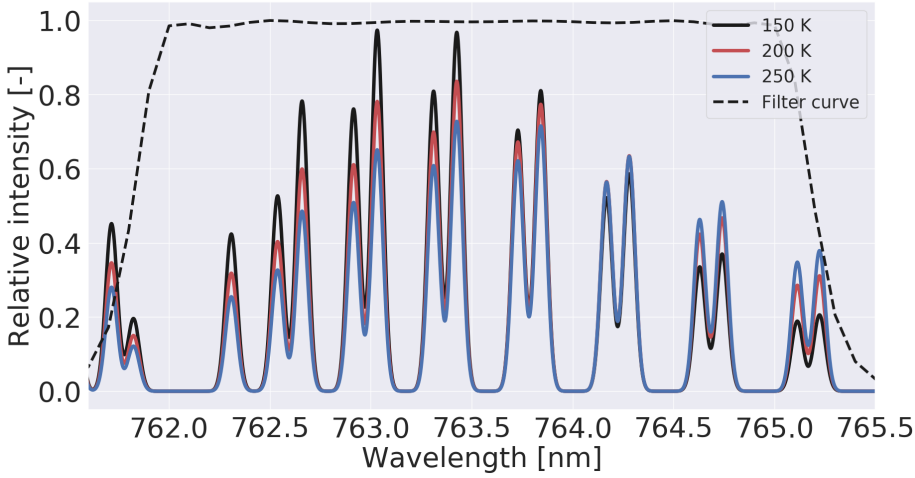

Figure 1.2: Part of O_2A-band fine-band structure at different temperatures. Six emission lines between 763.3 nm and 764.3 nm are primarily measured by the AtmoSHINE instrument for the temperature retrieval. Two emission lines inside one pair share similar temperature dependency. The theoretical bandpass filter curve provided by the manufacturer shows a relative response change in this region.

Based on this measurement principle, a small limb sounder for the

observation of the O_2A-band is developed, namely the Atmospheric Spatial Heterodyne Interferometer Next Exploration (AtmoSHINE), to derive temperatures in the MLT region (Figure 1.3, (*Kaufmann et al.*, 2018)). The instrument is developed jointly by the Research Center Juelich (FZJ) and the University of Wuppertal (BUW) in cooperation with the Max Planck Institute for the Science of Light (MPL) and the York University, Canada. Serving as an in-orbit verification to test the functionality and to verify the performance in space, AtmoSHINE is the precursor mission for a constellation of these instruments. The AtmoSHINE instrument combines the advantages of three technologies, the Michelson interferometer, field-widening of the Michelson interferometer and spatial heterodyne spectroscopy (SHS).

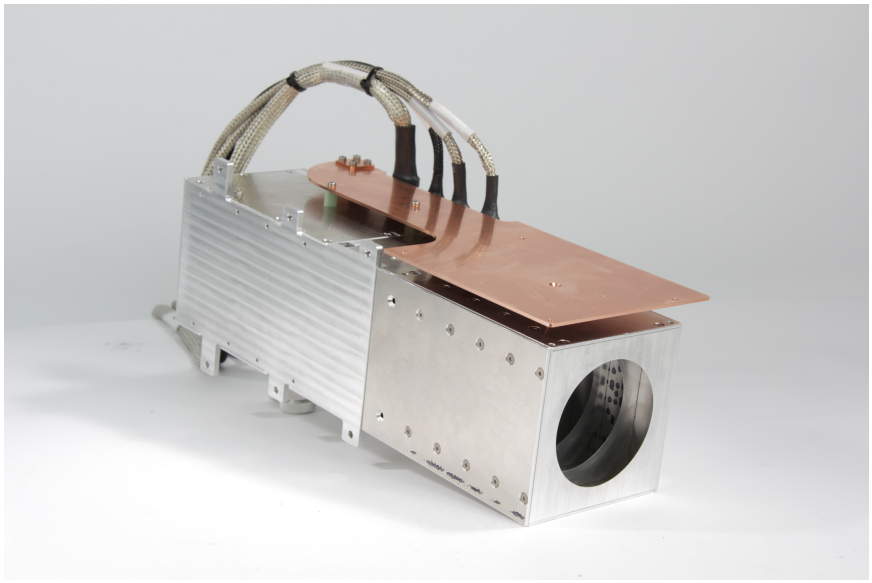

Figure 1.3: AtmoSHINE flight model.

Following the incoming light, the payload consists of a baffle, a small optical bandpass filter, a fore-optics, an SHS, a camera optics, and a CMOS detector, as displayed in Figure 1.4. The payload collects lights

emitted from a solid angle of 1.3 degree from the Earth limb, which corresponds to a vertical range of around 50-130 km as seen from 1000 km altitude orbit (Figure 1.5). Together with the optical bandpass filter, the stray light baffle of the system protects the instrument from unwanted emissions. The purpose of the front optics is to image a scene at the Earth limb onto the gratings. Given the assumption that the intensity fluctuations in the horizontal direction are small compared to the modulation depth of the interferogram, which is valid in atmospheric limb sounding, the gratings are oriented to allow the interferogram to be spanned over the horizontal direction. The detector optics images the gratings onto the focal plane of the two dimensional detector. The image recorded by the detector contains the spatial information of the atmosphere in both dimensions, meanwhile the fringe patterns are modulated in the horizontal direction.

To fulfill the scientific objectives, the diffraction gratings and the tilt angle of the SHS in the current instrument are designed to observe the 762 nm to 764 nm spectral region with a spectral resolving power of more than 10,000. The spectral resolution is large enough to distinguish individual emission lines of the O_2A-band. Therefore, the vertical profile of the emission spectrum can be obtained by a single interferogram without time delay or moving parts. Detailed specifications regarding the instrument are listed in Table 1.1 (*Kaufmann et al.*, 2018).

1.2.2 SHS technology

Over the past two decades, there has been an increasing interest in developing and applying the SHS technique. Originally proposed by Pierre Connes in 1958 (*Connes*, 1958), this kind of spectroscopy comes into vogue in recent times due to the development of two dimensional detector arrays and optical materials. Utilizing the field-widening technique, the throughput is typically more than 2 orders of magnitude larger than for typical grating spectrometers of the same size. The SHS has been successfully demonstrated for a varity of application in atmospheric meas-

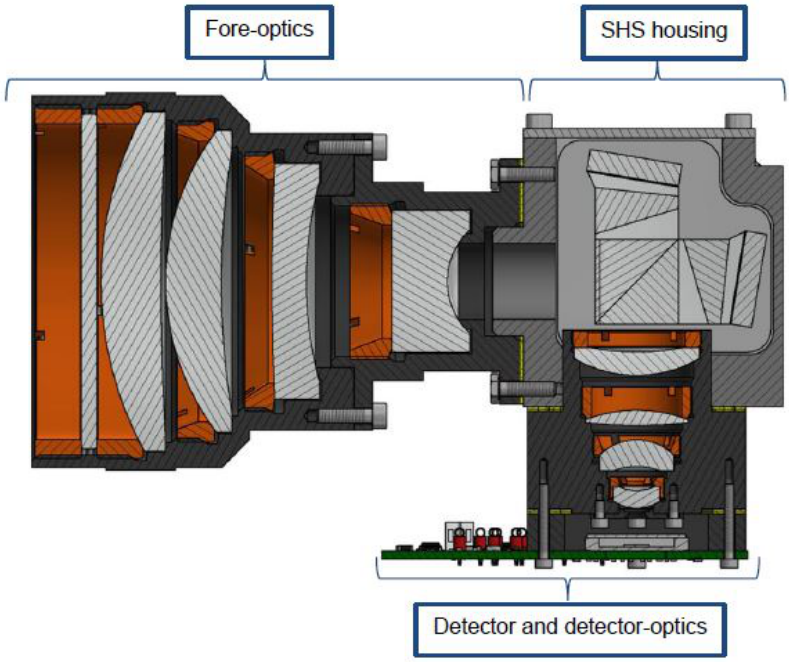

Figure 1.4: AtmoSHINE optomechanical components layout, including the filter, the fore optics, the SHS, the detector optics, and the detector.

urements, e.g. the Spatial Heterodyne Imager for Mesospheric Radicals (SHIMMER) for hydroxyl (OH) measurements (*Harlander et al.*, 2003), the Spatial Heterodyne Observations of Water instrument (SHOW) for water vapor measurements (*Lin et al.*, 2005) as well as the Doppler Asymmetric Spatial Heterodyne (DASH) (*Harlander et al.*, 2010) for wind measurements.

In general, the SHS utilizes the two-beam Michelson interferometric spectroscopy with the mirrors in each arm replaced by tilted diffraction gratings. As such, it provides high resolution for simultaneously observing multiple emission lines. The field-widened prisms configuration of these instruments allows the system throughput to be significantly in-

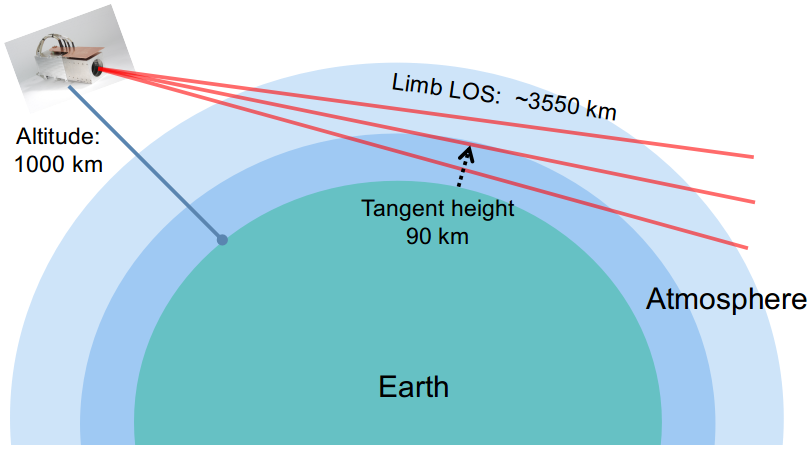

Figure 1.5: A sketch of the AtmoSHINE limb sounding configuration at a 1000 km altitude. Based on the spherical shape of the Earth (radius of 6378 km), the limb LOS is about 3550 km and the tangent height is about 90 km.

creased. The monolithic and compact feature of this spectrometer makes it suitable for operating on airborne and spaceborne platforms in many studies. Combined with modern 2D focal plane array, it provides a compact system to image multiple spectra over different altitudes in a single frame.

A schematic diagram of a field-widened SHS system is shown in Figure 1.6. Wavefronts coming into the system are firstly split into two arms, after which these two diffracted wavefronts are recombined at the detector plane. The incident beams are heterodyned by a reference wavenumber, the Littrow wavenumber σ_L, which thereby generates a Fizeau fringe pattern. The Littrow wavenumber can be determined by the following grating equation (*Cooke et al.*, 1999):

$$\sigma_L = \frac{m}{2d \sin\theta} \tag{1.1}$$

Table 1.1: **The properties of designed and utilized instrument components.**

Component	Item	Value
Filter	Wavelength range	761.9-765.3 nm
	Central wavelength	763.6 nm
	Transmission	> 93% abs @ 762.6-764.6 nm
Fore optics	Field of view	$\pm 0.65^{\circ}$
	Aperture diameter	66 mm
	Focal length	136 mm
	Etendue (circular aperture)	0.014 cm^2 sr
	Etendue (rectangular aperture)	0.01 cm^2 sr
SHS	Littrow wavelength	761.8 nm
	Littrow angle	27.2°
	Grating groove density	1200 lines mm^{-1}
	Grating area	13x13 mm^2
	Resolving power	~16800
	Diffraction order	1
Detector optics & detector	Numerical aperture (obj. space)	0.12
	Magnification factor	0.55
	Focal length	28mm
	Utilized detector pixel number	800 × 800 pixels
	Detector pixel size	5.04×5.04 μm^2

where $\frac{1}{d}$ is the grating groove density, m is the diffraction order and θ is the corresponding Littrow angle. Accordingly, the resolving power R of an SHS can be represented as:

$$R = \frac{2W}{d} = \frac{4W\sigma \sin\theta}{m} \tag{1.2}$$

with W the width of the illuminated area on the gratings. The wavenumber dependent spatial frequency f can be expressed as (*Roesler and Harlander*, 1990):

$$f = 4(\sigma - \sigma_L)\tan\theta \tag{1.3}$$

with σ the wavenumber of the incident light. The recorded interferogram

as a function of detector position x is given by:

$$I(x) = \int_{-\infty}^{\infty} B(\sigma)\left[1 + V(x,\sigma)\cos\left(2\pi f x + \varphi(x,\sigma)\right)\right] d\sigma \tag{1.4}$$

where $B(\sigma)$ is the spectral radiance of the incident emission line, $V(x,\sigma)$ is the instrument visibility function, $\varphi(x,\sigma)$ represents the additive phase distortion term associated with the emission wavenumber and the position in the localization plane.

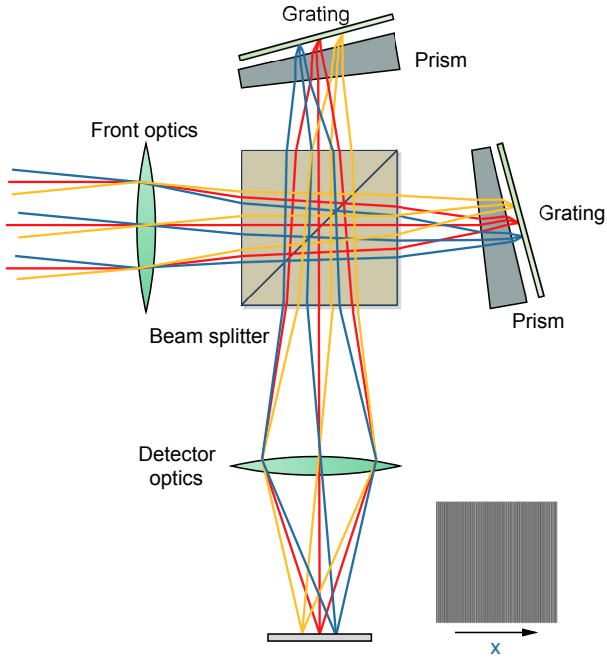

Figure 1.6: Schematic of a field-widened SHS concept in focused configuration.

1.2.3 Data processing

Based on the SHS technology, the AtmoSHINE instrument is a spatial modulated Fourier transform spectrometer. The interferograms have to be transformed to the calibrated atmospheric radiance spectra, which can then be used for various inversion models to compute vertical profile of atmospheric temperature, atmospheric composition and, as a follow-on product, gravity wave parameters. From the raw interferograms to the final parameters, the AtmoSHINE data products are processed at various levels ranging from level-0 to level-2, as indicated in the flowchart shown in Figure 1.7. At higher levels, data are converted into further formats.

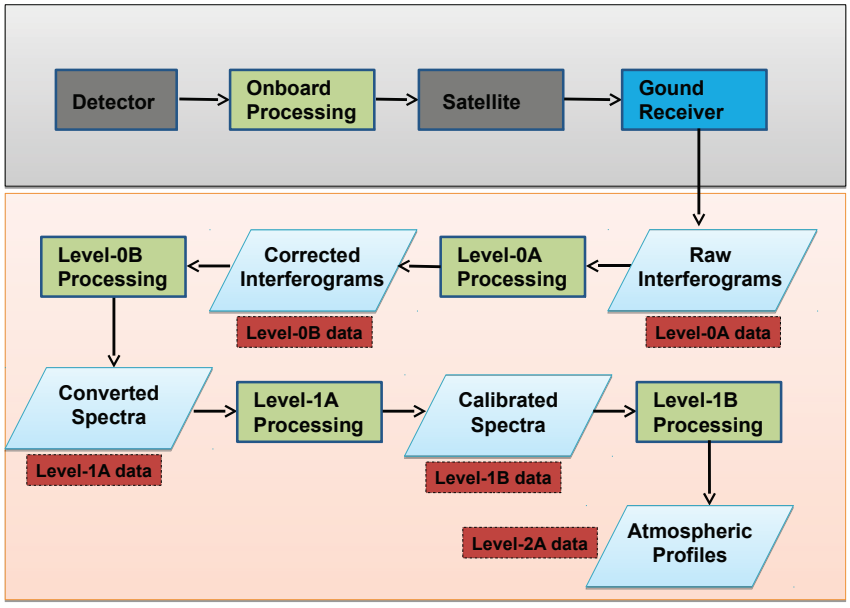

Figure 1.7: AtmoSHINE data processing chain from Level-0 to Level-2. Upper colored region indicates the processing on the satellite part, lower colored region includes the processing on ground.

The processing steps up to Level-2 is separated into two major parts, which are distinguished based on the procedures in spatial and spectral domains. The obtained images on the detector are firstly readout according to the configured region of interest (ROI) and binning factor. Along with the instrument housekeeping data and the registered data from satellite bus, the raw images are transmitted to the ground receiver. Ground segment decodes the data and converts them into Level-0A data products.

The level-0A processing includes the correction procedures implemented on the interferograms in spatial domain. Detector artifacts like offset and dark current are corrected based on the measurements in the laboratory or in space. Next, the interferogram spikes, which can be caused by detector hot pixel and cosmic radiation (or stars) , are replaced by the median values of their neighboring pixels. The non-uniformity of the instrument sensitivity response is corrected on a pixel basis in the radiometric calibration. Optical distortion correction and phase correction techniques are utilized to provide an undistorted interferogram without deviating the altitude information. The last procedure in spatial domain is to remove the ghost emission lines from other side of the Littrow configuration. After applying these techniques, the raw interferograms are converted into Level-0B products.

The Level-1A data is obtained via Level-0B processing, which transforms the interferograms to the corresponding spectra. Level-1B data includes the calibrated spectral information obtained by Level-1A processing. In spectral domain, the Level-1A processing mainly consists of instrument spectral response correction and wavelength calibration. The final Level-1B data is supplemented with ancillary data including position, attitude, altitude information from the satellite bus. Level-1B processing retrieves the atmospheric parameters from the emission spectra, the Level-2 data mainly consists of the retrieved atmospheric parameters, which are later mapped on uniform space-time grid scales. This thesis primarily discusses the development of the algorithms for the Level-0 and Level-1A processing chain. The research structure is shown in Figure 1.8 including some highlighted categories.

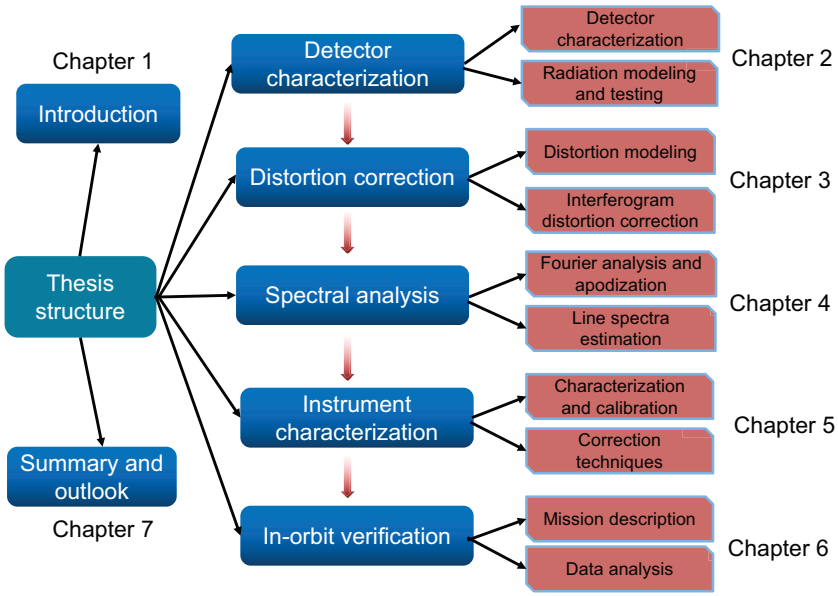

Figure 1.8: Structure of the thesis with some highlighted sections.

Chapter 2

Detector characterization

This chapter presents the characterization and analysis of the COTS CMOS detector utilized in the AtmoSHINE instrument for the experiment. To evaluate the performance of the selected CMOS detector, a series of tests were performed. The temperature dependent dark current, the readout noise and the system gain are determined, which are provided for the subsequent system performance evaluation and data processing. A case study is established to simulate the space radiation effect of high-energetic particles to determine the needed shielding thickness of the instrument. The effect of radiation damage on the CMOS image sensors is investigated using a Co-60 Gamma radiation source.

2.1 CMOS and CCD detectors

The rapid growth of the research and development on CMOS image sensors over the last decades offers desirable characteristics for a number of space-based scientific applications, with low power consumption, low cost and high levels of integration compared with conventional CCD detectors (*Magnan*, 2003; *Holst and Lomheim*, 2007). The CMOS detector does not suffer from charge transfer degradation from displacement

damage since, unlike in the case of a CCD detector, the pixels can be addressed directly. Nevertheless, the CMOS image sensors, especially the COTS parts, currently lack the competitive performance in detector dark current, noise and uniformity compared with customized CCD sensors.

During a space mission the detectors are damaged by cosmic particles or rays, which leads to the performance degradation or even functional failure. Although the radiation hardness technologies of commercial CMOS have been evolving rapidly over the past decades (*Derbenwick and Gregory*, 1975; *Calin et al.*, 1996), the performance of typical COTS products is still not guaranteed since this parameter is generally not characterized by the manufacturers (*Lacoe et al.*, 1998; *Faccio*, 2000; *Felix et al.*, 2006). Therefore, a radiation test on the COTS CMOS detector is compulsory in the instrument verification period of the space mission.

2.2 Electronic and detector configuration

The payload readout electronics developed at Central Institute for Engineering, Electronics and Analytics, Electronic Systems (ZEA-2) of the FZJ consist of two boards: the proximity electronics (PXE) for directly interfacing to the detector ICs and the front-end electronics (FEE) with an embedded controller with Advanced RISC Machines (ARM) cores and field-programmable gate array (FPGA) fabric. The FEE serves as the central processing system of the readout system. In addition, a power supply unit (PSU) is provided to fulfill grounding isolation requirements. The tasks are to handle signals from the control unit (CU) of the satellite bus to start the measurement, to acquire detector data, to provide data preprocessing (data binning) and to transfer data to the CU. A block diagram for the readout electronics is shown in Figure 2.1.

A scientific CMOS (sCMOS) imaging detector builds the baseline for the camera system of the experiment. After investigating several vendors for scientific CMOS sensors, a silicon-based CMOS image sensor from Fairchild Imaging (HWK1910A) is chosen for its low noise and high dy-

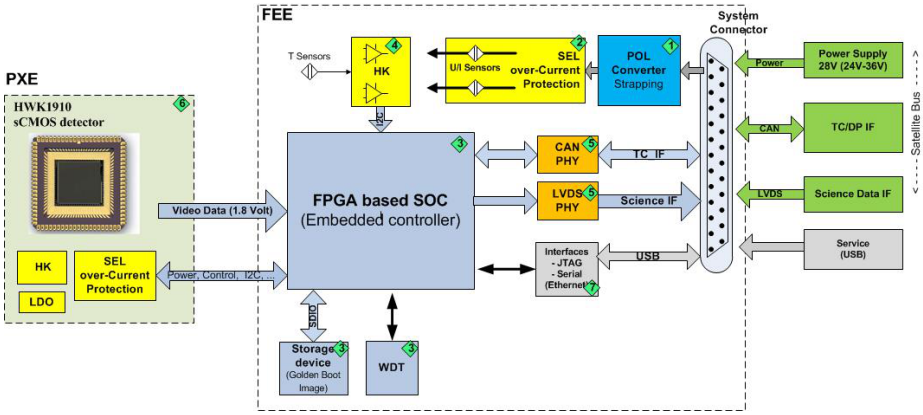

Figure 2.1: Block diagram AtmoSHINE readout electronics

namic range. The quantum efficiency at around 760 nm, which is the wavelength for the measurements, is about 40%. This sensor has common programmable region of interest (ROI) registers, on-chip digitizers (ADCs) and a digital interface to the readout electronics. The pixel size of the detector is 5 μm x 5 μm, and the ideal number of pixels 1920 x 1080. The detector main specifications provided by the manufacturer are summarized in Table 2.1.

Table 2.1: **HWK1910A CMOS detector specifications**

CMOS	HWK1910A
Pixel count	1920 Horizontal $\times$ 1080 Vertical pixels
Pixel size	5.04 μm $\times$ 5.04 μm
Active area	9676.8 μm (H) x 5443.2 μm (V)
Read noise	1 electron (rms)
Dark current	$< 20\ e^-$ /pixel/s dark current at 20°C
Gain	$0.42 e^-$/count
Quantum efficiency	40% @ 760nm

Among various operating modes of the detector, the uncalibrated mode and the manual calibration mode are investigated in this study. The

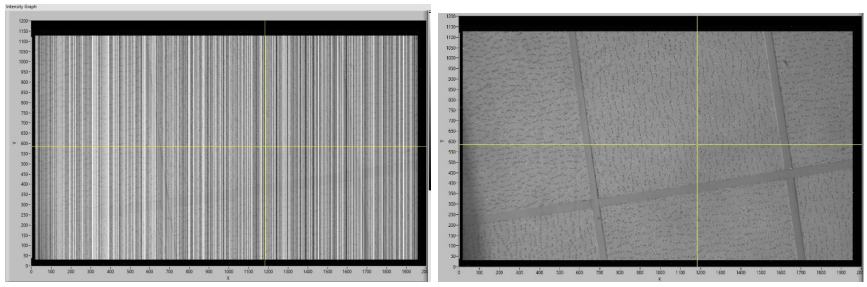

(a) Uncalibrated detector test image (b) Calibrated detector test image

Figure 2.2: Uncalibrated (left) and calibrated (right) detector test images in the laboratory.

switch between these two operating modes can be realized via sending a telecommand to the instrument during operation. For the manual calibration mode, the sensor goes through an internal offset and column amplifier calibration cycle to compensate for the different performance of the amplifiers and for temperature drift over time. Figure 2.2 shows the uncalibrated and calibrated detector test images, where the correction of column-wise amplifier variation is clearly visible. The manual calibration mode offers correction of the spatial variation of pixel output.

2.3 Detector performance tests

2.3.1 Detector dark current

The HWK1910A device was tested in a thermal chamber to characterize the detector dark current distribution under different conditions. Several temperature sensors were set inside the chamber and on the detector to monitor the detector and environmental temperatures. Temperature dependency of the detector dark current is characterized based on the measurements with different integration times and temperatures. During the

test, the detector dark current was measured between -14°C and +25°C.

Figure 2.3 displays the dark current profile as an ensemble average of the entire array. According to the experimental results (upper plots in Figure 2.3), the amount of dark current scales linearly with integration time under each tested temperature condition. A slightly larger uncertainty measured at higher temperatures may indicate an increase of detector hot pixels as a non-linear effect. Based on the linear integration time dependency and the exponential temperature dependency of the detector dark current, a model was established to predict the detector dark current for each pixel, as shown in lower plot in Figure 2.3 for the averaged results on the detector array. According to the fitted parameters, the detector dark current doubles for every 6.7±0.2 K temperature change.

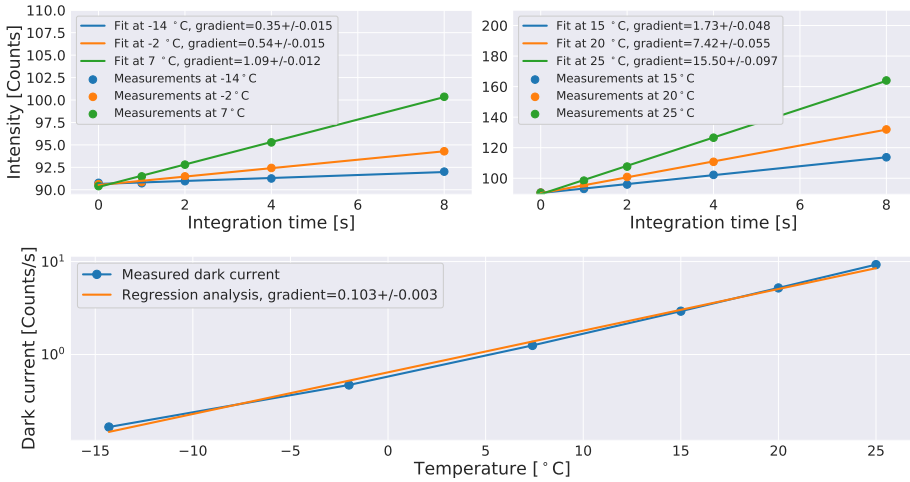

Figure 2.3: Upper plots: measured signal intensity between -14°C and 25°C under different integration time. Lower plot: temperature dependency of the detector dark current and the corresponding exponential fit, based on the gradients obtained in upper subplots.

2.3.2 System gain and readout noise

The detector system gain usually describes the conversion ratio from the number of electrons into Analog-Digital Units (ADUs). This parameter can be estimated from the shot noise characteristic associated with the signal intensity, namely the mean-variance method (MVM) or the photon transfer curve (*Beecken and Fossum*, 1996; *Stark et al.*, 1992). The Poisson distribution of the shot noise gives the shot noise variance σ^2_{shot} which is equal to the averaged signal intensity $\overline{S}$ in ADUs. The total noise variance σ^2_{noise} can therefore be expressed as:

$$\sigma^2_{noise} = G^2\sigma^2_{shot} + \sigma^2_{readout} = G\overline{S} + \sigma^2_{readout} \tag{2.1}$$

where G is the system gain in ADUs/electron and $\sigma^2_{readout}$ represents the readout noise variance which has zero mean. Accordingly, the linear fit of the total noise variance against the averaged signal intensity S gives the conversion gain G and the offset that corresponds to the readout noise variance.

For this measurement a light source was installed inside the thermal chamber. The detector was cooled down below -20°C to minimize the detector dark current during the experiment. The amount of photons recorded by the detector was controlled by adjusting the integration time. From the linear regression analysis the distribution of the estimated system gain under different integration times was obtained, as shown in Figure 2.4. This estimation indicates that the average conversion ratio is about 2 ADUs/electron and the corresponding readout noise is about $1e^-$, which are close to the detector specifications provided by the manufacturer.

Another method to characterize the detector readout noise is to determine the standard deviation of various read-outs at “zero” integration time (Figure 2.5). This method does not require a light source. For the detector analyzed in this study, the median value is approximately $0.9e^-$ on each pixel, which fits to the results from MVM method. The corresponding root mean square (rms) is $3.9e^-$, which is larger than the given

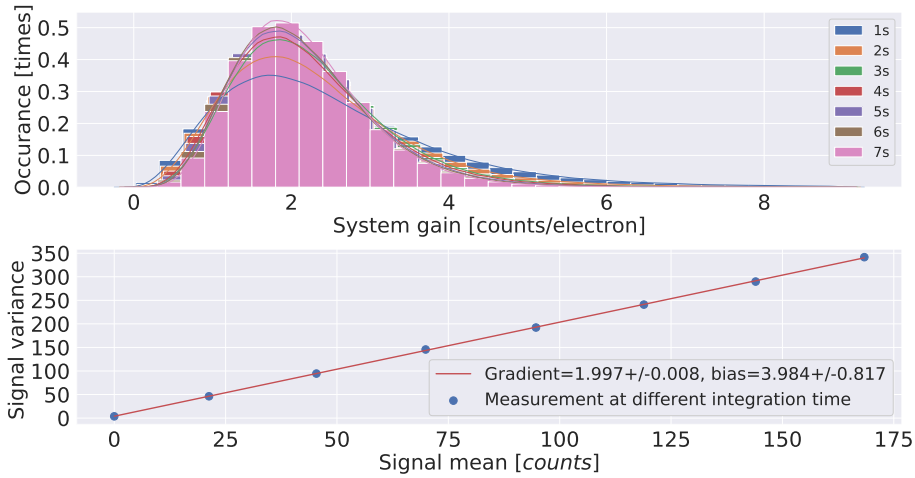

Figure 2.4: Estimation of system gain. Upper plot: histogram of the system gain for different pixels obtained with different integration times. Lower plot: linear regression analysis, the gradient and the bias represent the system gain and readout noise, separately.

information.

2.3.3 Detector fixed pattern

The detector fixed pattern noise (FPN) describes a spatial variation in pixel outputs of an image under uniform illumination conditions. For CMOS detectors that use column amplifiers configuration, the FPN appears as ”stripes” on the readout images. The manual calibration mode of the detector allows the correction of this pixel gain variation on the whole detector plane, as shown in Figure 2.2(b). This operation is achieved by injecting electrons into detector pixels specifically reserved for this calibration purpose. The manual calibration mode (Figure 2.2(b)) will change the pixel offsets slightly in each power loop, since this procedure is also bound up with the environmental conditions.

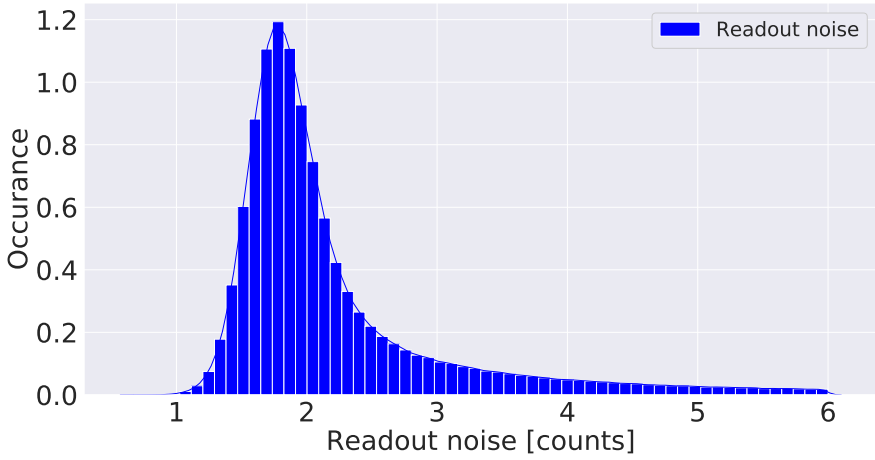

Figure 2.5: Detector readout noise estimation based on multiple frames readout under 1ms integration time. The detector was cooled down to -20°C in the thermal chamber.

The investigation of the pixel offset variation, which is also called the detector fixed pattern, is achieved by running several power loops. The detector integration time was set to be 1ms such that the dark current is negligible for the analysis. During each loop, frames were recorded every 5 seconds. As illustrated in Figure 2.6(a), the fixed pattern in loop 1-4 changes slightly, meanwhile the result from the 5th loop shows relative larger deviation than the first 4 loops, which is possibly associated with the environmental temperature at that time. For an accurate instrument radiometric calibration, the detector pixel offsets need to be measured and subtracted each time when the instrument is switched on, simply by taking images with the lowest integration time.

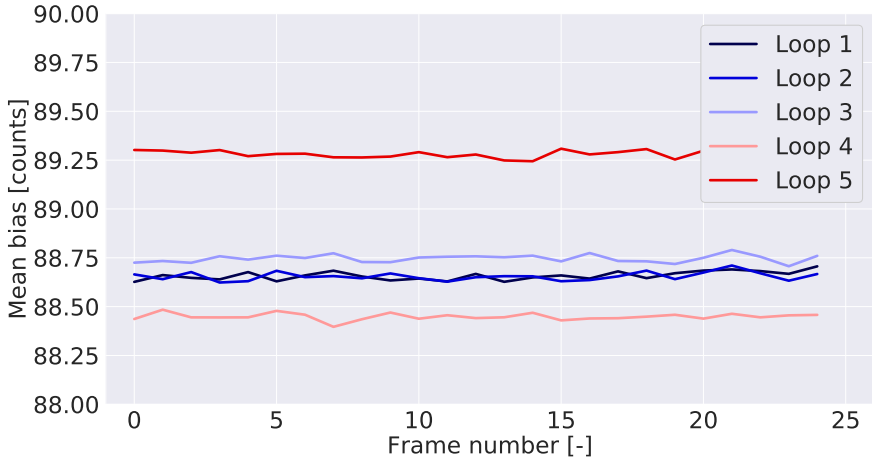

(a) Mean value of detector fixed pattern

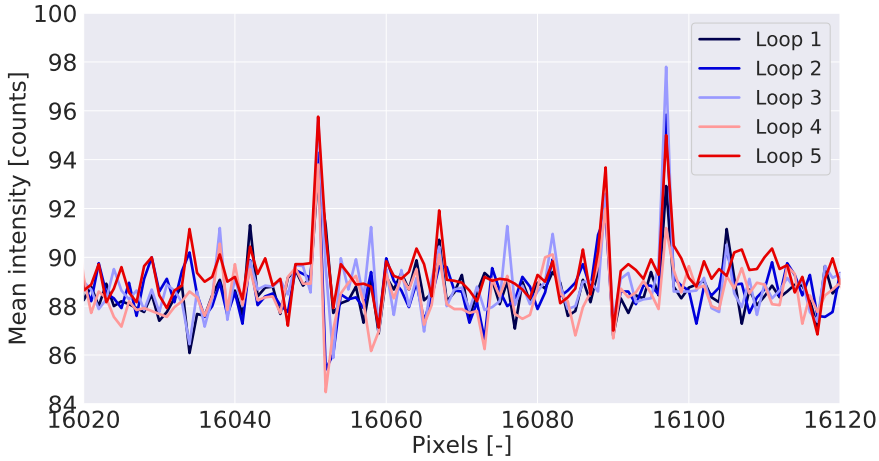

(b) Detector fixed pattern for some pixels

Figure 2.6: (a): detector mean fixed pattern with the lowest integration time (1ms) from 5 power loops. (b): detector fixed pattern at certain detector region. Loop 1-4 were measured with 3 minutes in between, while the 5th loop was measured 0.5 h after the 4th loop.

2.4 Radiation test

2.4.1 Radiation environment modeling

The ionizing effect in the space radiation environment can cause degradation and failure of electronic devices, especially when using optoelectronic detectors. Basically the radiation effects consist of two parts: the single event effect (SEE) and the total ionizing dose (TID). The SEE induced by high energy particles will result in device logic failure as an instantaneous failure mechanism, whereas the TID will make cumulative long term ionizing damage on the electronics for low Earth orbit (LEO) mission due to protons and electrons exposure. These particles and rays create shifts in threshold voltages and leakage currents, therefore causing permanent radiation damage to Silicon devices.

The increase of dark current is one of the most critical effects on the detector degradation in space radiation environments. The growth of the CMOS dark current under radiation is mainly caused by generated interface traps and bulk defects, producing additional surface leakage current and bulk current. The ionizing energy transfer generally leads to an increase of the detector dark currents, whereas the non-ionizing mechanism results in the displacement damage dose (DDD) effect, increasing the dark signal non uniformity (DSNU) (*Srour et al.*, 1986).

The commercial and industrial components generally do not specify radiation tolerance performance, therefore those devices need to be tested under expected space environmental radiation. The TID accumulated during satellite missions depends on the orbit, the mission duration and the shielding. TID effects can be reduced using radiation hardened devices and shielding.

To estimate the reliability of the COTS parts used in our experiment and to determine the required thickness of a radiation shield, the TID was calculated depending on the shielding thickness and different mission scenarios using the SPENVIS (Space Environment Information System)

tool provided by ESA (*Heynderickx et al.*, 2000). For this estimation, a satellite flying in a sun-synchronous orbit at an altitude of 1000 km is expected. Mission durations are 3 years and 5 years, respectively. As a worst case scenario, models for the trapped proton and electron fluxes included in the SPENVIS tool were the Proton model AP-8 at solar minimum and the Electron model AE-8 at solar maximum. The radiation effects caused by electrons, Bremsstrahlung and trapped protons are included in the model.

Figure 2.7 illustrates the SPENVIS output for the accumulated radiation dose for a mission lifetime of 5 years with different aluminum layer thicknesses. The SHIELDOSE-2 is selected for the ionizing dose model, and the shielding is considered as center of Al spheres (*Heynderickx et al.*, 2000). The number of trapped electrons, as the dominant source of the TID, is largely reduced by increasing the thickness of the medium, since the electrons have a low penetration depth and are therefore easy to shield. Meanwhile, the decrease in the number of trapped protons and Bremsstrahlung is not pronounced.

The TID reaching the electronics becomes inefficiently reduced for aluminum thickness greater than 4 mm. The TIDs for 3 year and 5 year missions with 3mm shielding are 11.4 krads and 19.4 krads, these values reduce to 2.4 krads and 4.1 krads when the semi-infinite aluminum medium model is defined for the shielding (*Heynderickx et al.*, 2000). Therefore, to guarantee a nominal lifetime of 3 years the instrument should be able to survive under 11.4 krads radiation without considering the shielding of the satellite.

2.4.2 Radiation test

During the radiation test, the readout electronics in the instrument were classified in modules, which were irradiated in separate steps with different total doses. Radiation tests were made to assure the functionality of the electronics and the detector for the designed mission lifetime. These

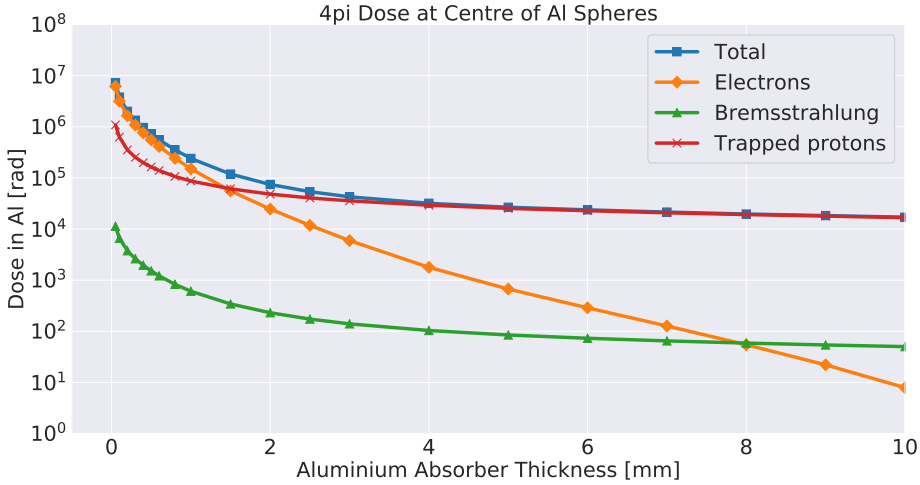

Figure 2.7: Effective dose vs. aluminum shielding thickness for a 5 years mission from SPENVIS. A sun-synchronous orbit at an altitude of 1000 km is assumed.

tests were performed at the Fraunhofer Institute for Technological Trend Analysis (INT). The samples were irradiated with gamma radiation from ^{60}Co, which is a radioactive isotope generated by the irradiation of nature ^{59}Co with neutrons. The homogeneity of the radiation is adjusted based on the dimensions of the components and the desired dose rate. The actual received radiation was calculated based on the distance to the radiation source. This work mainly characterizes the radiation effect on the detector.

Figure 2.8 shows a photograph taken for the experiment of the radiation test on the CMOS detector. To guarantee the full functionality of the electronics during the detector test, lead blocks were used to protect the remaining parts of the printed circuit board (PCB). The detector was irradiated up to 30 krads under uncalibrated mode, the manual calibration mode was activated from then on. The standalone test of the detector indicates that the detector component worked normally until accumulating

85.25 krads radiation, then all detector pixels became saturated.

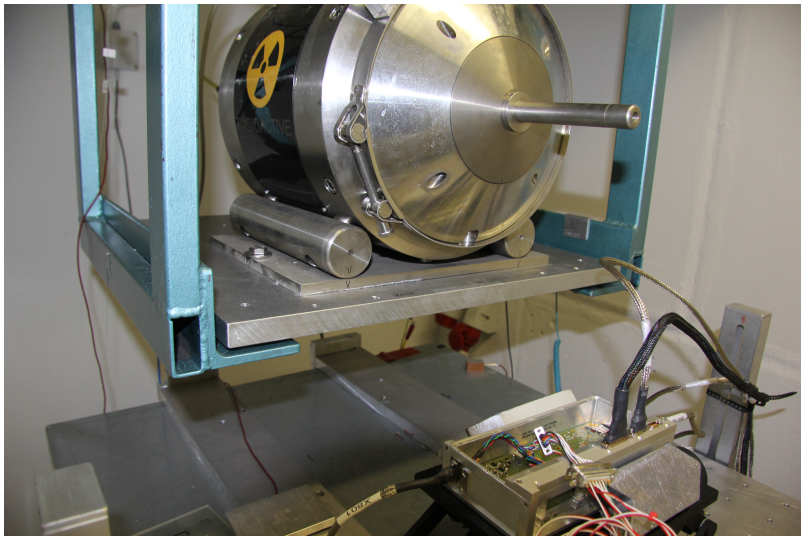

Figure 2.8: Radiation test on the detector board, the lead blocks were used to shield other electronics.

The detector was set to record images continuously during the radiation test. Dark current measurements were taken with 100 ms integration time when the radiation source was switched off. Figure 2.9 illustrates the dark images measured at two different radiation doses. Since the manual calibration mode was switched on after 30 krads radiation on the detector, the dark current at 30 krads is already more than 1000 counts, which is quite remarkable compared the detector dark current measured without radiation (usually below 10 counts under the same integration time at room temperature). The detector dark current increases with the increasing radiation dose. In contrast, the ”hot pixels” were not significantly increased since the ^{60}Co gamma radiation generally causes less DDD effect. Figure 2.10 displays two dark current histograms of the detector for the radiation test, where the long tail of the distribution is clearly shown. The dark signal after radiation shows a remarkable increase, where the corresponding root mean square changes from 1538 counts to 3247 counts.

According to the radiation test result, the detector chip has been qualified up to 85 krads radiation along with the developed detector readout board. Based on this experiment setup, the increase of the detector dark current is verified as one of the degradation effects of radiation. The results confirm that the detector system fulfills the requirement of a three to five years low earth orbit mission. For long term operation in orbit, the detector dark current needs to be measured via deep space observation and subtracted for further scientific analysis.

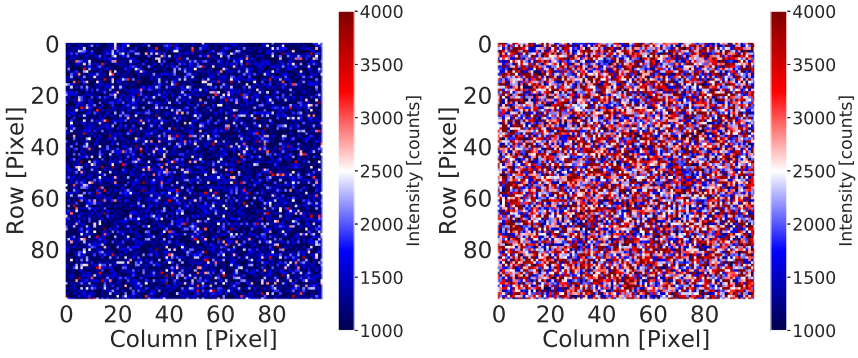

(a) Radiation dose at 30 krads

(b) Radiation dose at 60 krads.

Figure 2.9: Detector dark images measured at two different radiation doses for 100 x 100 pixels, start of row and start of column are chosen to be 450 and 450, respectively. The dark images obtained from the whole detector array reveal similar distribution. The detector was operated under manual calibration mode with integration time 100ms.

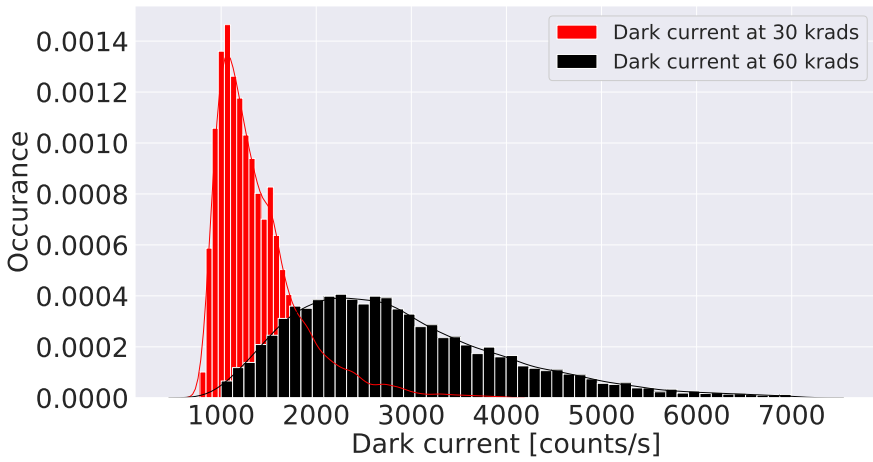

Figure 2.10: Detector dark current histograms measured under manual calibration mode with 30 krads and 60 krads radition. An image area of 600x600 pixels are chosen starting from row 200 and column 200.

Chapter 3

Distortion correction

This chapter mainly describes a method for correcting the radial distortion of interferograms generated by the system. Instead of utilizing calibration patterns, the distortion model parameters are estimated based on the distorted fringe features generated by projecting the straight interference stripes onto the detector. Comparisons between polynomial models and division models indicate that division models can deliver competitive performance on the reconstructed image with fewer parameters. Simulated interferograms based on ray-tracing are used to demonstrate the correction of errors in spatial, phase and spectral domain caused by optical distortion.

3.1 Optical distortion

Besides the interferometer, the AtmoSHINE optical system contains two additional parts: the front optics, which images the object onto the gratings in the interferometer, and the detector optics, which images the fringes onto the two dimensional detector array. This particular configuration exhibits some inherent radial distortions, especially in an SHS system with limited space and equipped with spherical lenses (*Kaufmann*

et al., 2018).

Optical lens distortion is one of the most severe effects among various aberrations, and results in a non-linear geometrical mapping from the object to the image. This distortion effect is caused by the non-constant value of the magnification factor of the optical system. The optical distortion effect may result in the deviation of the extracted geometric information, which leads to false altitude mapping of the measurement in space if not well corrected. Since the horizontal information of a recorded image and the modulated fringes of the corresponding interferogram are overlapped in one dimension, this distortion effect will also influence the accuracy of the Fourier transformed spectra.

Englert et al. (2005) summarizes three kinds of phase errors on the measured interferograms in an SHS system. The first kind gives an additional phase shift on the obtained interferogram depending on the emission wavelength. Possible reasons for such a shift are the dispersion effect of the beam splitter and the sampling grid that does not include the zero path difference (ZPD) location. According to *Englert et al.* (2005), this phase shift will not affect the measured emission intensity once the absolute value of the Fourier transformed spectrum is used. The second type of the phase distortion is the frequency-independent distortion, which only exhibits localized effect on the measured interferograms, e.g. the defect of the gratings. Since this phase distortion arises mainly due to local effect and varies for different instruments, it will be studied later in Chapter 5 with practical measurements.

The optical distortion effect mainly leads to the third phase error on the obtained fringes. Due to the variation in the optical magnification factor of the system, emissions with different spatial frequency result in different scales of phase distortion. Therefore, this effect is both position and frequency dependent. As proposed in *Englert et al.* (2005), this kind of phase distortion can be corrected in spectral domain via convolving with a correction function, which can be determined by measurements using a monochromatic source at each wavelength. Typically, for the correction of such phase distortion, a phase map needs to be built up based

on measurements at different wavelengths. Nevertheless, this correction technique is limited to certain conditions since it requires the phase distortion to be a slow varying function of the pixel position and wavenumber, which is sometimes not true for an interferogram with a large distortion. Therefore, it is practically more convenient to correct the phase error induced by optical distortion directly on the interferogram.

Since the fringe patterns are overlapped with the spatial structure of the measurements, the optical distortion effect will affect the spatial information and distort the obtained interferogram at the same time. If the distortion effect is mostly introduced by the detector optics, the geometric distortion is analogous to the interferogram distortion. On the contrary, in the absence of detector optical distortion, the obtained spatial information can be affected by the front optics, which is not the case for the interferograms. According to the analysis of the payload optical system, the detector optical distortion (7.1%) is significantly larger than the front optical distortion (0.4%). This work primarily studies the system whose image distortion is mainly dominated by the detector optical distortion. This technique can also correct the interferogram obtained by an SHS system without front optics.

3.2 Distortion characterization

3.2.1 Model based distortion correction

The radial distortion effect can be described by the Brown's distortion (polynomial) model (*Brown*, 1966):

$$r_d = r_u \left(1 + k_1 r_u^2 + k_2 r_u^4 + \cdots\right) \tag{3.1}$$

where r_d and r_u represent the distorted and undistorted radius with respect to its optical center, and k_n is the n^{th} radial distortion coefficient. For the one parameter polynomial model, a negative value of k_1 corresponds to

a barrel distortion, while a positive value of k_1 represents a pincushion distortion. It is also reported that the model may become numerically instable when a much higher order is implemented (*Tsai*, 1987). Another type of model that is also applicable is the division model:

$$r_d = \frac{1}{1 + k_1 r_u^2 + k_2 r_u^4 + \cdots} r_u \tag{3.2}$$

This model simulates the distortion behavior with fewer parameters and works even for large distortion scenes (*Fitzgibbon*, 2001).

Estimating the distortion parameters is generally considered to be a part of the camera calibration procedure, where the most popular method is proposed by Zhang (*Zhang*, 2000) via taking images of a planar pattern from different orientations. The camera intrinsic parameters (including the distortion) can be estimated from the detected features. This is, however, not applicable to some camera systems due to their unique configurations. Alternatively, these parameters can also be determined based on the geometric invariant principle by making use of geometric properties like the straight lines (*Devernay and Faugeras*, 2001) and vanishing points (*Becker and Bove Jr*, 1995).

So far, the straight lines are the most commonly applied geometric property for radial distortion correction. Based on the perspective principle, the projection of straight lines will also be straight, and yet these lines are eventually rendered as curved lines on the detector due to the radial distortion effect. Therefore, points on a curved line will reform a straight line once the distortion is well corrected with proper model. The corresponding model parameters can therefore be estimated by taking this property into the optimization procedure and minimizing the errors of the reconstructed curves to a set of ideal straight lines (*Alemn-Flores et al.*, 2013).

Accurate estimation of the distortion parameters requires the selected curves to be long enough, e.g. minimum length longer than half of the image size (*San Choi et al.*, 2006). Compared to images taken from

common imaging cameras, the fringes generated by the SHS are the major constitution of the detected curves, which is fulfilled for our square region of interest. This provides sufficient long curved features for the parameter estimation. In addition, the detected features should contain curves localized further away from the optical center, because using lines exhibited only in the center region generally results in the underestimation of distortion parameters.

3.2.2 Distortion model comparison

This section investigates the performance of several distortion models to determine the suited models for radial distortion correction of an SHS instrument. To assess the performance of the two models, the instrument is simulated using optical ray-tracing. This allows to compare the performance of the two distortion models using best possible data given by the ray-tracing software. Some relevant parameters are listed in Table 3.1. Parameters of polynomial and division models are estimated based on pairs of distorted and undistorted points, which are generated from the grids output (Figure 3.1).

Table 3.1: **Parameters of ray-tracing model**

Component	Item	Value
Filter	Wavelength range	761.9-765.3 nm
Fore optics	Field of view	$\pm 0.65^{\circ}$
	Aperture diameter	66 mm
SHS	Littrow wavelength	761.8 nm
	Littrow angle	27.2°
	Grating groove density	1200 lines mm^{-1}
Detector optics & detector	Numerical aperture (obj. space)	0.12
	Magnification factor	0.55
	Focal length	28mm
	Utilized detector pixel number	800×800 pixels
	Detector pixel size	$5.04 \times 5.04\ \mu m^2$

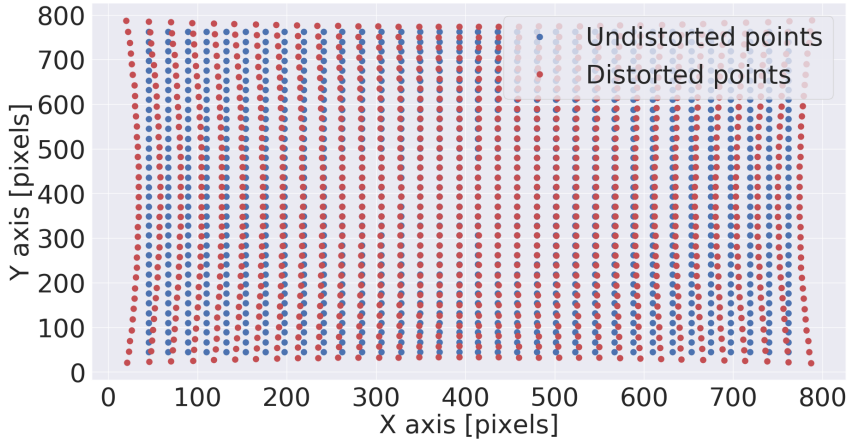

Figure 3.1: Generated grids for distorted and undistorted points via a ray-tracing simulation. The output grids contain 101*101 points, shown partly for 34*34 points.

The estimated model parameters are then used to reconstruct the undistorted points from the distortion points. Model performance is evaluated based on the residual distances between the points after reconstruction and the undistorted positions generated by the software. For the polynomial models containing multiple parameters, their inverse operations are usually difficult to perform. Therefore, iterative scheme is employed in the reconstruction procedures (*Debevec et al.*, 1996; *De Villiers et al.*, 2008). Alternatively, the undistorted points can be reconstructed by the analytical inverse expressions for division model within two parameters.

Table 3.2 summarizes the results of the distortion reconstruction performance using various models for comparison. For the mean values obtained on the whole image area, models with different types and different orders do not offer remarkable differences. As presented by the maximal reconstruction errors in the results, models that consist of more parameters would generally provide better estimation results for the distortion away from the optical center. Among those, one or two order di-

Model	Expression	Mean residual [pixels]	Max residual [pixels]	Estimated parameters
Polynomial	$1+k_1r^2$	0.535	1.878	$k_1 = 2.57\times10^{-7}$
	$1+k_1r+k_2r^2$	0.506	1.404	$k_1 = -1.12\times10^{-5}, k_2 = 2.82\times10^{-7}$
	$1+k_1r^2+k_2r^4$	0.505	1.319	$k_1 = 2.37\times10^{-7}, k_2 = 1.19\times10^{-13}$
Division	$1/(1+k_1r^2)$	0.512	1.336	$k_1 = -2.46\times10^{-7}$
	$1/(1+k_1r+k_2r^2)$	0.506	1.324	$k_1 = 4.43\times10^{-6}, k_2 = -2.58\times10^{-7}$
	$(1+k_1r)/(1+k_2r+k_3r^2)$	0.505	1.318	$k_1 = -2.73\times10^{-4}, k_2 = -2.77\times10^{-4}, k_3 = -2.07\times10^{-7}$

Table 3.2: Comparison of the model performance for the distortion reconstruction, where the residuals indicate the distances between the undistorted points from reconstruction and from output of the software. 101*101 pairs of distorted and original points are used in the evaluation. Mean residual stands for the average distance of all samples, and the max residual presents the largest value.

vision models slightly outperform the polynomial models with the same order. The minimum reconstruction errors are achieved by utilizing the two parameter polynomial model with higher order and the three parameter division model.

The detailed residual maps are displayed in Figure 3.2 for individual point reconstructed using both polynomial and division models. The residuals from the polynomial model with one parameter (Figure 3.2(a)) are higher than those from other models, especially at the corner regions. The performance of one parameter division model is quite close to the performance of two parameter polynomial models. To some extent, the additional parameter in the two parameter division model tends to refine the distortion at the corner areas, whereas the overall performance is close to the results attained from the one parameter model.

3.3 Interferogram distortion correction

The correction of a distorted interferogram utilizing image features can be divided into several main procedures, as shown in Figure 3.3 for a demonstration. Firstly, the edge points on the interferogram are extracted by applying some edge detection operators, e.g. the Canny edge detector (*Canny*, 1986). These outlined points are then connected and grouped

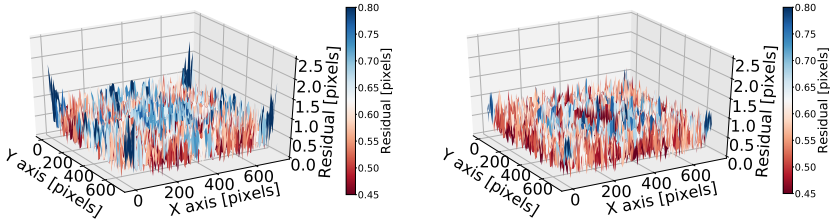

(a) Polynomial one parameter model: $1+k_1r^2$

(b) Polynomial two parameters model: $1+k_1r+k_2r^2$

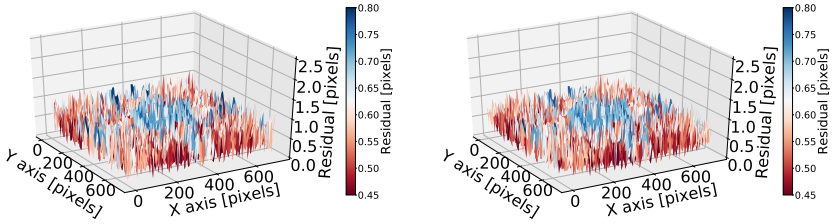

(c) Division one parameter model: $1/(1+k_1r^2)$

(d) Division two parameters model: $1/(1+k_1r+k_2r^2)$

Figure 3.2: Residuals (radius in pixels) between the original positions and the reconstructed points using different distortion models. $1+k_1r^2$ and $1+k_1r+k_2r^2$ stand for the polynomial models with one and two parameters, the division models shown here are $\frac{1}{1+k_1r^2}$ and $\frac{1}{1+k_1r+k_2r^2}$.

into different candidate curves. After minimizing the objective function described by the error between the reconstructed line segments and their corresponding straight lines, the distortion parameters could be optimized. Consequently, the distorted interferogram can be corrected analytically from the inverse conversion, or numerically from the iterative approach.

Conventional polynomial distortion models with more than one coefficient commonly do not provide the exact inversion. Although the undistorted points can be numerically reconstructed for each pixel via the iterative approach, this procedure requires an additional computational

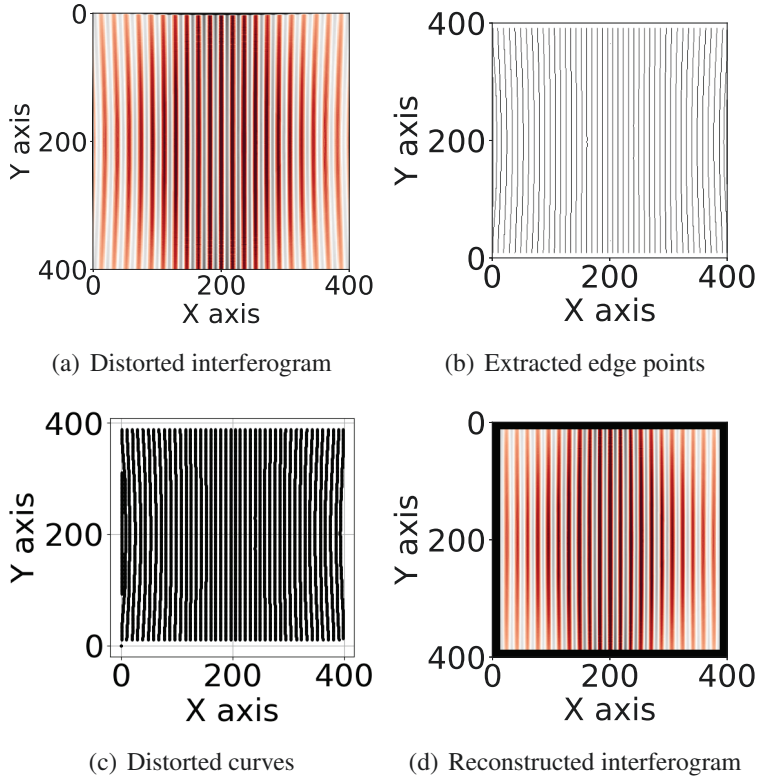

(a) Distorted interferogram (b) Extracted edge points

(c) Distorted curves (d) Reconstructed interferogram

Figure 3.3: Correction of a distorted interferogram. In this simulation, the pixel size is $10\times10\ \mu m^2$. From the original interferogram (a) the edge points are detected (b). (c) represents the distorted curves for the parameter optimization. (d) displays the reconstructed interferogram after distortion correction.

effort, especially in the optimization procedure where the cost function needs to be calculated multiple times. As shown in Section 3.2.2, the division models are able to provide comparable or even slightly better performances than the polynomial models. In this case, the division models, which can offer the exact analytical inverse, will be used in the optimiza-

tion procedure.

Estimating the distortion parameters is a typical non-convex optimization problem for models with multiple parameters, and it usually results in getting stuck in local minima if the parameters are not properly initialized. For the division model containing only one parameter k_1, the cost function becomes close to a unimodal function in the feasible region (ruling out the case when k_1 gets close to negative/positive infinity, those points would be flocked). In addition to the typical optimization methods widely used in higher dimensional optimization problems, some basic algorithms such as the line search method and Newton's method (*Luenberger et al.*, 1984) can offer more direct alternatives for solving this one-dimensional minimization task in limited iterations. Therefore, the one parameter division model is chosen for the interferogram distortion correction.

3.4 Results and analysis

3.4.1 Spatial information

To verify the performance of the distortion correction, several interferograms are simulated based on the designed model parameters, as presented in Table 3.1. In these simulations, each interferogram was generated using a single emission line as input. Figure 3.4(a) and 3.4(b) display the results of distorted and reconstructed interferograms using the one parameter division model for the correction. The inhomogeneous intensity distribution of the displayed interferogram is caused by the undersampling on local areas during ray-tracing. Therefore, localized thresholds are needed for image segmentation to detect the useful curved lines. For these interferograms, the adaptive thresholding method (*Gonzalez and Woods*, 2002) is implemented in the edge detection procedure.

To evaluate the algorithm performance under different noise levels, a numerical study is made for the parameter estimation in different scenarios. The signal-to-noise ratio (SNR) of each interferogram is defined by

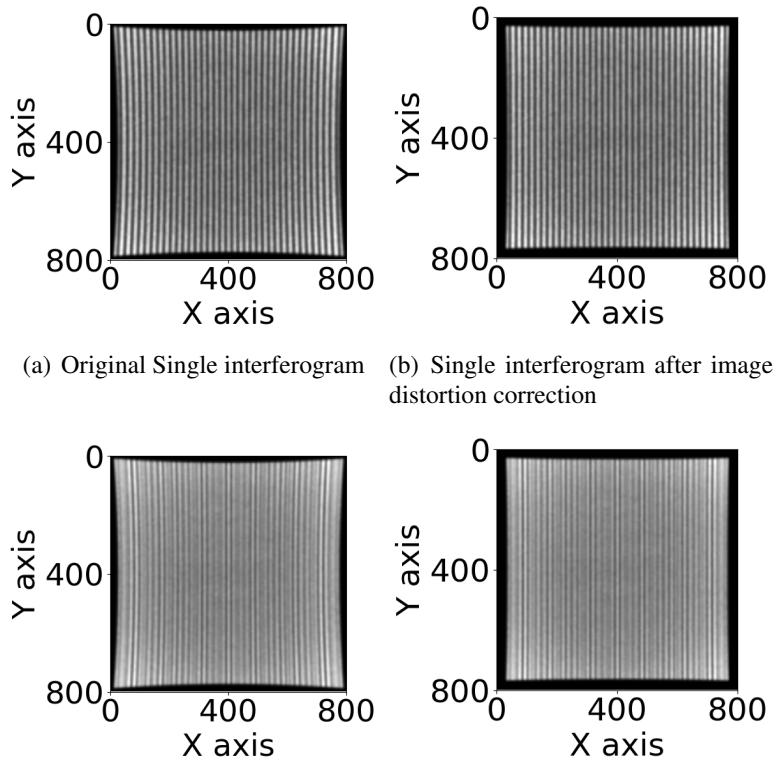

(a) Original Single interferogram

(b) Single interferogram after image distortion correction

(c) Original composed interferogram

(d) Composed interferogram after image distortion correction

Figure 3.4: (a) A distorted interferogram generated at 763.4 nm wavelength using a ray-tracing software. (b) The corresponding interferogram after applying image distortion correction using the one parameter division model. (c) Composed interferogram containing emission lines at 763.4 nm, 763.8 nm and 764.2 nm. (d) The corresponding interferogram after distortion correction. For each interferogram, the pixel size is 5×5 μm^2.

the intensity of the signal A_{signal} and the standard deviation σ_{noise} of the

additive white Gaussian noise (AWGN) as: $SNR(dB) = 20log\frac{A_{signal}}{\sigma_{noise}}$. The estimation results are shown in Figure 3.5 in comparison with another approach containing simple Gaussian filter for noise reduction.

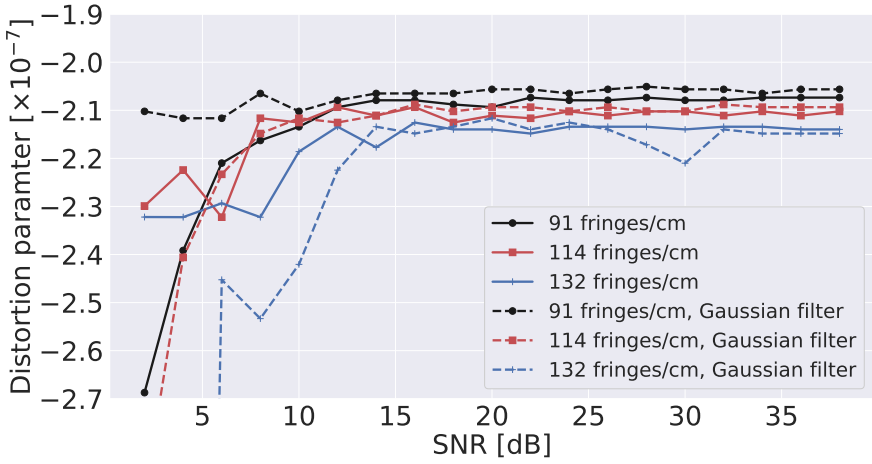

Figure 3.5: Parameter estimation results for interferograms with different spatial frequencies with respect to SNR (dB). The dashed lines represent the results with Gaussian filter for noise reduction before edge detection.

Both methods can deliver well-stablized estimation if the SNR is higher than 15 dB. For the parameter estimation based on the raw noisy interferograms, the performance is relative worse if the SNR is low. The modulation efficiencies in edge areas as seen in Figure 3.4(a) are higher than that in the center region. In the presence of larger noise, the algorithm fails to detect the corresponding features with lower modulation efficiency, therefore the distortion parameters estimated are consequently larger in absolute value since only the features on the edges are substantially valid for the optimization. A classical linear filter, the Gaussian filter, is implemented for the noise reduction before edge detection. This filter smooths the image, which meanwhile blurs the edges. This technique would help to improve the accuracy under lower spatial frequency, whereas it will limit the performance for higher frequency patterns.

Figure 3.6 illustrates the results of parameter estimation using the Golden section search method for the optimization. The figure shows that this method exhibits convergence within limited iterations for the optimization problem. The slight fluctuation of the objective function is a typical behavior of this method, since a new, narrower search interval is constructed for each iteration. The objective functions shown in this plot are relatively high for larger wavelengths, since the curved lines in interferograms with very high spatial frequency can not be separated easily.

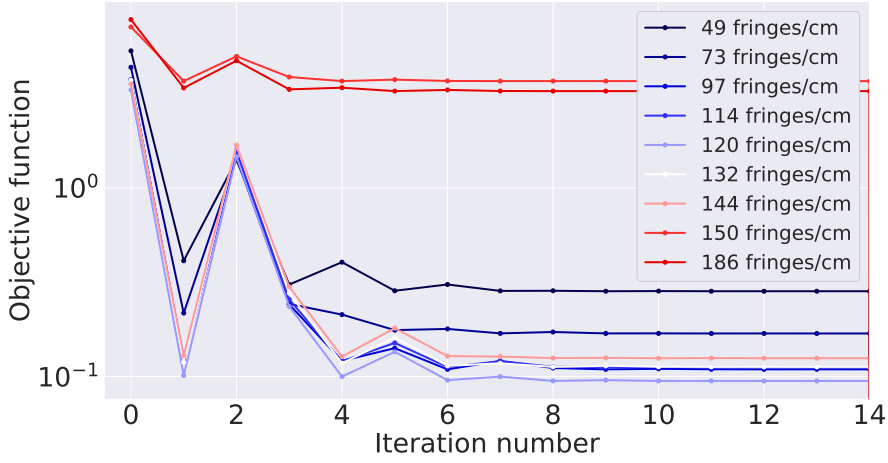

Figure 3.6: The convergence rates of the optimization algorithms using Golden section search method. Interferograms with wavelengths between 762.6 nm (49 fringes/cm) and 764.9 nm (186 fringes/cm) are used for the estimation.

Figure 3.7 reveals the estimated model parameters from interferograms at different wavelengths based on one parameter division model. In this demonstration, the minimum spatial frequency on the detector is about 49 fringes/cm at 762.6 nm, and the maximum spatial frequency is about 186 fringes/cm at 764.9 nm. Similar to the results shown in Figure 3.6, the estimated parameters are relative larger at higher wavelengths,

which are likely caused by the inaccuracy introduced by the high spatial frequency features that are not easily distinguishable. On the contrary, the interferograms with lower spatial frequencies provide limited curve features for the optimization, resulting in the underestimation of distortion values.

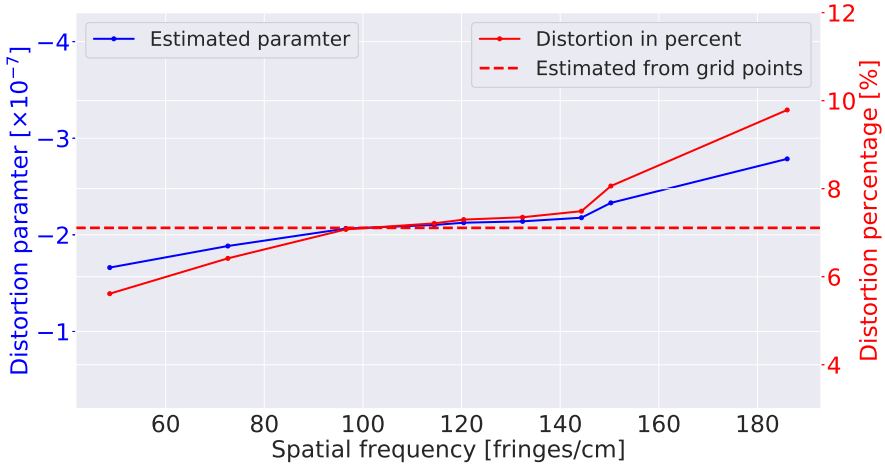

Figure 3.7: Estimated distortion parameters from the interferograms generated between 762.6 nm and 764.9 nm. The corresponding distortion in percent is represented by: $Distortion(\%) = 100 \times \frac{r_d - r_u}{r_u}$ of the farthest point in each interferogram. The dashed red line represents the distortion in percent obtained from grid points shown in Figure 3.1.

The distortion obtained from the grid points in Figure 3.1 is about 7.1%, which is similar to the values obtained in the center wavelength region (around 763.8 nm, 132 fringes/cm). The estimated model parameters are quite close to the results using the distortion grids from one parameter division model. This also indicates that the optical distortion is mainly caused by the detector optics. Besides, the deviation in the estimated values between two approaches likely results from different objective functions in the optimization procedures for the estimation of distortion parameters, as well as the slight difference on the selected regions for

processing. Due to the limited modulation efficiency of the simulated interferograms and the number of samples, the feature extraction for high frequency pattern may not be accurate.

3.4.2 Phase and spectral information

In this section, the performance using the image distortion correction for an optical distortion dominant system is compared with the performance using the phase distortion correction technique. The phase distribution of each interferogram is calculated based on the Fourier transform approach. Following *Englert et al.* (2005), additional steps like the phase unwrapping and the linear trend removing are implemented to get the correct phase curve of the interferogram. Once the phase function $\varphi(x,k)$ is determined, the distortion effect can be corrected via multiplying the fringe pattern with function $e^{i\varphi(x,k)}$ in spatial domain. This multiplication operation corrects the spectral information in "positive" part of the double-sided spectrum, whereas the spectral information in "negative" part is consequently doubled.

Accordingly, the interferogram distortion correction algorithm is applied on each frame based on the same model parameter obtained at 763.8 nm (about 120 fringes/cm). Phase information at row 400 is displayed in Figure 3.8 as a demonstration. The large phase variations on two sides of the phase curves in Figure 3.8(a) are dominated by the effect of optical distortion, which is more pronounced for the points farther away from the optical center. Since the whole interferogram is consequently squeezed after reconstruction, the interfergram edges do not contain useful fringe information, which therefore exhibits the fluctuations on the reconstructed phase error on both sides (Figure 3.8(b)). After correction, the maximal phase distortions are reduced from 1.5 rads to less than 0.5 rad on the effective area (about 700 pixels in the center region).

Figure 3.9 illustrates the interferogram phase values as a 3D global map for inter-comparison between different rows. The overall phase dis-

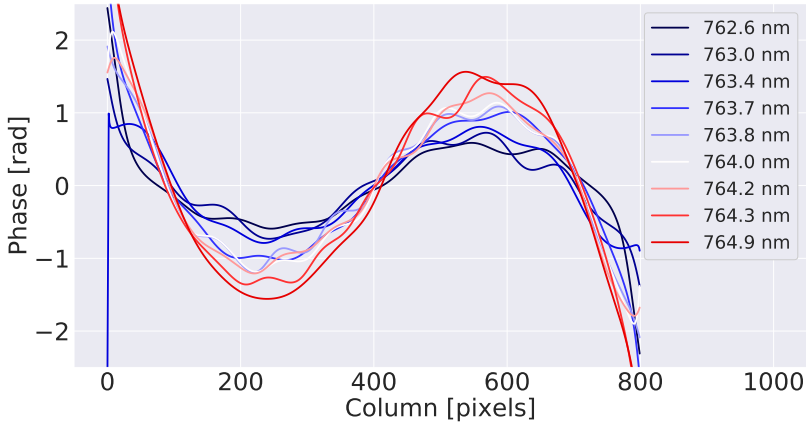

(a) Phase before image distortion correction

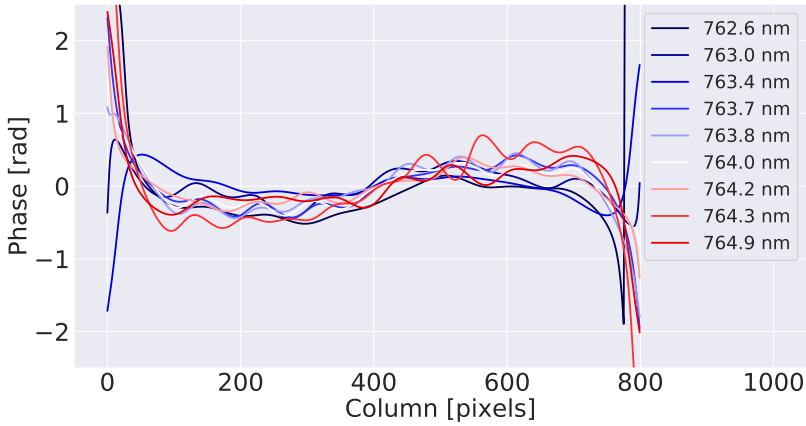

(b) Phase after image distortion correction

Figure 3.8: Phase distribution of different wavelengths before (a) and after (b) implementing image distortion correction using the same correction parameter obtained at 763.8 nm. Row 400 is chosen for demonstration.

tribution, which is symmetrically deviated on two sides, becomes nearly flat around the center region after reconstruction. The corrected phase

curves at different rows show satisfactory results using the same reconstruction parameter. In practice, one can fine-tune this parameter to achieve the best correction performance.

To assess the distortion correction effect in spectral domain, a typical interferogram containing multiple emission lines is generated by composing three single interferograms at different wavelengths, as shown in Figure 3.4(c) and Figure 3.4(d) before and after image distortion correction. In these comparisons, phase distortion correction and image distortion correction techniques are applied in spatial domain. The phase distortion correction is applied individually for each signal component, then these interferograms are composed together. In addition, another correction procedure, which contains both the image distortion and phase distortion corrections successively, is also included. When both correction methods are used, the image distortion correction is implemented before the phase distortion correction.

As can be seen in the Fourier transformed spectra from Figure 3.10 for the relative intensities, the side lobes of the spectrum (black line) without any correction lean toward one side, since the spatial frequency of a fringe is not consistent on the whole area due to the radial distortion effect. The spectrum shape becomes concentrated after implementing the image correction or phase correction. The output spectrum intensities with correction techniques are in accordance with each other in 1%, while the original spectrum peaks are about 3% lower.

The shift of the spectral position is another consequence of the distortion effect. For a pincushion-like distorted interferogram, the spatial frequency on both sides of the fringes is smaller than that on the center area. To determine the phase function for phase correction based on the Fourier transform, the increment of the phase along the optical path needs to be subtracted after phase unwrapping. Due to the presence of optical distortion, the estimated spatial frequency used for the phase detrending may deviate. Without image distortion correction, this effect will shift the spectrum towards the lower spatial frequency direction for a pincushion-like distorted interferogram. The spectrum without any correction reveals

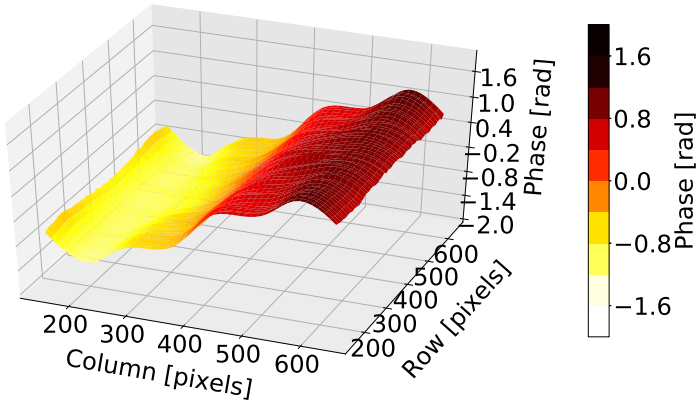

(a) Phase map without image correction

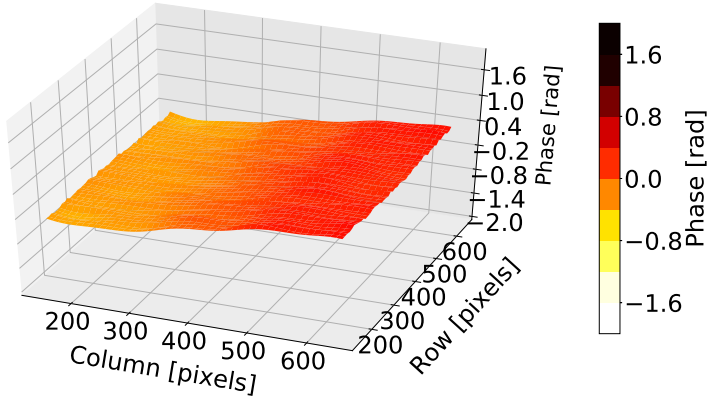

(b) Phase map with image correction

Figure 3.9: Interferogram (763.8nm) phase distribution before (a) and after (b) implementing interferogram distortion correction. The range shown is between 100-700 pixels by columns and 100-700 pixels by rows. The phase is normalized to 0 at pixel 400.

strong side lobe effect due to optical distortion, which will also be studied

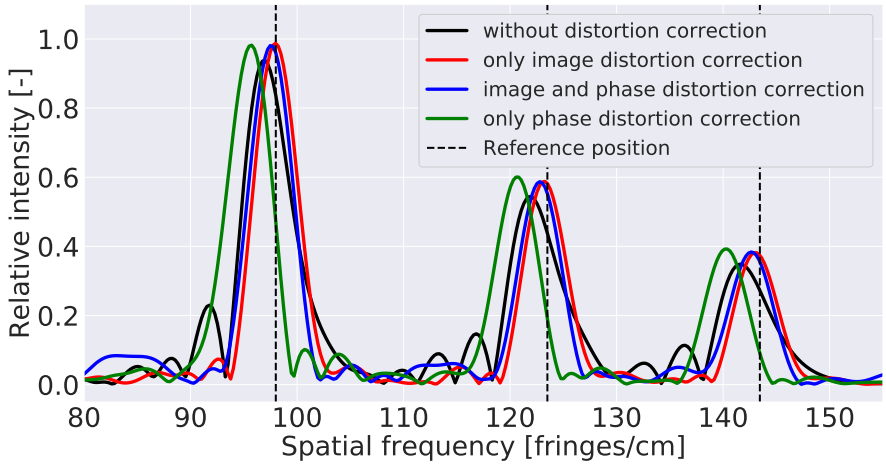

Figure 3.10: Obtained spectra using different correction techniques, Hanning window function is used for apodization. Simulated emission lines are 763.4nm, 763.8nm, 764.2nm. The dashed lines indicate the expected positions based on the simulation parameter. The spatial frequency shown in x-axis refers to the spatial frequency of the fringe patterns on the detector.

later in Section 5.4.

A comparison between the combined correction procedure (blue line) and the interferogram distortion correction standalone (red line) shows little deviation in spectral domain. In this case, the interferogram distortion correction can provide satisfactory performance in a radial distortion dominated SHS system. The slight spectral position shift after the corrections with respect to the expected ones can be fine-tuned via Littrow recalibration if needed. Once the phase distortion associated with the optical distortion is corrected, the phase correction will not deviate the spectral position. For a system where other phase distortion effects are also prominent, the interferogram distortion correction technique ought to be included before implementing the phase distortion correction.

Chapter 4

Spectrum analysis

This chapter mainly focuses on the spectral analysis for interferograms generated by the SHS instrument. The analysis based on the Fourier transformation is introduced with different apodization functions, where the spectral leakage and picket-fence effect are also addressed. The frequency estimation of the fringe patterns based on the subspace methods is studied, which is able to provide higher spectral resolution for line spectra with limited samples. These methods are investigated with respect to different noise levels, different dynamic ranges as well as different broadening conditions.

4.1 Fourier analysis and apodization

The recorded interferogram for an ideal SHS instrument containing K emission lines can be modeled as:

$$y(x) = \sum_{i=1}^{K} B(\sigma_i)\left[1 + \cos(2\pi f_i x + \varphi_i)\right] \tag{4.1}$$

with the corresponding intensity $B(\sigma_i)$, wavenumber σ_i, spatial frequency f_i and phase φ_i of each emission line. Similar to a conventional Michelson Interferometer (MI), the frequency domain representation of the signal can be obtained via Fourier transformation as a weighted sum of exponential spectral components with the corresponding amplitudes and phases. For digitalized signals, the spectral information at each frequency bin can be derived from well sampled points in time or spatial domain via discrete Fourier transform (DFT), which is generally implemented by a set of algorithms namely the fast Fourier transform (FFT) (*Rader and Brenner*, 1976) for fast computation of the DFT based on divide-and-conquer method.

FFT analyzes finite samples of a signal, which constitutes a rectangular window (apodization) on the data stream with infinite replication (or periodic extension) of this slice. Multiplying such a boxcar function results in a convolution with the Fourier transformed window function in the frequency domain, which results in side lobes around the spectral peaks. When the spectral component does not contain an integer number of cycles inside the sampled internal, the frequency component will not represent the corresponding position and peak. This leakage effect is manifested as a loss of spectral resolution as well as the amplitude precision in spectral domain. In the same time, it spills the emission spectrum centered at one frequency bin into the surrounding regions, which limits the resolving power for high dynamic range signals. Weak signals are masked and therefore difficult to be detected in spectral domain.

Since this leakage effect is mainly associated with the discontinuity on the ends of the signal, it can be suppressed by using a multiplicative function, which gradually and gently reduces the signal intensity towards zero on the edges. Consequently, the extended sequence on the boundaries can be smoothly connected without significant deviation on the amplitudes. Commonly used windows are the Hanning window, the Hamming window, the Blackman window, etc. Some of the corresponding window properties are summarized in Table 4.1 based on *Cerna and Harvey* (2000) and *Harris* (1978).

Windowing the original signal results in the modification of the corresponding signal envelope. Besides integrating over all the relevant DFT bins, the input amplitude can also be determined by its peak intensity, where the spectral peak needs to be corrected by multiplying a scaling factor based on the utilized window coefficients. Generally, a window function with small side lobe levels (side lobe level in Table 4.1) implies a widen main lobe. For example, the Hanning window does not provide as much side lobe suppression as the Blackman window does, but its main lobe is narrower, which offers higher spectral resolvability for the frequency information. Therefore, the choice of a proper window function varies for specific applications to make an inherent trade-off between lowering the side lobes and remaining the narrow main lobe.

Table 4.1: **Window functions and their properties.**

Window type	Scaling factor	RBW (-6dB)	ENBW	Side lobe level (dB)
None (rectangular)	1.0	1.21	1.0	-13.3
Hanning	0.5	2.00	1.5	-32.2
Hamming	0.54	1.81	1.36	-43.5
Bartlett	0.5	1.77	1.33	-26.5
Blackman	0.42	2.29	1.73	-58.1
Flat top	0.215	4.67	3.78	-68.8

As a result of multiplying the original signal with a window function, the main lobe of the Fourier transformed spectrum becomes broadened compared with the spectrum from non-windowed signal. For closely located multiple signal components with similar amplitudes, their main lobes may be overlapped due to limited resolving power. The resolution bandwidth (RBW) describes the width of the main lobe frequency interval of a 6dB attenuation, which corresponds to a drop of amplitude to 50% (FWHM). As the consequence of the broadening effect, more noise is transfered into the measurements, which increases the uncertainty of spectral information. In this case, the equivalent noise bandwidth (ENBW) of a window function is used for the evaluation of the amount of noise gathered inside of the the main lobe with respect to a non-windowed spectrum.

The FFT operates like a bank of filters with certain bandwidth for each bin spacing, therefore only the noise inside this frequency range is transfered into the corresponding spectral information. For a double sided Fourier spectrum, the improvement of the SNR for each frequency bin is a factor of $\sqrt{\frac{N}{2}}$ for fringe pattern with N samples. As a consequence of applying the window function, the spectrum is broadened and the amount of noise that is accumulated in one frequency bin is also increased. To account for this effect, the ENBW should be included as the corresponding factor to represent the equivalent filter bandwidth for the effective SNR in spectral domain.

Figure 4.1 illustrates the spectra converted from a composed fringe pattern with two different spatial frequencies utilizing various window functions. The spectral resolution achieves its maximum with the smallest FWHM without additional apodization function, while the leakage effect produces large interference between adjacent lines. Adding the window functions attempts to suppress the side lobs by broadening the width of the main lobe, which thus reduces the spectral resolution. When multiple emission lines are closely located, the Hanning function or the Hamming function is suggested for use without greatly losing the spectral resolution. The Blackman window function is sometimes preferred to reduce the side lobe effect. A more specific analysis of the SNR with different apodization functions is provided in Section 5.8.1 considering the instrument radiometric performance.

The estimation accuracy of the spectral information (frequency, amplitude and phase) is generally limited to half of the spectral bin, since the DFT only enables the spectrum to be resolved at each bin component. In reality, the spectrum of a natural signal is composed of frequencies lying on a continuum, they can not be well approximated by atoms on the DFT grid. This is sometimes called the picket fence effect, the associated attenuation of the spectrum magnitude is named the scalloping loss (*Harris*, 1978).

When the frequency sampling is considered to be too sparse, zeros

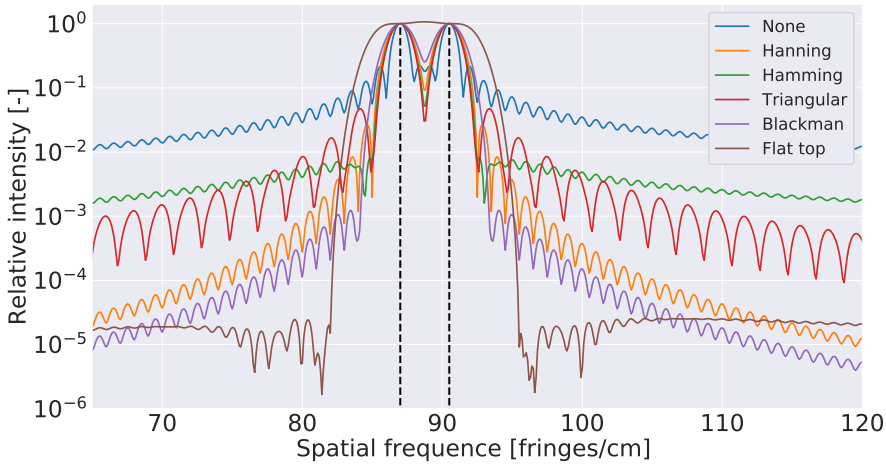

Figure 4.1: Spectral information obtained via different window functions. Input signal amplitude is 1 for each sinus component, input frequencies are 87 and 90.5 fringes/cm, represented by the dashed black lines in the plot. The scaling factor is used to show the amplitudes at the corresponding positions. Zero padding with a factor of 10 is added on the original signal.

padding at the end (sometimes on both sides) of the signal leads to the interpolated spectrum in spectral domain, which can therefore provide a high quality Sinc interpolation of the non-padded FFT of the original data. Therefore, a good representation of the estimated spectrum can be achieved. The zero padding is sometimes not computationally efficient if the accuracy of the spectral information is highly required (*Smith and Serra*, 1987), e.g. several orders of magnitude better than the resolution of DFT bins. Alternatively, the scalloping loss can be corrected by spectral interpolation methods based on maximal amplitude samples in the main lobe (*Jain et al.*, 1979; *Abe and Smith III*, 2004).

4.2 Line spectra estimation

As a typical non-parametric approach, the DFT usually has limited resolving power and estimation accuracy due to additional window functions and the spectral leakage effect. Its accurate representation also requires long observation intervals. Instead, the parametric methods represent the spectrum by firstly estimating the parameters of the signal model in the presence of noise. Since the parametric methods do not rely on data windowing, the results will not lead to the spectral leakage effect. Owing to the additional information assumed, a parametric method is expected to offer better frequency resolution than the non-parametric method, especially when applied to measurements with shorter samples.

The SHS instrument generally has very high spectral resolution, which enables individual emission line to be parameterized independently. Since the measured spectrum consists of limited number of components, the recorded interferogram is usually very sparse in spectral domain, which allows the interferogram to be represented with a few parameters. When the envelope of the fringe pattern is slowly varying on the detector array, e.g. by using a cylindrical lens as indicated in *Damiani et al.* (2007), the line spectrum property can be well preserved.

The line spectral signal can be represented as a sparse linear combination of atoms in a indexed dictionary from a finite number of observations. In several applications, particularly in radar, communication, interferometry and so forth, the signals can be well described by the combination of the Fourier basis at different frequencies f_i for complex valued signal:

$$y(x) = \sum_{i=1}^{K} A_i \left(e^{-j(2\pi f_i x + \varphi_i)} + e^{j(2\pi f_i x + \varphi_i)} \right) + \mathcal{N}(\mu, \sigma^2) \tag{4.2}$$

with the amplitude A_i and the initial phase φ_i for each component. $\mathcal{N}(\mu, \sigma^2)$ represents the additive white Gaussian noise (AWGN) with bias μ and standard variance σ.

A joint estimation of the signal amplitude and phase from the fringe

pattern is considered as a convex optimization problem for determined frequency f_i , which can be solved via least square method when the phase estimation is conveted to the linear estimator as well (*Daniels*, 2010). Detailed formulation can be found in Appendix A.1. Nevertheless, a good estimation performance is not always guaranteed by applying the least square method unless an accurate initialization for the frequency information is provided, since the function has many sharp global maxima for f_i. Although the peak positions in spectral domain from DFT can be treated as the good starting values for the optimization, the spectral resolution based on this method is still limited by the resolving power of the Fourier transform.

Alternatively, several high resolution power spectrum estimation methods such as the Pisarenko harmonic decomposition (*Pisarenko*, 1973), Maximum Entropy Method (MEM) (*Burg*, 1972) and Capon's Minimum Variance Method (MVM) have been proposed in the past decades. In addition, some methods based on the covariance matrix information can also be used to estimate the signal frequency with higher resolution. These methods decompose a covariance matrix of the noisy signal into signal subspace and noise subspace. Typical subspace methods are the MUltiple SIgnal Classification (MUSIC) (*Schmidt*, 1986) and the Estimating Signal Parameters via Rotational Invariance Techniques (ESPRIT) method (*Roy and Kailath*, 1989). These methods both require some a-priori information of the signal, e.g. number of components, to separate the eigenvalues in signal subspace and noise subspace. They are able to achieve asymptotic approach to the Cramer-Rao Lower Bound (CRLB, *Stoica and Nehorai* (1989)), a lower bound on the variance of unbiased estimators, with a good approximation (*Swindlehurst et al.*, 2001).

4.2.1 Multiple signal classification (MUSIC)

Generally, a signal made of K complex sinusoids with unknown frequency f_i can be modeled as:

$$\begin{aligned} y(x) &= \sum_{i=1}^{K} A_i e^{j(2\pi f_i x + \varphi_i)} \\ &= \sum_{i=1}^{K} A_i e^{j\varphi_i} e^{j2\pi f_i x} \end{aligned} \tag{4.3}$$

where A_i, φ_i are the unknown amplitude and initial phase information, respectively. A real valued sinusoidal signal can be expressed by the combination of two exponential components at $\pm f_i$. In the presence of AWGN, the signal model can be vectorized as:

$$\boldsymbol{Y}(\boldsymbol{x}) = \boldsymbol{A}(\theta)\boldsymbol{s}(\boldsymbol{x}) + \boldsymbol{N}(\boldsymbol{x}) \tag{4.4}$$

where $\boldsymbol{Y}(\boldsymbol{x})$, $s(\boldsymbol{x})$ and $\boldsymbol{N}(\boldsymbol{x})$ correspond to the measurements, original signal and noise. $\boldsymbol{A} = [a(\theta_1), \ldots, a(\theta_K)]$ is the $N \times K$ steering matrix where K is the number of sources . Each steering vector can be written as:

$$\boldsymbol{a}(\theta) = \left[1, e^{-j2\pi\theta}, e^{-j2\pi 2\theta}, \cdots, e^{-j2\pi(N-1)\theta}\right]^T \tag{4.5}$$

When the signals and the noise are not correlated, the $N \times N$ correlation matrix is given by *Schmidt* (1986) :

$$\begin{aligned} \boldsymbol{R} &= E\left[\boldsymbol{Y}\boldsymbol{Y}^H\right] \\ &= \boldsymbol{R}_s + \sigma_0^2 \boldsymbol{I} \\ &= \boldsymbol{U}_s \boldsymbol{\Sigma}_s \boldsymbol{U}_s^H + \boldsymbol{U}_n \boldsymbol{\Sigma}_n \boldsymbol{U}_n^H \end{aligned} \tag{4.6}$$

where $\boldsymbol{R}_s$ denotes the signal covariance matrix. H denotes the conjugate transpose of the matrix. $\boldsymbol{U}_s$ is the subspace spanned by the eigenvectors related to K largest eigenvalues after eigenvalue decomposition of matrix $\boldsymbol{R}$. The rest $N-K$ eigenvalues are the minimum eigenvalues of $\boldsymbol{R}$, $\sigma_0^2 \boldsymbol{I}$

represents the covariance matrix related to the noise process. The subspace spanned by the vectors in $\boldsymbol{U}_n$ is the noise subspace which is orthogonal to the subspace $[a(\theta_1), \ldots, a(\theta_L)]$ spanned by the steering vectors:

$$\boldsymbol{a}^H(\theta)\boldsymbol{U}_n = 0 \tag{4.7}$$

The estimator which minimizes the norm $\left\|\boldsymbol{a}^H(\theta)\boldsymbol{U}_n\right\|_2$ for $a(\theta_i)$ indicates the frequency information of i^{th} sinus component. The corresponding pseudospectrum can be built as:

$$p(\theta) = \frac{1}{\|\boldsymbol{a}^H(\theta)\boldsymbol{U}_n\|_2} = \frac{1}{\boldsymbol{a}^H(\theta)\hat{\boldsymbol{U}}_n\hat{\boldsymbol{U}}_n^H\boldsymbol{a}(\theta)} \tag{4.8}$$

This function has K sharp peaks at its peak frequencies. Therefore, the sinusoidal frequency components can be determined by searching through all angles θ and finding the K highest peaks of the pseudospectrum. Accordingly, the corresponding frequency of the original signal can be calculated from the estimated angle information.

For a typical MUSIC approach, the resolution depends on the precision of the scanning angle. Alternatively, the spectrum search process can be replaced by calculating the roots of a polynomial expression. This method converts the estimation of the required parameters to the problem of finding roots of the polynomial on the unit circle, namely the Root-MUSIC method (Root-MUSIC, *Barabell* (1983)). This method can achieve higher resolution while keeping low computational cost.

4.2.2 Estimating signal parameters via rotational invariance techniques (ESPRIT)

Similar to the MUSIC method, the ESPRIT method also estimates the sinusoid frequencies by mean of eigenvalue decomposition. Differently, it utilizes the rotational invariance property from the signal subspace of the covariance matrix spanned by two time/space-shifted data vectors. This

avoids the spectrum search process in typical MUSIC method, ensuring a fast and robust estimation.

Considering two subarrays both containing m elements with known and fixed distance in between, a complex sinusoid $e^{j2\pi f_i m}$ can be shifted by one sample by multiplying an additional phase term $e^{j2\pi f_i}$. The first subarray with measurement $\boldsymbol{Y_1}$ and the second subarray with measurement $\boldsymbol{Y_2}$ can be expressed as (*Roy and Kailath*, 1989):

$$\begin{aligned}\boldsymbol{Y_1} &= [\boldsymbol{a}(\theta_1), \boldsymbol{a}(\theta_2), \cdots, \boldsymbol{a}(\theta_N)]\boldsymbol{S} + \boldsymbol{N_1} = \boldsymbol{AS} + \boldsymbol{N_1} \\ \boldsymbol{Y_2} &= \left[\boldsymbol{a}(\theta_1)e^{j2\pi f_1}, \boldsymbol{a}(\theta_2)e^{j2\pi f_2}, \cdots, \boldsymbol{a}(\theta_N)e^{j2\pi f_N}\right]\boldsymbol{S} + \boldsymbol{N_2} = \boldsymbol{A\Phi S} + \boldsymbol{N_2}\end{aligned} \tag{4.9}$$

where $\boldsymbol{\Phi} = diag\left[e^{j2\pi f_1}, e^{j2\pi f_2}, \cdots, e^{j2\pi f_K}\right]$ is a diagonal phase matrix, the elements are the relative phases between the adjacent samples of the sinusoids. Defining covariance matrix of signal array:

$$\boldsymbol{Y} = \begin{bmatrix}\boldsymbol{Y_1} \\ \boldsymbol{Y_2}\end{bmatrix} = \begin{bmatrix}\boldsymbol{A} \\ \boldsymbol{A\Phi}\end{bmatrix}\boldsymbol{S} + \boldsymbol{N} = \overline{A}\boldsymbol{S} + \boldsymbol{N} \tag{4.10}$$

the covariance matrix can be represented using the eigenvalue decomposition as:

$$\boldsymbol{R} = E\left[\boldsymbol{YY^H}\right] = \overline{A}\boldsymbol{R_s}\overline{A}^{\boldsymbol{H}} + \boldsymbol{R_N} = \boldsymbol{U}_S\boldsymbol{\Sigma}_S\boldsymbol{U}_S^H + \boldsymbol{U}_N\boldsymbol{\Sigma}_N\boldsymbol{U}_N^H \tag{4.11}$$

Assuming the K largest eigenvalues $[e_1, e_2, \cdots, e_K]$ of $\boldsymbol{R}$ to be $\boldsymbol{E_s}$, since $m \gg K$, the subspace spanned by the K largest eigenvalues and the subspace spanned by the steering vectors A are equal: $span\{\boldsymbol{U_s}\} = span\left\{\overline{A}(\theta)\right\}$. Therefore, there exists unique non-singular matrix $\boldsymbol{T}$ so that:

$$\boldsymbol{E_s} = \sum_n [e_1, e_2, \cdots, e_K] = \begin{bmatrix}\boldsymbol{E_1} \\ \boldsymbol{E_2}\end{bmatrix} = \begin{bmatrix}\boldsymbol{AT} \\ \boldsymbol{A\Phi T}\end{bmatrix} \tag{4.12}$$

where $\sum_n = I$. Submatrices $\boldsymbol{AT}$ and $\boldsymbol{A\Phi T}$ have same rank K, therefore the rank of $\boldsymbol{E_s}$ should also be K, since $\boldsymbol{E_1}$ and $\boldsymbol{E_2}$ lie in the signal subspace

spanned by the same signal:

$$span\{U_{s1}\} = span\{A(\theta)\} = span\{U_{s2}\} \tag{4.13}$$

When the array matrix $\boldsymbol{A}$ has full rank, the rotation invariance of two signal subspaces of received data from two sub arrays can be derived as:

$$\boldsymbol{U}_{s2} = \boldsymbol{U}_{s1}\boldsymbol{T}^{-1}\boldsymbol{\Phi}\boldsymbol{T} = \boldsymbol{U}_{s1}\boldsymbol{\Psi} \tag{4.14}$$

where each column of $\boldsymbol{T}$ is the eigenvectors of $\boldsymbol{\Psi}$ and matrix $\boldsymbol{\Phi}$ is the diagonal matrix consisting of eigenvalues of $\boldsymbol{\Psi}$. Once the rotation invariance matrix $\boldsymbol{\Psi}$ is calculated, the ESPRIT estimates the frequency as $\theta_i = -\arg(v_i)$ where v_i is the eigenvalue of matrix $\boldsymbol{\Psi}$ with full rank by the least square (LS) method:

$$\boldsymbol{\Psi} = \left(\boldsymbol{U}_{S1}^H \boldsymbol{U}_{S1}\right)^{-1} \boldsymbol{U}_{S1}^H \boldsymbol{U}_{S2} \tag{4.15}$$

from which the frequency can be estimated.

4.3 Numerical examples

4.3.1 Single component scenario

In this section, the performances of several selected spectral analysis methods are evaluated for single sinusoid signal in the presence of AWGN. The SNR in the simulation denotes: $SNR = \frac{A}{\sigma}$, where A is the amplitude of the collected fringe pattern and σ is the standard variance of the noise. The first scenario considers the evaluation of the frequency estimation based on the subspace methods under different SNR levels by varying σ. The spatial frequency of the simulated monochromatic emission line is set to be 50.5 fringes/cm, 50 trials are tested under each SNR condition.

Figure 4.2 displays the probability of identifying the signal frequency

correctly within 1 DFT bin (50-51 fringes/cm) with different number of samples. Both subspace methods can reach almost accuracy results when the SNR is larger than 1. The frequency estimation performance of these subspace methods are limited under lower SNR level, as indicated by *Tufts et al.* (1988). Increasing the number of samples can also improve the accuracy of the frequency estimation. The ESPRIT approach performs slightly better and more stable than the Root-MUSIC algorithm.

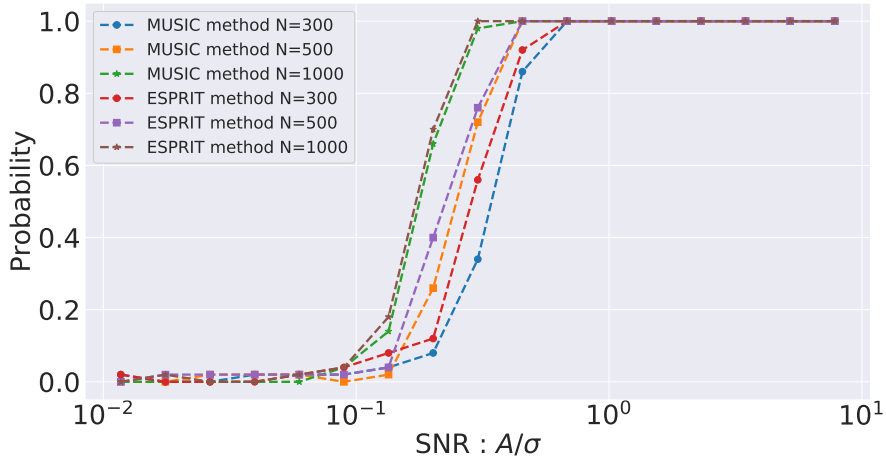

Figure 4.2: Probability of accurately estimating the signal frequency under different SNR conditions utilizing the Root-MUSIC and the ESPRIT methods. 300, 500 and 1000 pixels are included in the comparison.

Figure 4.3 shows the comparison between the estimated parameters using the subspace and the FFT for single tone scenario. Hanning apodization function is applied before applying the FFT, a good representation of the estimated spectrum is achieved via zero padding by a factor of 1000. As shown in the corresponding subplots, although both subspace methods can hardly provide the optimal results at lower SNR, their performances are slightly better than the FFT at higher SNR. The windowed FFT can only provide limited accuracy at higher SNR for frequency and phase estimation, which is possibly related to the window type and the number of

zero-padding.

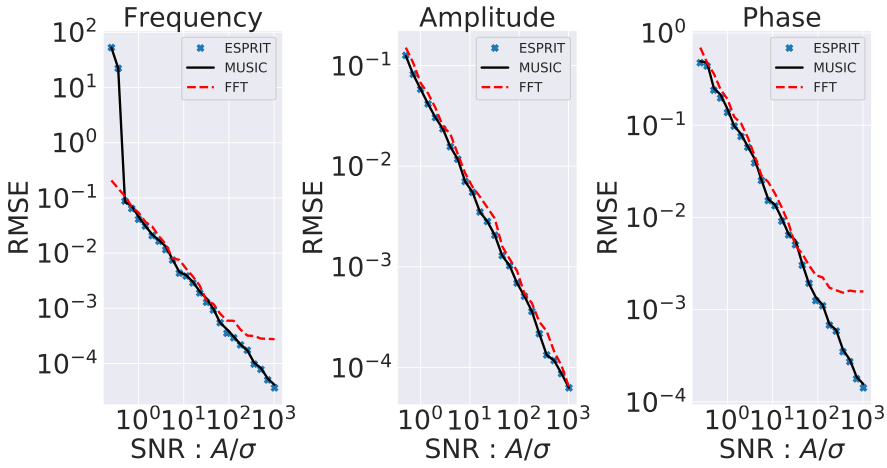

Figure 4.3: The Root-mean-square error (RMSE) of parameter estimation performance using subspace methods and FFT for single emission spectrum. The generated signal contains 500 samples with signal amplitude 1 and signal phase 0.5 radian. In order to evaluate the performance on the signal with different spatial frequencies, the frequency of the signal is set to be 100 fringes/cm plus an additional random fractional number (between 0 and 1) in each trial, total 100 trials are generated at each SNR level.

Figure 4.4 reveals the comparison between different subspace methods regarding to the time consumption with various number of samples. Despite the Root-MUSIC method avoids the search in the pseudospectrum by means of polynomial rooting, its time cost is still an order of magnitude higher than the ESPRIT method. The time consumption from two methods do not show significant SNR dependent behavior, while it is highly related to the number of measurements due to the matrix decomposition procedure. When the computational power is limited, the ESPRIT method is more preferred since the estimation can be achieved in one shot. Therefore, the ESPRIT approach is adopted and discussed in

the later sections.

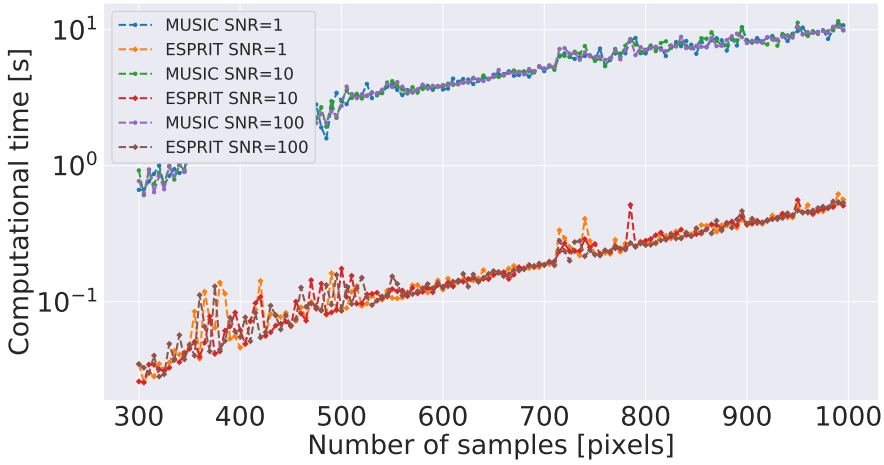

Figure 4.4: Computational time of Root-MUSIC and ESPRIT methods with various number of samples.

4.3.2 Multiple components scenario

This section mainly investigates the spectral reconstruction accuracy for the signal composed of multiple emission lines. In the first part, the generated fringe patterns contain 12 well spaced spatial frequencies starting from 50.5 fringes/cm (or 50.5 DFT bins in spectral domain). The frequencies are estimated by means of ESPRIT method where the number of emission line is provided as the a prior information. The distance between each spatial frequency is tested up to one DFT bin (1 fringes/cm).

Figure 4.5 shows the frequency reconstruction error averaged over all the estimated tones using the ESPRIT method from signals containing 300 to 700 samples. A frequency estimation error within approximate 0.1 fringes/cm can be achieved by the ESPRIT method when the components are spaced over 0.8 DFT bins, which is beyond the traditional

Fourier transformation. In addition, the subspace method does not show significant sampling number dependent behavior, therefore it can achieve high resolution even with limited samples. On the contrary, the spectral resolution based on the FFT method is directly related to the number of samples and to the utilized window functions (Table 4.1).

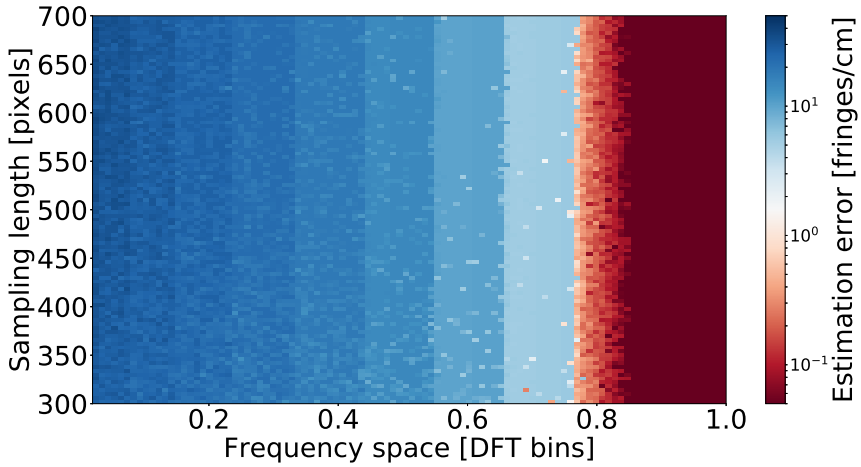

Figure 4.5: Frequency estimation for well spaced scenario with sampling length ranges from 300 to 700 in noiseless case using ESPRIT method. In this example, each interferogram contains 12 different sinusoidal signals with well-spaced spatial frequencies, the base frequency starts from 50.5 fringes/cm. Each signal component is set to be with the same amplitude and random phase.

The next part in the simulation compares the stability of the subspace and the Fourier transform methods under different SNR conditions to reconstruct 20 frequencies spaced by 2 DFT bins. This study mainly investigates their ability to discern signals at different frequencies and significantly different power levels, specifically to identify low level signals in the presence of signal with much higher intensity. The relative intensity between each component, defined as the dynamic ranges (DR), is set to be 1, 5 and 10 respectively to evaluate the algorithm performance. The

noise defined here is in reference to highest signal intensity among these emission lines.

Figure 4.6(a) displays the reconstructed frequency error with different DRs. The subspace method fails to reconstruct some of signal components under lower SNR higher DR condition, since the signal subspaces formed by these true emission lines are difficult to be completely identified. On the contrary, the Fourier transform can provide more robust performance at lower SNR. Nevertheless, without additional fitting procedure, its performance is limited due to the interference between the neighboring lines.

Regarding the amplitude estimation (Figure 4.6(b)), both methods can provide accurate performance when the dynamic range is relatively low. The amplitudes estimated from FFT become deviated when the intensity of each line differs remarkably. Even though the applied window function suppresses the side lobes to some extent, the corresponding amplitudes can not be extracted directly from the spectrum without additional interpolation or fitting procedure. In addition, the window function will also broaden the spectral main lobes, making closely located signal components more difficult to be identified.

A snapshot for the generated spectra based on different approaches is shown in Figure 4.7. The unwindowed signal (rectangular window) shows the poorest dynamic range, whereas the Hanning window function would provide better performance at the cost of reducing the spectral resolution. The Hanning windowed spectrum can be well represented by the Gaussian mixture model with determined frequency positions. Note that the prior knowledge on the component frequencies are essential in this fitting process.

Based on the subspace (ESPRIT) method, the least square estimation can provide almost unbiased amplitudes (mean amplitude reconstruction error about 0.014%). It is observed that both methods (especially the Gaussian mixture model in this simulation) sometimes lead to numerical instability (change of amplitudes between emission lines), since the

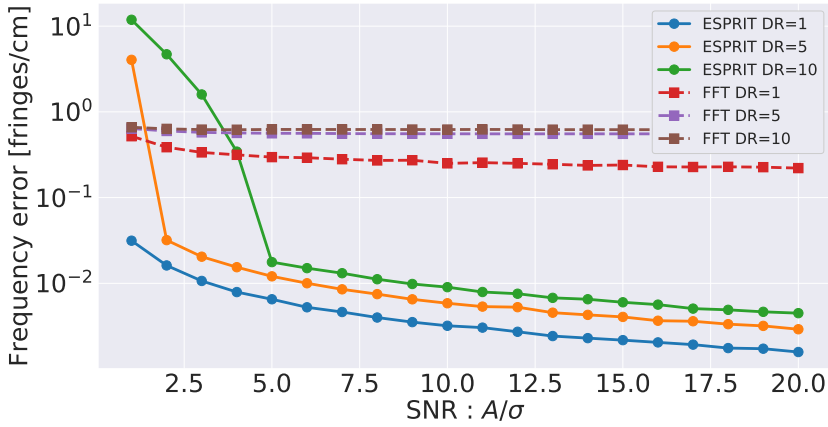

(a) Frequency estimation error

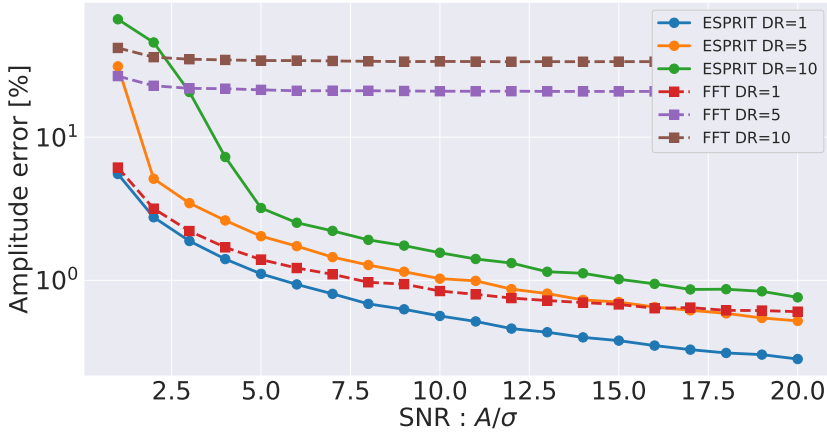

(b) Amplitude estimation error

Figure 4.6: Reconstruction error for the signal frequency and amplitude using the ESPRIT and the FFT with varying SNR, averaged over each signal component in 100 trials. The interferogram with 500 samples consists of 20 well-spaced frequencies separated by 2 DFT bins, starting from 50.5 fringes/cm. The relative intensity between each signal component is set to be 1, 5 and 10 respectively. The SNR is defined as $SNR = \frac{A_{max}}{\sigma}$, where A_{max} is the highest amplitude among the generated signal components. Zero padding by factor of 1000 and Hanning apodization function are added before FFT.

orthogonality may not maintain between closely located spectral lines. Nevertheless, based on different methods, the total energies summed over the spectral band remain identical. Identifying the intensity of each individual line with FFT can be achieved by increasing the spectral resolution, e.g. by sampling more pixels.

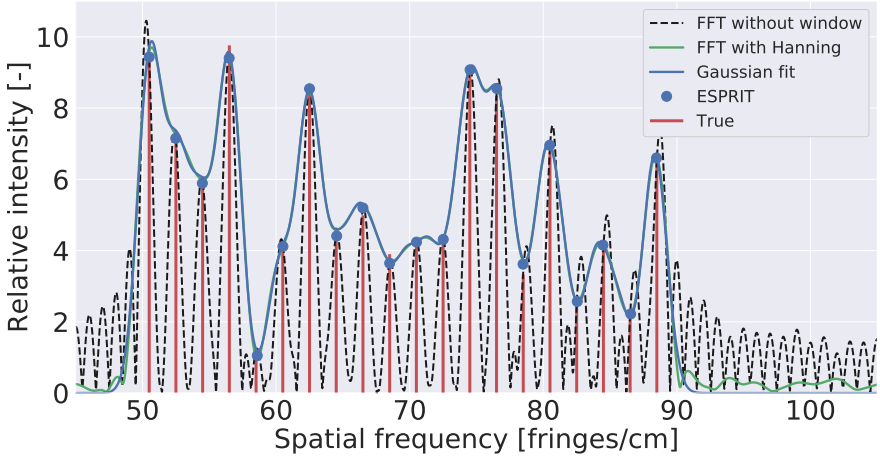

Figure 4.7: Reconstructed spectra using different methods in comparison with the input spectral intensity containing 20 well spaced components. The amplitude of each signal component is randomly generated between 1 and 10. The SNR in spatial domain is 100 and the sampling length is 500 pixels. Blue lines indicate a fitted spectrum using Gaussian mixture method with determined frequency information. Blue dots represent the amplitudes estimated from the ESPRIT method.

4.3.3 O_2A-band simulation

To further evaluate the performance of the spectral analysis in a more realistic scenario, several interferograms are generated based on the designed model parameters for AtmoSHINE instrument. In these simulations, each interferogram was generated using the O_2A-band emission lines between

763.31 and 764.28 nm (total 6 lines) with spatial frequency between 108 fringes/cm and 175 fringes/cm. Figure 4.8 shows an interferogram with 800 pixels per row obtained on the detector for emissions at night time between 86 km and 119 km based on the HITRAN database (*Gordon et al.*, 2017). Since the emission at night time is relatively low, longer integration time is required for a good measurement. In addition, 20 detector rows are summed up for each altitude bin to improve the SNR, therefore the altitude resolution is about 1.5 km for each altitude bin.

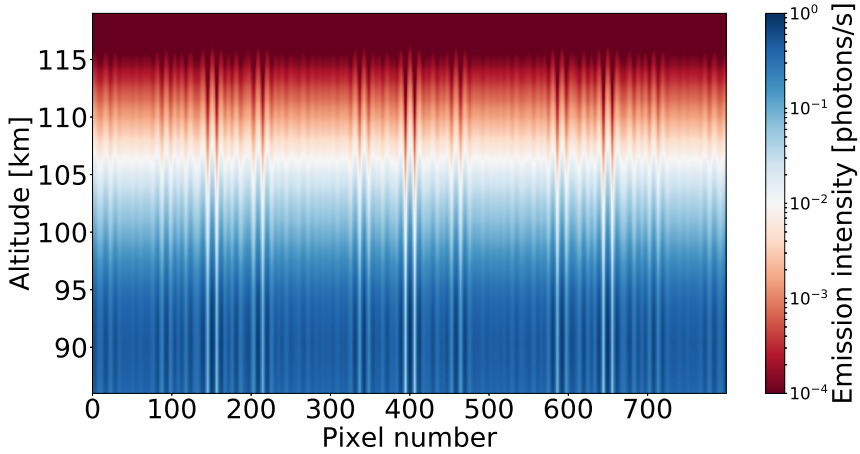

Figure 4.8: Simulated interferogram of the O_2A-band nightglow emission between 86 km and 119 km. 800 x 800 pixels are sampled on the detector localization plane. Utilized six emission lines are at: 763.31 nm, 763.43 nm, 763.73 nm, 763.84 nm, 764.17 nm and 764.28 nm. Each row contains 800 pixels.

The amplitude estimation results for different number of samples are plotted in Figure 4.9 with respect to different noise levels. A minor deviation is still present under high SNR based on the Fourier transform method, the reconstructed amplitudes error converge asymptotically to around 1%. This discrepancy is possibly related to the spectral leakage and the interferences from the adjacent lines in spectral domain. In con-

trast, the subspace arises more accurate estimation. To obtain an amplitude estimation error of 1%, the subspace methods require a SNR of 5, whereas a conventional Fourier-transform requires a 50% higher signal-to-noise ratio. A noticeable improvement can be seen on the amplitude results by increasing the number of sampling points.

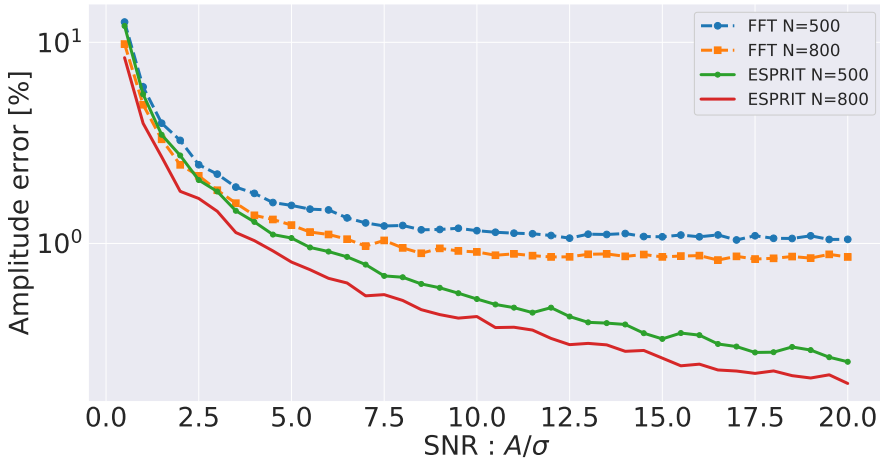

Figure 4.9: Amplitude estimation results simulated under different SNRs based on the Fourier transform method (Hanning apodization) and the subspace method (ESPRIT). The estimation error corresponds to the averaged error for 6 emission lines.

In the next scenario, the interferograms are generated by a set of broadened emission lines with different wavelengths. The broadening effect is simulated by setting a Gaussian-profile distribution of each emission line wavenumber (wavelength). The spectral broadening effect exhibits a decrease in the envelop of the fringe pattern (*Liu et al.*, 2018). Figure 4.10 shows an example of the converted spectra with one wavenumber broadening for each component. For the subspace method, 15 emission lines are assumed to imitate the spectral broadening effect.

Both methods exhibit little biased frequency localizations compared

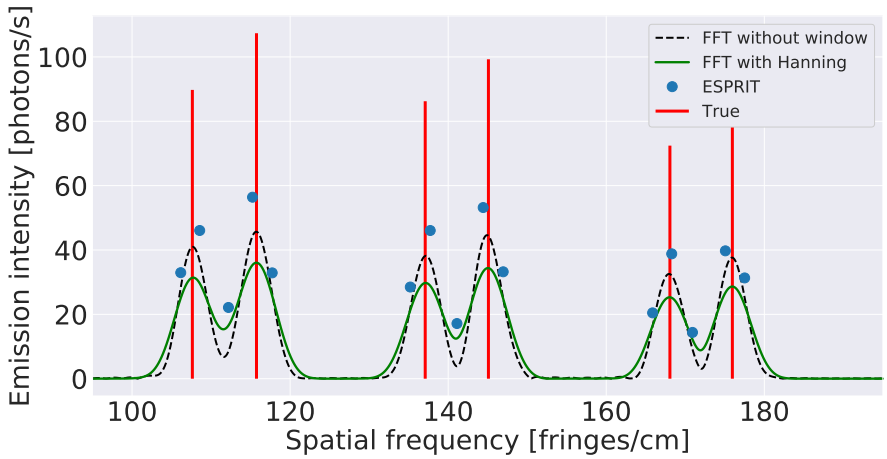

Figure 4.10: Converted spectra with one wavenumber broadening interferogram containg 800 pixels at SNR=20. The spectrum (green line) obtained from the Hanning windowed interferogram does not contain the correction using the corresponding scaling factor. For the subspace method (blue dots), 15 emission lines are assumed as the a prior information.

with their corrected peak positions. In the presence of spectral broadening effect, the peak amplitudes in the spectral domain do not correspond to the input emission intensity. Since the line spectra assumption for frequency estimation is no longer valid for the broadened spectrum, the subspace method describes the broadening effect by using multiple emission lines for each line pair. The intensities can be obtained from the sum (subspace method) or the integration (FFT) over the effective spectral range. Simulation results indicate that both methods lead to an estimation uncertainty of about 1% for the absolute value, and less than 0.5% for the relative intensity between each line pair.

When the interferogram shows large envelope variation or phase distortion, the spectral broadening effect consequently leads to the line splitting when applying conventional subspace method. Nevertheless, the sub-

space method can provide necessary frequency information for an unknown spectrum, which is especially essential when the spectral resolution based on the Fourier transform is limited. These frequencies can also be used as the initial frequency information for the spectral fitting method. When the relative ratio between emission lines needs to be addressed correctly, e.g. to derive the temperature, the Fourier transform method is practically more preferred. The analysis of the broadening effect (spectral line shape) on the real instrument will be shown in Section 5.4 .

Chapter 5

Instrument characterization and calibration

Before the atmospheric emission spectrum can be derived from the observations, the obtained raw interferograms must be processed to the corrected data. The processing steps are based on a series of calibration measurements on ground. The main objectives of the calibration procedures are to correct for the instrumental effects that arose from the design and assembly. In this study, the radiometric performance of the instrument is characterized using a blackbody. A specified calibration unit was built-up in the optical lab for detailed instrument characterization. The following sections provide specified studies on the selected characteristics including the phase and image distortion, the instrument line shape function, the spectral position and modulation efficiency (visibility) calibration as well as the ghost emission lines. These steps are demonstrated using the laboratory measurements followed by some results after correction. Last but not least, the measurement uncertainty is also evaluated in this chapter.

5.1 Radiometric characterization

In this section, the radiometric response of the instrument is investigated within the signal level of expected atmospheric emissions. Even though the atmospheric temperature retrieval from relative distribution of O_2A-band emission lines does not require a strict absolute radiometric calibration, this characterization can still provide useful information to understand the systemic input-output-response. By means of a characterized blackbody, the ratio between the incoming photons arriving at the instrument and the detected digital counts can be estimated.

The spectral radiance per unit wavelength λ from an ideal blackbody can be described based on the Planck's law as:

$$B_\lambda(\lambda, T) = \frac{2hc^2}{\lambda^5} \frac{1}{e^{\frac{hc}{\lambda k_B T}} - 1} \tag{5.1}$$

with k_B the Boltzmann constant $1.38 \times 10^{23} J \cdot K^{-1}$, h the Planck constant $6.626 \times 10^{-34} J \cdot s$, and c the speed of light. Defining the instrument etendue G which is related to the area A and the solid angle Ω of the instrument, the corresponding number of photons $N_{photons}(\lambda,\ T)$ (per second) entering the instrument can be calculated by scaling to the energy per photon $h\nu$ as:

$$N_{photons}(\lambda, T) = \frac{B_\lambda(\lambda, T)}{E(\lambda)} G = \frac{\frac{2hc^2}{\lambda^5} \frac{1}{e^{\frac{hc}{\lambda k_B T}} - 1}}{h\upsilon} G = \frac{2c}{\lambda^4} \frac{1}{e^{\frac{hc}{\lambda k_B T}} - 1} G \tag{5.2}$$

The instrument receives emissions at wavelengths between 762 nm and 765.3 nm within the optical filter range. The estimated blackbody spectral radiance at different temperatures is shown in Figure 5.1 for this wavelength region of interest. The expected limb radiance of a strong O_2A-band emission line is about $10^9 photons/s/cm^2/sr$ (*Kaufmann et al.*, 2018). For multiple emission lines in the filter range, a total intensity

should be in the order of $10^{10} photons/s/cm^2/sr$. This corresponds to the blackbody temperature of about 760 K. If the radiance at 10% of the total radiance also needs to be detected as the lower bound, the effective blackbody temperature is about 695 K.

In this measurement, the distance between the blackbody emission surface and the first lens of the instrument is about 141.5 cm, which enables the emissions from the blackbody to cover the whole FOV of the instrument. The temperature of the blackbody was tuned between 693 K and 773 K to evaluate the conversion ratio. During the experiment, the detector was cooled down to $-35°C$ to reduce the dark current by connecting the detector board to the liquid nitrogen. In the end, the corresponding dark current and detector offset were measured and subtracted before further analysis.

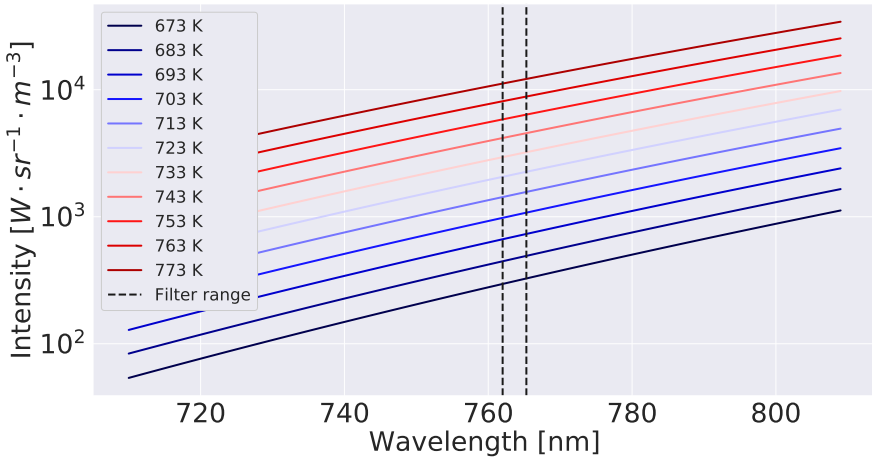

Figure 5.1: Spectral radiance estimated from an ideal blackbody at different temperatures, the dashed lines represent the optical filter range.

The expected photons from the blackbody on the instrument and the actual detected signal counts are plotted in Figure 5.2(a), based on the averaged values over the effective area of the detector (840 x 840 pixels in

the image center). The relationship between the increment of detector counts and the increasing number of photons follows the linear trend with the gradient of around 5.4 photons/count. Considering the detector quantum efficiency and the photon transfer ratio estimated in Section 2.3, the corresponding instrument optical transmission ratio is approx. 23%.

Figure 5.2(b) illustrates the distribution of the conversion ratio derived from the gradient of the linear regression analysis for each pixel, which shows quite significant variance over the field. Considering the photon loss on the filter (7%), on the beam splitter (50%) and on the gratings (20%), the system optical transmission ratio is about 37%. The characterized conversion ratio at the center area is about 3.7 photons/count, this value corresponds to 34% optical transmission ratio, which fits to the theoretical budget estimation.

The conversion ratio obtained on the image edge areas is about 9 photons/count , which corresponds to 13% optical transmission ratio. This decrease towards edges is assumed to be associated with the field curvature of the designed optics. Simulation result from optical ray-tracing software shows around 15% intensity drop over the field, the misalignment during assembly may account for the additional decrease in practice.

5.2 Interferogram generation using the calibration unit

A specified calibration source, namely the AtmoSHINE calibration unit (ACU), was built up for the on-ground calibration, as shown in Figure 5.3 for its setup. This calibration unit is able to provide the emission similar to that from the atmosphere, which fulfills the requirements regarding virtually homogeneous scene (infinity) and plane wave configuration over the full FOV. A fore optics subsystem images the emission from the laser source onto a spot on the diffusor, where the spatial coherence of the laser

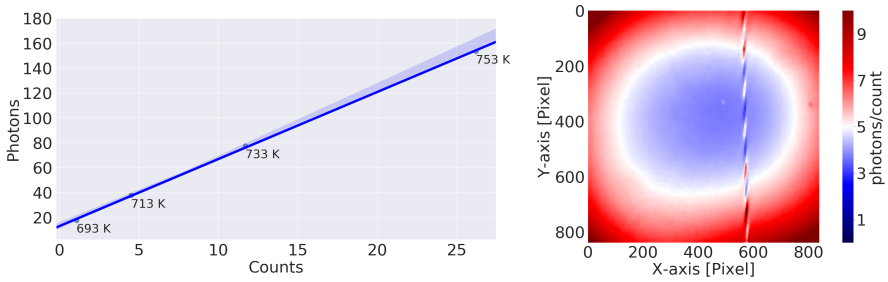

(a) Photon counts curve obtained at different blackbody temperatures

(b) Photon counts distribution estimated for each pixel

Figure 5.2: Estimation of photon-to-count conversion ratio. (a): Measurements with different temperatures. Each value represents the results averaged over the effective area (840x840 pixels) on the detector. (b): Conversion ratio derived from the gradient of the linear regression analysis for each pixel. The vertical "barber pole" corresponds to the location of the zero-order interference.

light is removed. A homogenous illumination is achieved using an optic subsystem containing micro lens array. The homogenous scene is then set to infinity such that the aperture of the instrument is uniformly illuminated by plane waves virtually from infinity.

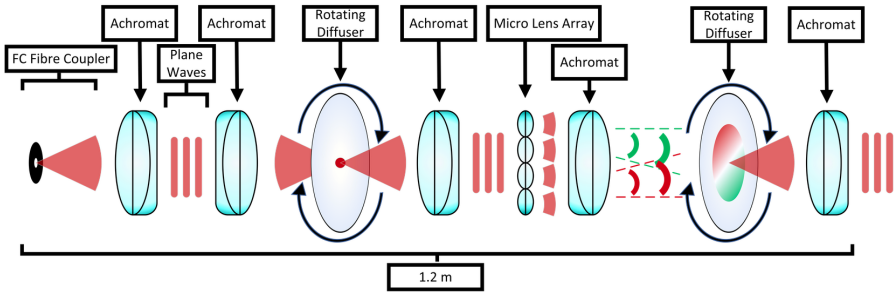

Figure 5.3: AtmoSHINE calibration unit (ACU) setup.

Following *Englert and Harlander* (2006), the flatfield of each arm was measured one by one with another arm blocked to verify the instrument inhomogeneity. The instrument was illuminated by a tunable laser with emission line inside the filter range. Each illuminated scene in Figure 5.4 covers a round shape with a diameter of about 500 pixels on the detector. Compared with the radiometric characterization result using the blackbody (Figure 5.2(b)), the recorded images with the ACU setup are more homogeneous within the circular areas. Specifically, the flatfields at row 450 are displayed in Figure 5.5 where the two arms are well balanced within the 10% intensity drop region. The relative intensity between two arms are 51% and 49%, respectively.

Since the output shape of the ACU is not fully characterized so far, its contribution on the obtained flatfield can hardly be extracted from the measurements. Each flatfield measurement is actually the superposition of the ACU output shape and the instrument flatfield. In this case, the measured flatfield images are not suitable for practical correction. Alternatively, the radiometric measurements are used to correct for the instrument inhomogeneity, with zero-order interference pattern replaced by a series of interpolated points for each row. The modulation efficiency variation caused by the unbalanced arms is corrected in the visibility calibration.

During the experiment, some of the interferograms were over exposed, which generates additional saturated areas on the obtained interferograms. An example of the interferogram containing 840x840 pixels at 762.39 nm is shown in Figure 5.6. The saturation effect will create the discontinuity of the interferogram and therefore generate side lobes and harmonics in the Fourier transformed spectrum. This effect is more serious for lower spatial frequency signal since more saturated pixels will occur per period. The influence of the saturation effect on the spectral intensity will be addressed in Section 5.7.

The tilt of the interferogram is the consequence of rotating the gratings in the assembly procedure. Note that this tilt cannot be removed by image rotation due to its wavelength dependency and related smearing in

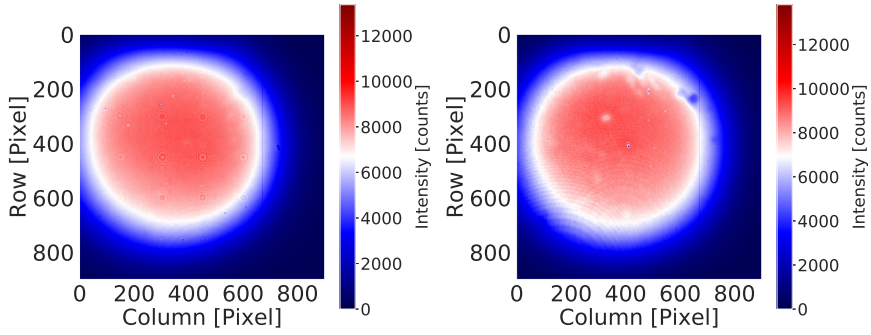

(a) Measurement of arm 1 (b) Measurement of arm 2

Figure 5.4: AtmoSHINE flatfield measurements using laser and ACU configuration. Each flatfield was generated with another arm blocked.

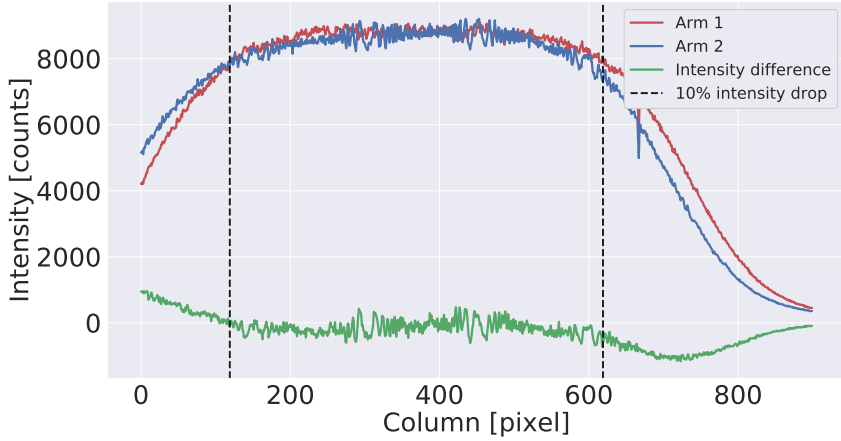

Figure 5.5: Intensity of two arms at row 450. Dashed lines indicate the edges where the intensity drop to 90% of the highest value. The relative intensity is about 51% and 49% for two arms within the dashed region. Green curve indicates the intensity difference between two arms.

the vertical information. Instead of applying spatial binning which might

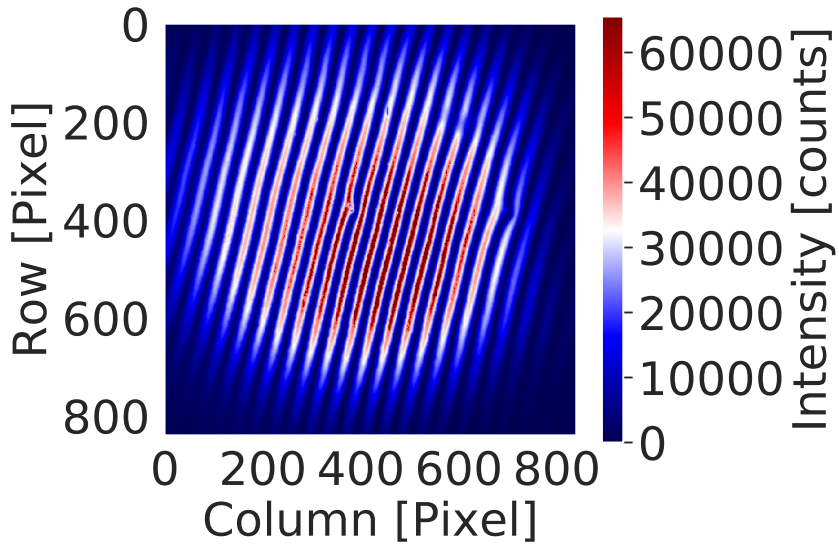

Figure 5.6: Raw interferogram containing 840x840 pixels at 762.39 nm.

decrease the visibility of the binned fringes, measurement binning can be still be made in spectral domain. With such a rotating configuration, the ghost lines from other side of Littrow can be separated using 2 dimensional Fourier transform, which will be shown later in Section 5.5.

5.3 Distortion correction

The designed system shows a significant optical distortion mainly introduced by the distortion of the detector optics, which is both frequency and location dependent, as indicated in Chapter 3 for the simulated scenario. With the tunable laser, the interferograms at different wavelengths within the filter range were generated with the ACU setup to characterize the interferogram distortion effect on the real instrument. The first step in the analysis is to estimate the distortion parameter from a set of interfero-

grams utilizing the one-parameter division model. Estimation procedures for parameter determination are quite similar to those used for the estimation on the simulated data based on line features.

Figure 5.7 shows a plot for the estimated model parameters with respect to different spatial frequencies. The distortion parameters obtained from different interferograms reveal almost no wavelength dependency. Defining the distortion in percent as: $distortion(\%) = 100 \times \frac{r_d - r_u}{r_u}$ of the farthest point in each interferogram, the overall percentage is around 7.5%. This consistency inside the narrow bandwidth region allows the interferograms with different spatial frequencies to be corrected with the same model parameter, which is also valid for interferograms containing multiple emission lines. Comparing with the similar study on the simulated interferograms in Figure 3.7, the estimated parameters are more identical over the whole filter region. The modulation depth of the interferogram from the practical instrument is greater than that from the simulation, the curved features are therefore easier to be detected.

Another kind of phase distortion reveals a mainly localized effect (*Englert et al.*, 2004). This distortion can be characterized on the obtained interferogram row by row, since this wavelength-independent phase distortion is only a function of detector position. Once the phase curves are estimated, the correction of a phase distorted interferogram can be made in spatial domain via multiplying with this phase function. As a comprehensive analysis, the performance of sequentially applying the image distortion correction and the wavelength-independent phase distortion correction are investigated.

The parameter used in the division model for the interferogram distortion correction is the mean value of parameters of 6 emission lines. To correct for the phase distortion related to the position in the localization plane, phase functions are obtained row by row from interferogram at 763.65 nm (130 fringes/cm), this correction technique is implemented after interferogram distortion correction. The wavelength-dependent phase shift will not deviate the spectrum once the absolute value in spectral domain is taken (*Englert et al.*, 2004), therefore it will not be included

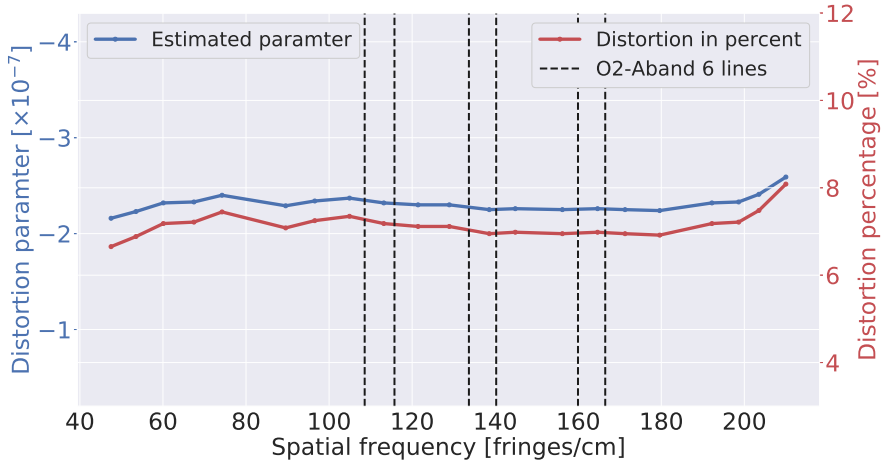

Figure 5.7: Estimated distortion parameters from the interferograms generated between 762.29 nm and 765.01 nm. Dashed lines represent the corresponding spatial frequency of 6 O_2A-band emission lines for the temperature retrieval.

in the correction.

As can be seen in Figure 5.8(a) for the uncorrected phase residuals in one row, the optical distortion is the major factor of the overall phase variation, which is more remarkable at longer wavelengths. In this case, utilizing the image distortion correction is able to generate stable phase functions within 500 pixels range. The phase functions on two sides of the curves bend down to negative regions, which are the main residuals after interferogram distortion correction. In addition, some local distortion effects can also be observed on the measured phase, e.g. around column 670 in the plots. The corresponding interferogram phase can be well corrected when two correction techniques are applied sequentially.

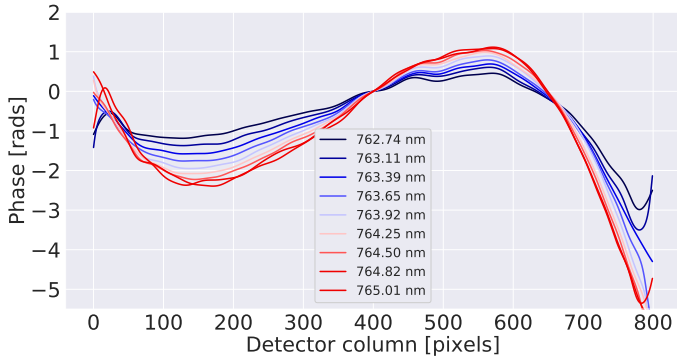

(a) Without any correction

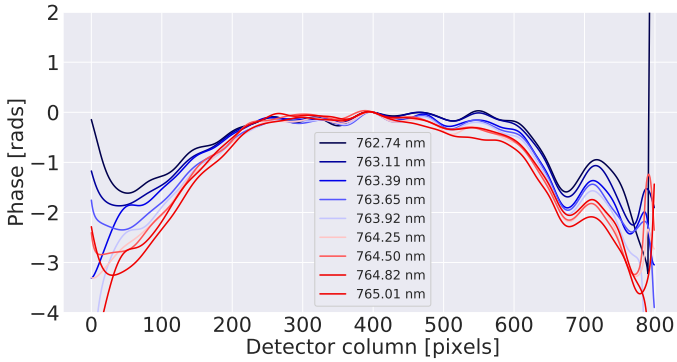

(b) Image distortion correction

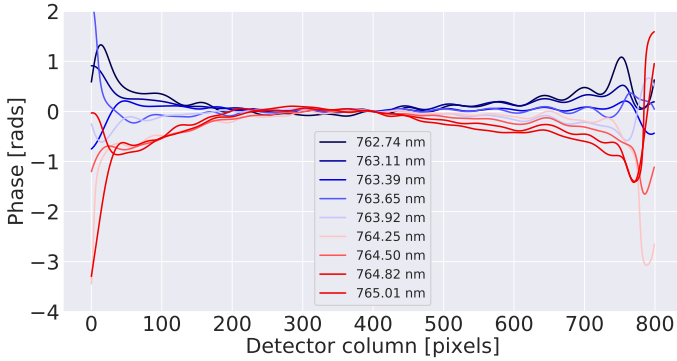

(c) Image and phase distortion correction

Figure 5.8: Phase residuals using different correction techniques for a set of emission lines at row 400. Phase curves are normalized to zero at the center position. Phase function characterized at 763.65 nm is used for the wavelength independent phase distortion correction. When both corrections are applied, image distortion correction is implemented ahead of phase distortion correction.

5.4 Instrument line shape

The instrument line shape (ILS) function indicates the normalized intensity distribution that the spectrometer would record from a monochromatic source. For an ideal SHS instrument, the fringe pattern on its own is perfectly symmetric after Fourier transform and does not shift the apparent location of the emission line. An ideal instrument line shape function in a FTS is associated with the Fourier transform of the apodization functions. Their spectral shape and the FWHM are investigated in Chapter 4. Though carefully designed and constructed, the SHS instruments are still subject to imperfections which affect the recorded interferogram and consequently create irregular spectrum.

Figure 5.9 shows the extracted instrument line shape functions from measurements with a monochromatic laser source at different wavelengths. The spectra are shown for row 400 from interferograms containing 840x840 pixels without apodization function. In these plots, the intensity of each emission spectrum is normalized to 1 for the comparison. The FWHMs of the ILS main lobes measured in spectral domain are almost identical. The measurements appear to show that this instrument has an asymmetric ILS. According to the study in Section 5.3, in addition to the local phase distortion effect, this asymmetry is mainly associated with the interferogram distortion. The pincushion distortion generates the spectrum containing lower spatial frequency component. Therefore the interferograms become more asymmetric, when more pixels from boundary regions are included.

Figure 5.10 displays the spectral line shapes converted from 700 pixels at row 550 after applying the image distortion correction and the phase distortion correction. The two side lobes become more symmetric after image distortion correction. The phase correction can further fine-tune the spectral line shapes to compensate for the rest phase distortion. The ILS for each emission line after corrections is closer to an ideal Sinc function converted from Fourier transform with rectangle apodization function.

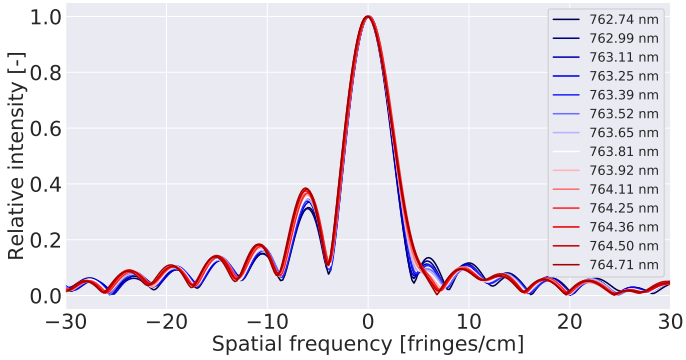

(a) ILS at row 400 with 600 samples without any correction

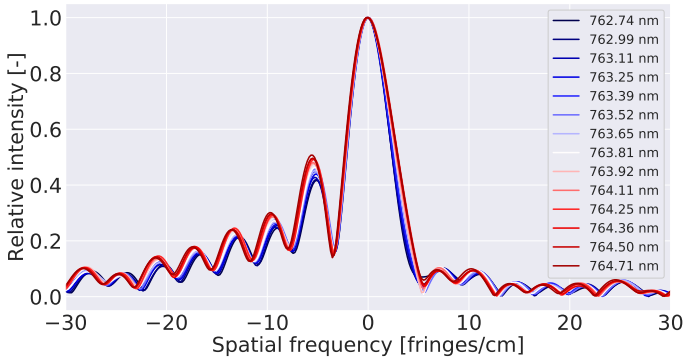

(b) ILS at row 400 with 700 samples without any correction

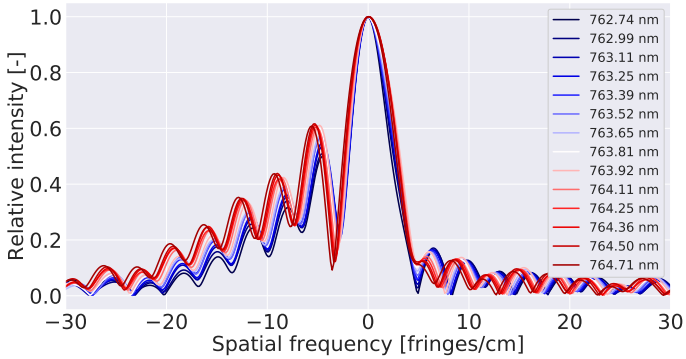

(c) ILS at row 400 with 800 samples without any correction

Figure 5.9: Instrumental line shape as obtained from laboratory measurements without apodization at row 400 with different number of samples. The spatial frequency of each emission line is normalized to 0 in the comparison.

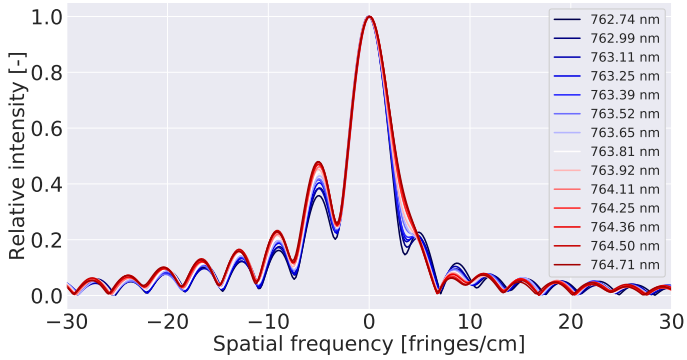

(a) ILS at row 550 with 700 samples without any correction

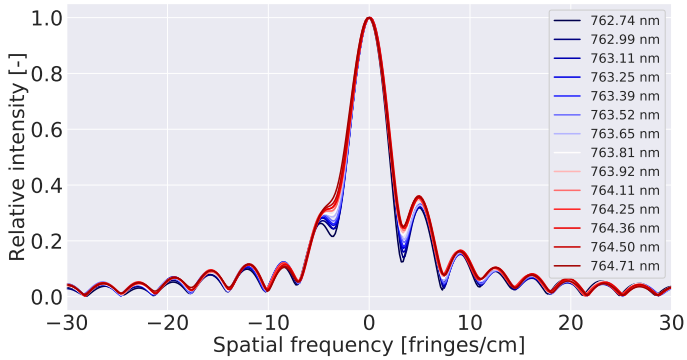

(b) ILS at row 550 with 700 samples with image distortion correction

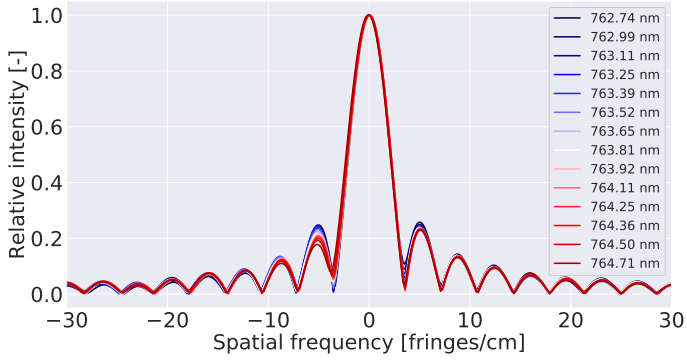

(c) ILS at row 550 with 700 samples with image and phase distortion correction

Figure 5.10: Instrument line shape functions without apodization at row 550 with different correction techniques. Phase curves measured at 763.25 nm is used for the localized phase distortion correction. The spatial frequency of each emission line is normalized to 0 in the comparison.

Figure 5.11 reveals the spectra from the composed interferograms containing emission lines at 763.65 nm and 763.81 nm with different techniques. The uncorrected spectrum shows evident side lobe effect on the left side. Accordingly, the left spectral peak shows relative higher intensity, which is mainly introduced by the low spatial frequency component from the right spectral peak due to the distortion effect. The obtained spectra after applying image distortion corrections result in higher spatial resolution. Applying the phase distortion correction after image distortion correction can produce a more concentrated spectral shape. The difference between the integrated spectral intensities using different correction techniques is about 2%.

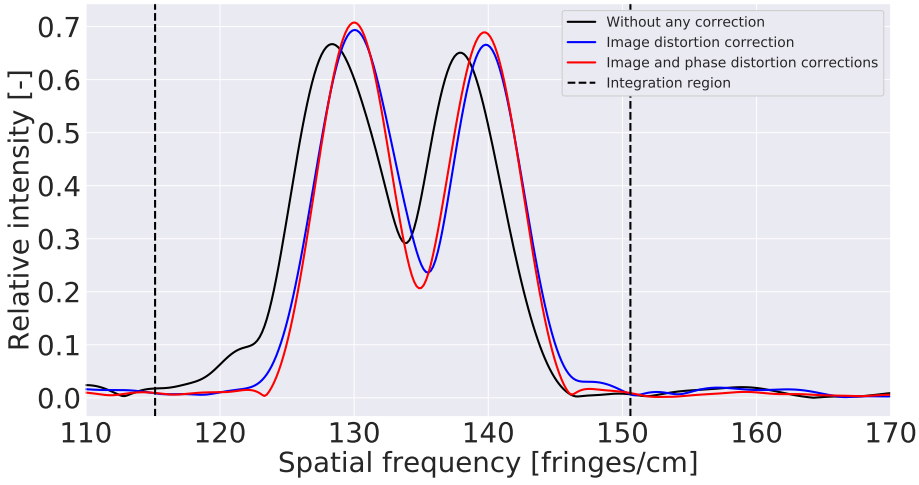

Figure 5.11: Spectra obtained via composed interferograms consisting of emission lines at 763.65 nm and 763.81 nm. The Hamming function is used as the apodization function on the 700 pixels. Dashed lines indicate the integration region to calculate the total intensity.

5.5 Ghost lines correction

For a typical SHS instrument, the emission line on both sides of the Littrow can create the same spatial frequency component in spectral domain. The unwanted emission lines in spectral domain are sometimes called the ghosts, which will affect the required spectrum for scientific analysis. Usually this effect can be avoided by setting the optical filter bandpass on one side of the Littrow. Alternatively, interferograms from the two sides of the Littrow wavelength can be distinguished by slightly tilting the gratings by a certain angle in the direction perpendicular to the interference plane. The interferograms therefore exhibit different orientations for the emission lines from the left or right side of the Littrow wavelength. The clockwise and counter-clockwise rotations correspond to different quadrants of the two dimensional Fourier transformed (2D FFT) spectrum, which makes the removal or separation possible.

Figure 5.12(a) shows a composed interferogram consisting of two emission lines: 760.04 nm at the shorter wavelength region of the Littrow wavelength (761.5 nm) and 761.79 nm at the longer wavelength region. The 2D FFT is applied to separate the emission lines, and the corresponding recovered interferogram at longer wavelength side of Littrow is displayed in 5.12(b). Note that after separation a weak interference strip around column 450 still preserves, it consists of some remaining low frequency components after processing. The Fourier transformed spectrum after ghost removal is shown in Figure 5.13, which illustrates nearly the same result as that converted from the original single emission interferogram. The peak intensity at around 17 fringes/cm differs only within 0.2% before and after correction .

5.6 Littrow calibration

The spatial frequency f_i of an interferogram obtained on the detector localization plane is dependent on the wavenumber of emission line σ_i,

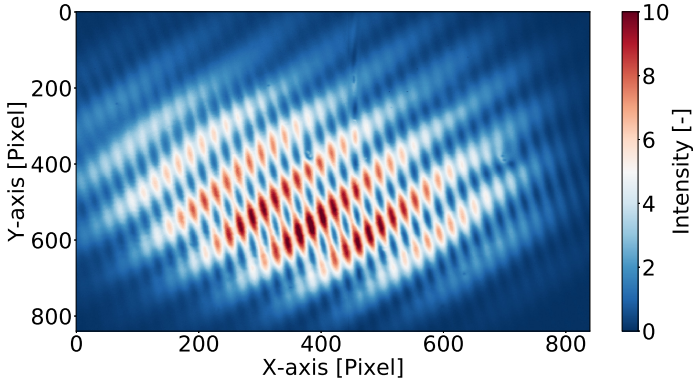

(a) Interferogram before ghost removal

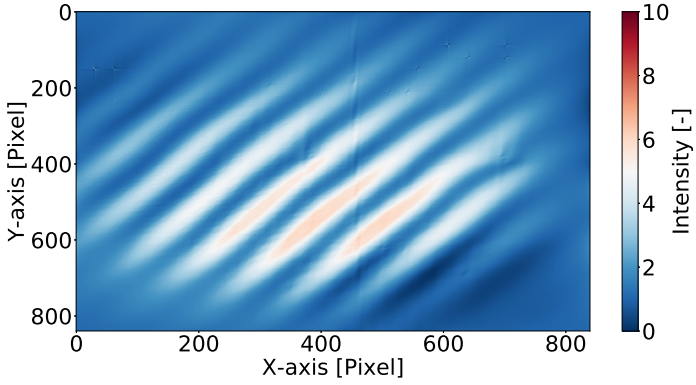

(b) Interferogram after ghost removal

Figure 5.12: (a): Composed interferograms with emissions at 760.04 nm and 761.79 nm. The Littrow wavelength is about 761.5 nm. (b) Separated interferogram based on 2D FFT, the remaining emission line is 761.79 nm.

which can be expressed as follows:

$$\begin{aligned} f_i &= 4\,(\sigma_i - \sigma_l)\tan\theta_l M \\ &= 4\tan\theta_l \sigma_i M - 4\tan\theta_l \sigma_l M \\ &= k\sigma_i + b \end{aligned} \tag{5.3}$$

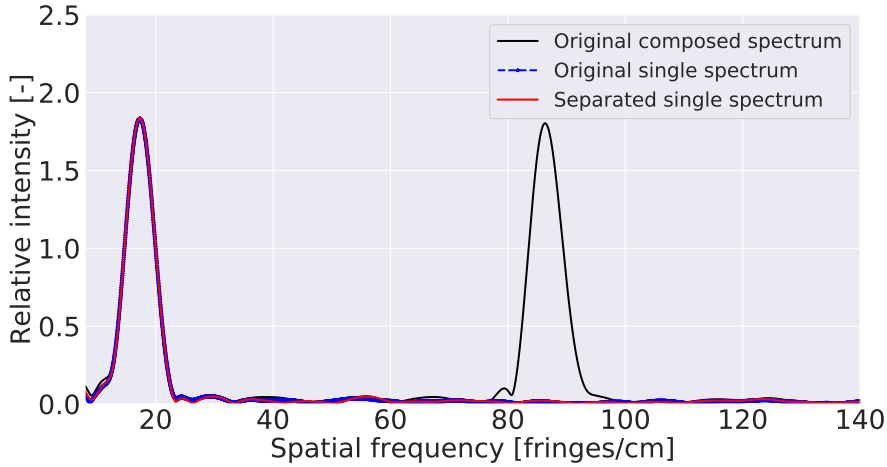

Figure 5.13: Ghost emission line correction. Black curve: original composed spectrum from two components. Blue dashed curve: original single line spectrum. Red curve: the spectrum separated by 2D FFT. Row 600 is shown for the demonstration, hamming function and zero-padding are applied before transformation.

where M is the magnification factor of the detector optics, σ_l represents the Littrow wavenumber, which follows the relation with the Littrow angle θ_l:

$$\sin\theta_l = \frac{m}{2d\sigma_l} \tag{5.4}$$

with m the diffraction order and $\frac{1}{d}$ the grating groove density. Characterization of three unknown parameters (σ_l, θ_l, M) is possible by measuring the interferograms via adjusting multiple laser wavelengths. Accordingly, the unknown parameters can be estimated based on the gradient k and the bias b obtained from the linear regression analysis.

The spatial frequency of each interferogram is estimated using the subspace method, or by detecting the corresponding peaks of the Fourier transformed spectrum with zero-padding. The regression analysis in Figure 5.14 indicates that the estimated Littrow wavenumber is 13132 cm^{-1}

at room temperature in air, which is larger than the designed value 13127 cm^{-1}. The corresponding Littrow angle from the regression analysis is 27.2°, and the magnification factor of the detector optics is about 1.72. Since the space between optical components of the SHS is filled with air under laboratory conditions, the pressure dependent refractive index change needs to be considered for measurements under vacuum condition, which has about 0.1 nm shift towards shorter wavelengths.

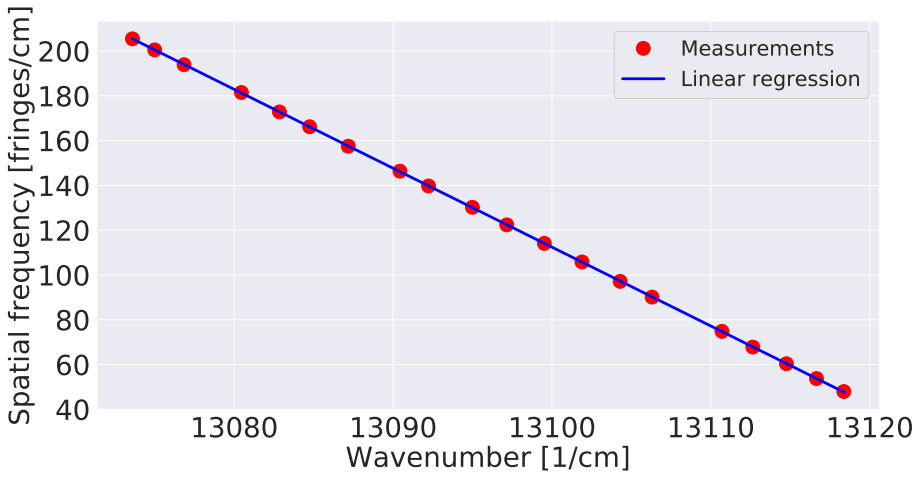

Figure 5.14: Spatial frequency of the interferogram from a set of laser wavelengths between 762.29 *nm* and 765.41 *nm*. The data was obtained under laboratory condition at room temperature, in air. The zero crossing is 13132 cm^{-1} or 761.5 *nm*.

5.7 Visibility calibration

In practice, not all the incoming photons can be fully modulated in an SHS system, accurate estimation of the real emission line intensity and the atmospheric temperature highly relies on the characterization of the

ratio between the modulated part and the unmodulated part in an interferogram. The visibility function of an SHS system describes the system modulation efficiency (ME) variation for different spatial frequencies. In this instrument, this variation is mainly associated to the modulation transfer function (MTF) of the detector optics. Besides, the system visibility is also limited by the imbalance of the beam splitter, local defects on the gratings, the MTF effect of the utilized detector as well as other artifacts during assembly. Identification of the system visibility is the key procedure to obtain the correct spectral information at different wavelengths.

To characterize the visibility variation of the obtained fringe pattern on the detector, the Hilbert transform is used for the envelope estimation (*Liu et al.*, 2018). The Hilbert transform of a real valued function $y(x)$ can be deemed as a following linear convolution with a filter function $h(x) = \frac{1}{\pi x}$:

$$\hat{y}(x) = h(x) * y(x) \tag{5.5}$$

This corresponds to a $\frac{\pi}{2}$ phase delay for positive components and a $\frac{\pi}{2}$ phase forward for negative components in the spectral domain. When the analytic signal $z(x) = y(x) + j\hat{y}(x)$ that consists of the real interferogram signal $y(x)$ and the corresponding Hilbert transform $\hat{y}(x)$ is adopted, the interferogram envelope can be derived straightforwardly based on the following relation:

$$A(x) = \left(y^2(x) + \hat{y}^2(x)\right)^{\frac{1}{2}} \tag{5.6}$$

Figure 5.15 displays several 1-D fringes along with the detected envelopes at different wavelengths. These envelopes in the subplots reveal a gradual decline in the signal fringe contrast as they move further away from the signal center position. This indicates a inhomogeneous distribution of the signal modulation effect. As shown in the estimated envelopes at higher wavelengths, the corresponding envelopes are relatively low, which coincides with the decrease of the MTF at higher spatial frequencies. For an interferogram containing monochromatic emission line, the correction can be made directly by dividing the envelope function on the

measured signal.

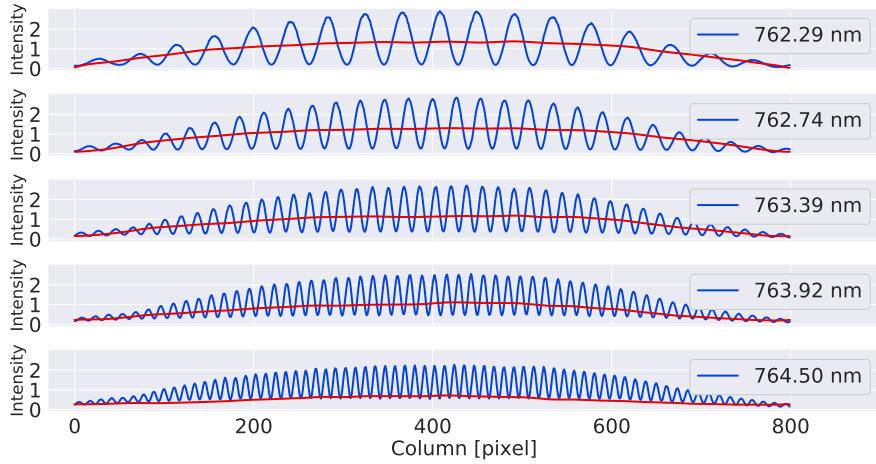

Figure 5.15: Interferograms and their envelopes at different wavelengths on the detector. The blue curve in each subplot represents the fringe pattern on one row, the red curve shows the estimated signal envelope using the Hilbert transform. The mean intensity of each signal is normalized to 1 for the comparison.

Regarding the interferograms containing multiple emission lines, the correction can be made in spectral domain once the corresponding visibility correction factor is obtained with the tunable laser. A demonstration of the visibility measurements is shown in Figure 5.16 in spectral domain from the measured fringes at several wavelengths. Since some interferograms at lower spatial frequency region are saturated during measurements (e.g. Figure 5.6), this discontinuity results in the integer multiples (overtone) of the fundamental frequency of the emission spectrum, as can be seen between 100 and 150 fringes/cm frequency region (relative intensity below 0.02). This will create uncertainties in the characterized visibility function. Note that this integer harmonic effect will not occur in real observations with the signal level below saturation region. For the interested emission lines, the deviation of the spectrum obtained by using

different sampling points (500, 600, 700 pixels shown in Figure 5.16) is about 1%.

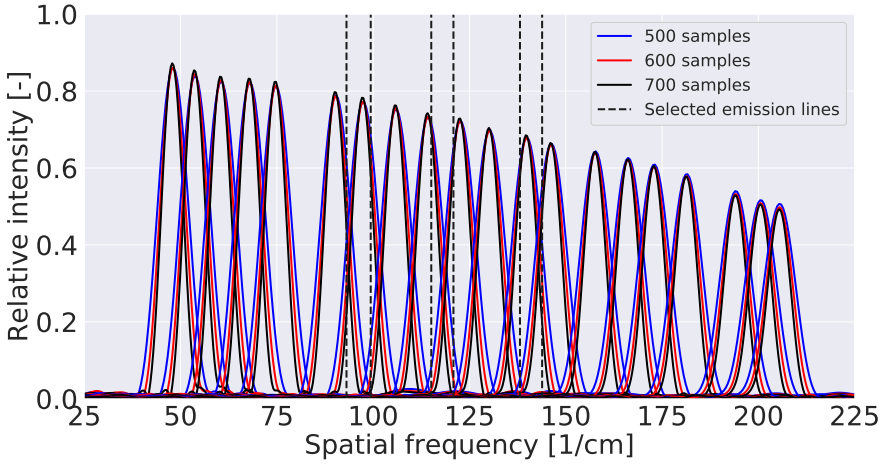

Figure 5.16: Visibility function shown at row 600 for measured wavelength using tunable laser. The dashed lines represent the six O_2A-band emission lines used for temperature retrieval. For each fringe pattern in spatial domain, a Gaussian fit is used for the flatfielding correction. Image distortion correction and phase correction are applied before Fourier transformation. The sampling center is always the row center.

Figure 5.17 shows the visibility calibration matrix obtained at different detector rows, where an overall decrement of the efficiency towards higher spatial frequencies component can be observed. The visibility at the center area of the localization plane is higher than in the upper and lower regions, which indicates a drop of modulation performance on the edges of the optics. Besides, the variation of the modulation efficiency also shows some local effects, e.g. around row 320, which might be associated with the grating defect.

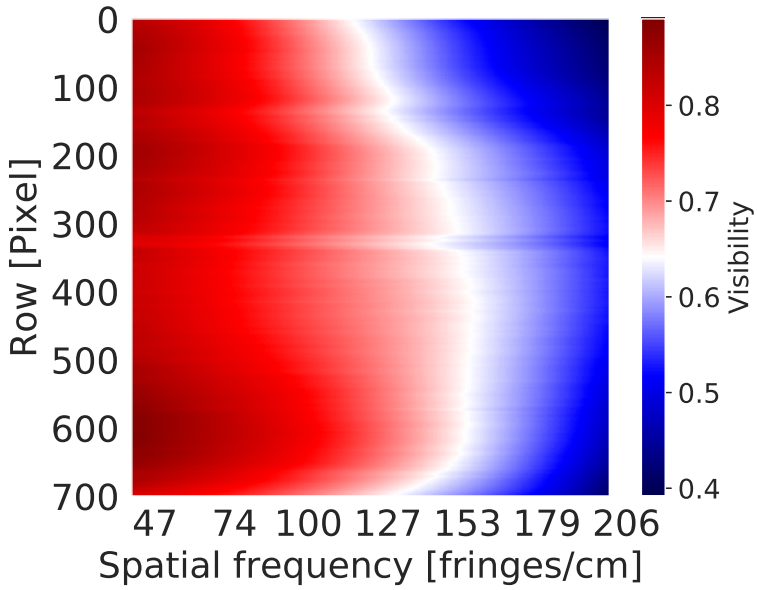

Figure 5.17: Relative calibration matrix at different spatial frequencies on the detector rows with 600 pixels. The plot shows the interpolated results at different spatial frequencies based on the measured spectra. Six emission lines for the temperature retrieval correspond to spatial frequency between 110 fringes/cm and 170 fringe/cm.

5.8 Uncertainty estimation

As a practical consideration, the measurement error which is embedded in the system during measurements depends on many experimental factors as well as instrumental configurations. Depending on different sources of error, the instrument uncertainty estimation is performed on two specific components: (a) the uncertainty of the measurement under different SNR levels and (b) the uncertainty in the calibration procedure.

5.8.1 SNR estimation

Firstly, the expected SNR is estimated for an in-orbit observation scenario with different integration times. For a CMOS image sensor, the SNR represents the ratio of the original signal to the unwanted noise combined with the undesirable electronic signal components and the inherent natural variation when counting photon flux. For this instrument, the noise is mainly caused by three parts: the detector dark current, the shot noise and the readout noise. Assuming the incoming number of photons arriving at the detector is constant under the integration time T, the SNR can be given by:

$$SNR = \frac{QI_{ph}T}{\sqrt{QI_{ph}T + I_{dc}T + \sigma_{re}^2}} \tag{5.7}$$

where I_{ph} is the incoming photons on the detector per second and I_{dc} is the detector dark current in electrons. Comparing with other noise sources, the detector readout noise is relatively low and does not increase with the increasing integration time. In this analysis, the quantum efficiency Q is considered to be constant within the measured emission lines (about 3 nm). σ_{re} represents the standard deviation of the corresponding readout noise. When the measured light signal is orders of magnitude higher than other noise sources in the observation, the system can be considered to be shot noise limited.

When the instrument operates at about 1000 km altitude, each detector row records approximately 0.1 km atmospheric vertical information, therefore 20 rows are binned for each 2 km altitude bin. As a rough estimation for 13 night glow emission lines inside the filter range, their averaged intensities are about 8×10^8 $photons\ cm^{-2}sr^{-1}s^{-1}$ for each 2 km layer. The overall optical transmission efficiency is considered to be about 25% based on the radiometric calibration measurements (Figure 5.2(b)). In this estimation, the detector characteristics are based on the experimental results in Chapter 2. The detector dark current is estimated up to $40°C$ according to the dark current model parameter. 840 rows and

840 columns are considered to be the effective image area on the detector.

Figure 5.18 illustrates the estimated measurement SNR with integration time up to 60s with 20 rows binning. The detector dark current does not show significant effect on the SNR once the detector temperature is well below $10°C$. When the shot noise is the main noise source in this system, the SNR for each line is dominated by the shot noise multiplexing effect from the emission lines in the filter band.

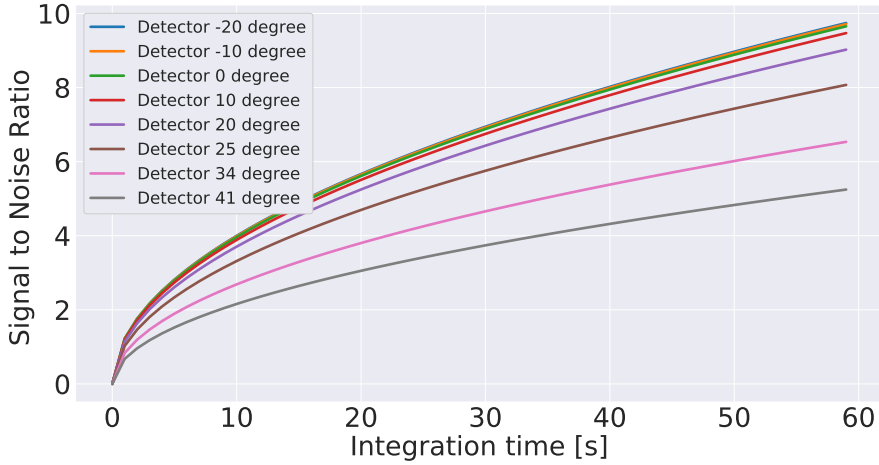

Figure 5.18: Estimated SNR in spatial domain for each emission line at night time with 20 rows binning, 840 pixels for each row. The SNR is defined by the intensity of each emission line divided by the the standard derivation σ of the AWGN. 13 night glow emission lines inside the filter range are considered, the mean intensity of each line is about 8×10^8 $photons\ cm^{-2}sr^{-1}s^{-1}$ for each 2 km layer.

The corresponding SNR of each emission component in spectral domain is considered based on the sampling length and the utilized apodization function, as introduced in Section 4.1. The Fourier transform without apodization function enables the SNR of an emission line in spectral domain to be improved by a factor of $\sqrt{\frac{N}{2}}$ with N samples in spatial domain.

In addition, the accumulated noise level in the spectrum may vary when different apodization functions are used, as shown in Figure 5.19. In this scenario, a SNR of about 80 in spectral domain can be achieved when the integration time is set between 10s and 20s depending on the utilized apodization functions.

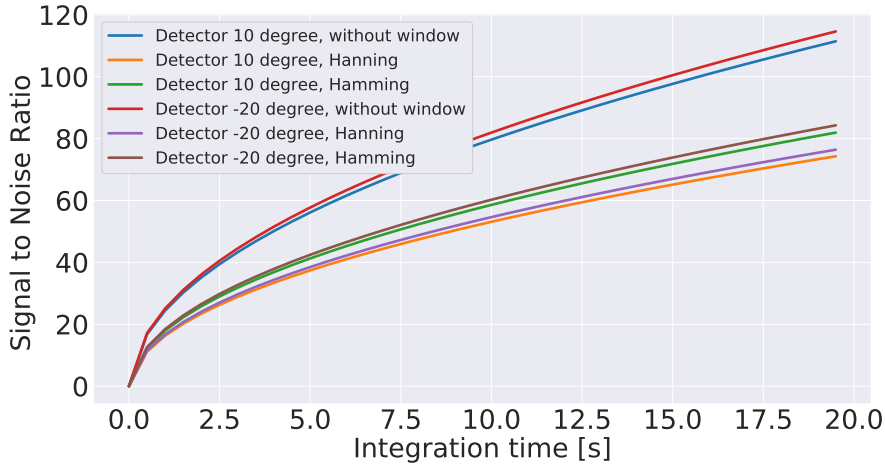

Figure 5.19: Estimated SNR in spectral domain with different apodization functions. Similar to Figure 5.18, each row contains 840 pixels, and 20 rows are binned to improve the SNR. The spectral leakage and the interference from other emission lines are not considered in this evaluation.

5.8.2 Calibration uncertainty

In this section, the uncertainty of the measurements is analyzed and summarized for individual calibration procedure, as summarized in Table 5.1. Since most calibration procedures are made on ground and used in orbit under different pressure and temperature conditions, this might reveal some discrepancy for the measurements in orbit. Without specific indication, the uncertainty analyzed here is mainly based on the instrument

performance on ground.

Table 5.1: **Uncertainty estimation on the spectral intensity**

Component	Item	Uncertainty	Remarks
Detector	PRNU	-	calibrated
	offset	-	DC component
Flatfield	envelope variation	-	spectral broadening
Image distortion	ILS	0-2%	integrated intensity
Phase distortion	ILS	0-2%	integrated intensity
Filter	Ghosts correction	0.2%	-
Visibility calibration	saturation effect	0% - 2%	6 emission lines
	sampling number	1%	500-700 pixels

The manual calibration mode of the detector enables the correction of the detector gain variation for each column, therefore the photon response non-uniformity (PRNU) will also not affect the obtained interferogram. The detector offset serve as added noise on the obtained interferogram. This offset pattern is usually not modulated, therefore it only contributes to DC component or low spatial frequency components in frequency domain. If the emission lines for temperature retrieval are not placed in the low spatial frequency region, their corresponding spectra will not be deviated by the detector offset even without subtraction.

The flatfield is affected by the anomalies presented in the optical components, e.g. the intrinsic pixel-to-pixel sensitivity variation. This non-uniformity will produce additional multiplicative factor on the obtained interferogram as a localized effect. The flatfield of this instrument mainly exhibits a decrease of the interferogram intensity away from the optical center. This effect leads to the spectral broadening effect, which is similar to the result of adding window functions. If the flatfield of the instrument is not well corrected, instead of obtaining a line spectrum for an ideal emission line, its intensity will be redistributed around its original frequency position (similar to spectrum in Figure 4.10). Nevertheless, the emission intensity is expected to be the same when integrated over the spectral range.

In view of image distortion correction, the purpose is to correct for the geo-information deviation and the corresponding phase variation induced by the optical distortion effect. Simulation results indicate that the one-parameter division model can provide the correction accuracy within 1.5 pixels for the largest distortion, the vertical error scales with its square root accordingly. Therefore, the maximal deviation after the image distortion correction based on one parameter division model is about one pixel (0.1 km) for the altitude information. The integrated spectral intensities with and without image distortion correction reveal about 2% deviation.

The phase distortion correction applied in this work mainly aims to correct for the local phase variation of the fringe pattern. Since the on ground calibration was made in the laboratory at room temperature, the real phase of the generated interferogram in orbit varies under different temperature and pressure conditions. The lack of phase correction results in the change of the spectral shape, the spectral information may spread to adjacent frequency bins when the overall phase variation is larger than 2π. Based on the instrument characterization, a total intensity change of about 2% for the integrated spectrum is expected with and without phase distortion correction (Figure 5.11). An alternative approach is to extract the phase information based on the in-orbit measurements if the emission lines can be well separated in spectral domain.

The spatial frequency of the heterodyned fringe pattern generated by the crossed wavefronts has the symmetric property around its Littrow position. The emission lines with the same distance to the Littrow wavenumber will consequently produce the same spatial frequency, which will therefore interfere each other in spectral domain. This effect can be reduced by setting the optical filter passband to one side the Littrow to filter out the mirrored emission lines. The ghost removal technique based on 2D Fourier transform can further reduce this leakage effect for an tilted interferogram. Experimental result (Figure 5.13) shows almost identical spectra (with deviation less than 0.2%) between the original input emission line and the ghost removed signal from a composed interferogram. When the measured emission lines are not located at very low spatial fre-

quency region, the ghosts can be well removed without modifying the real spectral information.

For the AtmoSHINE instrument, the drop of the signal visibility at higher spatial frequencies is mainly associated with the system MTF change, especially on the detector optics, as shown in Section 5.7. This response curve might vary under different temperature and pressure conditions. Due to the limited time for final payload delivery, the instrument calibration experiment was not fully carried out covering all the possible situations. Additional in-orbit calibration procedure is needed when the payload environment, especially the temperature of the spectrometer, does not fit to the laboratory condition.

The saturation effect in the interferogram center area (Figure 5.6) creates additional integer harmonic components in spectral domain, which shows a fluctuation up to 5% on the secondary harmonic. Note that this effect is more evident for the emission line with wavelength below 763 nm. The major emission lines chosen for the temperature retrieval are located between 763.3 nm and 764.3 nm, where the harmonic effect on the calibration matrix is about 2%. In practice, the payload can be tilted slightly downward to use the less saturated rows in the observation. Excluding the conditioned system visibility variation on the temperature and the saturation effect on part of the measured interferograms, the overall visibility variation reveals about 1% deviation when different number of samples (500-700 pixels) are included.

Chapter 6

In orbit verification

The AtmoSHINE instrument was successfully deployed on 22th of December 2018 from the Jiuquan Satellite Launch Center (JSLC) into a sun-synchronous orbit. This chapter mainly shows some preliminary information for this mission and the corresponding first light results. This experiment is deemed as a successful in orbit verification mission for instrument functionality test and data processing. Based on the developed algorithms and the calibration procedures, Level-0 and Level-1 results for a set of measurements are shown accordingly. This mission highlights the ability of the AtmoSHINE instrument to resolve the emission lines inside the O_2A-band, and the potential ability for further temperature measurements and gravity wave detections.

6.1 AtmoSHINE onboard the satellite

6.1.1 Mission introduction

The flight opportunity of the AtmoSHINE instrument was given as a rideshare (secondary) payload onboard a technical verification satellite

(Hongyun project) for the low-orbit broadband communication. The satellite was launched into a sun-synchronous low Earth orbit of about 1067 km altitude. The orbit inclination angle is 99.78° during the designed mission lifetime of at least one year. The satellite platform offers a pointing accuracy of 0.4°, which corresponds to a tangent altitude uncertainty of about 25 km. The stability of the attitude can be controlled at least within $0.01^\circ/s$, which corresponds to about 0.6 km altitude uncertainty in the observation. The knowledge of the satellite attitude is about one order of magnitude better.

As demonstrated in Figure 6.1 for the instrument onboard the satellite platform, installed outside the main chamber, the AtmoSHINE is viewing to the left side with respect to the satellite flight direction, which is the back side of the solar panels. The size of the AtmoSHINE payload is about 400 mm $\times$112 mm $\times$ 141 mm. The instrument was mounted about 30° degree below horizontal direction to view the earth limb, and is dedicated for the night glow observation. In order to operate the detector at low temperature, the detector is cooled separately by a passive radiator unit. A heating pad is attached to the cover of the electronics box, which will be switched on in case the instrument temperature gets colder than the nominal operational condition.

In nominal observation mode, the AtmoSHINE instrument is facing the Earth limb to observe the O_2A-band emission lines at around 90 km at nighttime. The deep-space observation mode allows the detector dark current to be measured in orbit, which requires a satellite roll maneuver of at least 5° so that the instrument line of sight (LOS) is pointed to the deep space. Additional operation opportunities are the nadir observation towards a specified earth surface for the radiometric calibration, and the astronomical target observations (stars, Mars, moon) for the radiometric and LOS calibration. The integration time and region of interest (ROI) shall be adjusted for different observation modes.

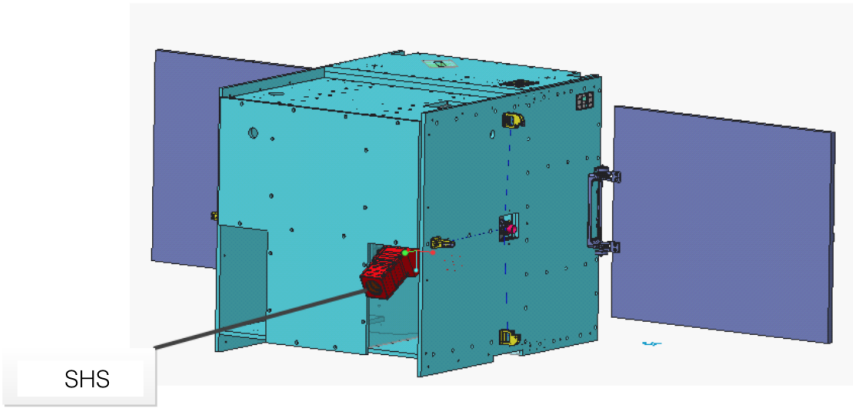

Figure 6.1: Model demonstration of the AtmoSHINE instrument onboard the satellite platform, with an angle of around 30° downward looking to the earth limb. The instrument is placed on the backside of the solar panels.

6.1.2 Satellite launch and the first light

The satellite was launched on 22th of December 2018 at 0:51 CET using the Long March 11 carrier rocket from the JSLC in north-western China (Figure 6.2). The first in orbit test of the AtmoSHINE instrument was carried out on the following days. The actual orbit has a perigee of about 1062 km and a apogee of about 1078 km. The orbit period is about 106.5 minutes. The initial test results revealed that the payload worked nominally within the expectation.

In order to verify the accuracy of the satellite attitude and the instrument observation functionality, the ROI was set to be the maximal and different integration times were tested in the first phase. Figure 6.3 shows the satellite trajectory in a global map with measurements for different integration times. The frame time between each image was set two seconds longer than the integration time for a successful readout routine. In this test, a small amount of data acquired contains unexpected fringe patterns,

Figure 6.2: Launch of the AtmoSHINE instrument onboard the satellite using the Long March 11 carrier rocket on Dec 22, 2018.

which is assumed to be related to the unsynchronization problem during frame communication.

Two representative interferograms obtained during the observations are selected and shown in Figure 6.4 for the O_2A-band nightglow measurements at different geo-locations. The brightest vertical "barber poles" displayed at both image centers correspond to the location of the zero-order interference. Besides the detector dark current effect, the hot pixels shown in Figure 6.4(a) result from high energy particles hitting on the detector as the satellite passed by the south Atlantic anomaly (SAA) region. The localizations of the emission layers in the two interferograms are not exactly identical, which is likely associated with the altitude variation due to the non-ideal spherical shape of the Earth and the inhomogeneity of the atmosphere. An additional object can be seen in Figure 6.4(b) along with its ghost, which is more or less symmetrically reflected over the image center. Notice that the slightly tilt of the interferogram is caused by the

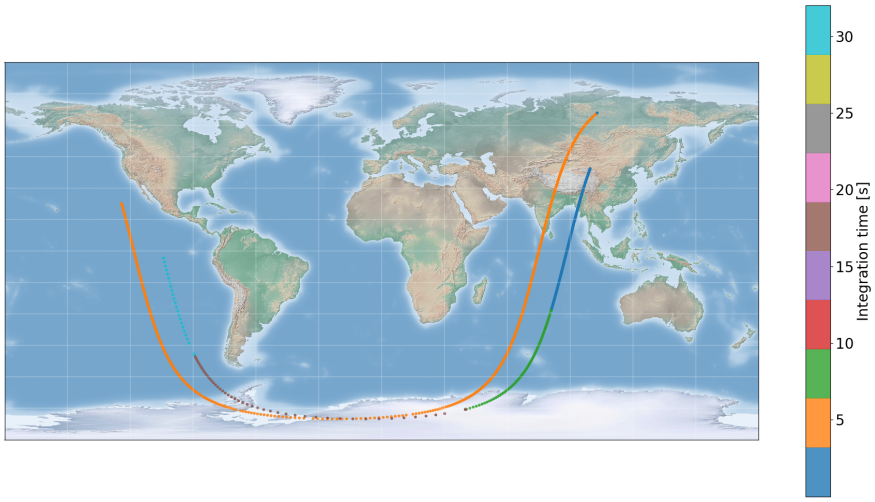

Figure 6.3: Geolocation of the AtmoSHINE first measurements obtained on 23 Dec, 2018. ROI is the full detector size. The first orbit contains measurements with 4s integration time, the second orbit contain measurements with: 1s, 2s, 8s, 16s, 32s.

rotation of the gratings.

6.2 Data analysis

6.2.1 Dark current

The full range of the detector readout in the first phase contains dark regions on the detector boundary, which are not illuminated directly. They are considered to be unaffected by the stray light effect during observations. To study the dark current behavior in orbit, these regions are selected from several frames under different integration time configurations, as shown in Figure 6.5(a) for the histogram. The plot with 32s integration time shows more deviated distribution than other measurements, which is

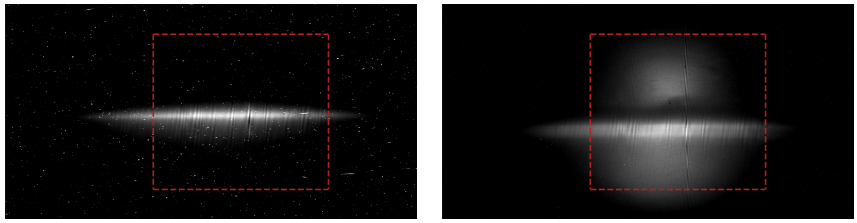

(a) Interferogram without strong stray light

(b) Interferogram with stray light

Figure 6.4: Full frame (1160*1972 pixels) interferograms taken at different geolocations. (a): Interferogram taken at 94.2° W 38.2° S, 32s integration time. (b): Interferogram taken at 13.8° W 80.1° S, 16s integration time. Red dashes lines indicate the selected area (840*840 pixels) for later analysis.

most likely associated with the radiation effect in the SAA region.

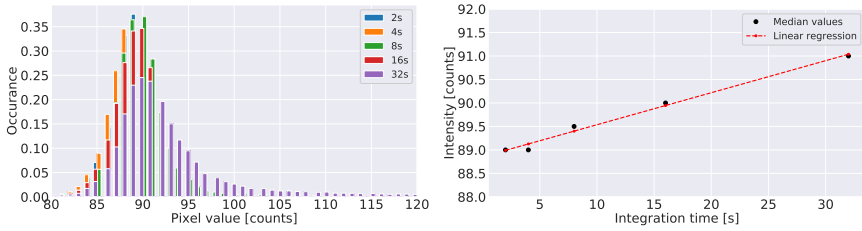

(a) Intensity distribution of shielded pixels

(b) Mean intensity vs integration time

Figure 6.5: (a): Intensity distribution of the dark (shielded) pixels. (b): Signal intensity at different integration times. The median values are used for the representation, which are taken from a set of frames with the same integration time to reduce the radiation effect. Regression analysis shows a gradient of 0.068 count/s and a bias of 88.85 counts.

If the “hot pixels” on the detector are caused by the radiation effect,

their positions are considered to be varying in different measurements. The radiation effect can therefore be suppressed in the dark current characterization by taking the median value from different frames. Figure 6.5(b) displays the dark current profile with respect to different integration times averaged over pixels. A linear regression analysis indicates a gradient (dark current) of 0.068 count/s at $-17°$C measured by the detector internal sensor. This value is considered to be several orders of magnitude lower than the intensity of the emission lines, therefore its noise in spectral domain can be neglected even without correction. The estimated bias shows the averaged detector fixed pattern of about 88.85 counts, which is almost identical to the characterized value on ground.

6.2.2 Radiometric calibration

Unlike a typical grating spectrometer, the radiometric calibration of the SHS instrument can be carried out in spatial domain along with the instrument flatfield correction. For the AtmoSHINE instrument, the ACU built up for the flatfield measurement did not cover the whole FOV. Under this circumstance, the radiometric calibration is implemented based on the calibration matrix derived from the Blackbody measurement (Section 5.1). The zero-order interference patterns from the blackbody measurements are replaced by a series of interpolated points (Figure 6.6). The equivalent photons arriving on the instrument can be estimated via multiplying this calibration matrix after the detector fixed pattern removal.

Figure 6.7(a) shows the performance of implementing the radiometric calibration on the selected areas shown in Figure 6.4(a). The calibration converts the detector digital number to the corresponding photons arriving at the instrument. The inhomogeneity of the recorded limb radiance after correction is significantly improved, especially on two sides of the interferograms. In the limb sounding observation, each row on the detector records the emissions from different layers integrated along the LOS, the lower half of the image is therefore brighter than the upper half (Figure

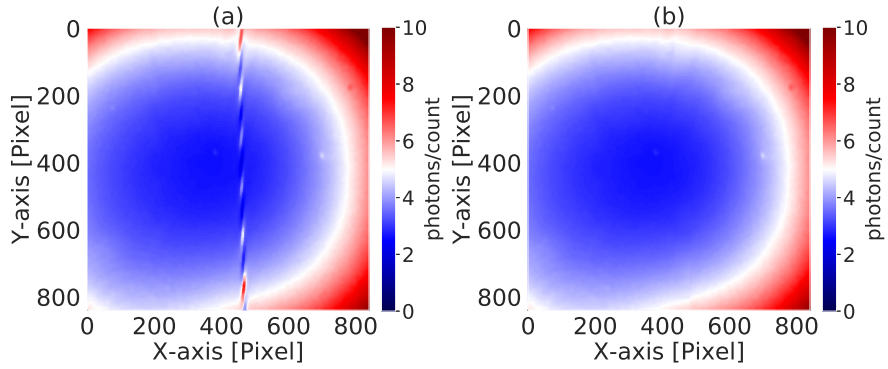

Figure 6.6: (a): Radiometric measurement from the Blackbody emission characterized on ground. (b): Corrected radiometric response matrix, the zero-order interference regions are replaced by a series of interpolated points with polynomial approximation for each row.

4.8).

As displayed in Figure 6.8 for the signals of different rows, the curved intensity distributions become relative stable after the calibration. Besides the measurement uncertainty in the calibration matrix, the gradual incline or decline may indicate an inhomogeneous field of the atmospheric scene. Note that the implementation of the instrument radiometric calibration also flats the corresponding envelope of the fringe pattern (Section 5.8.2), the spectral broadening caused by the non-uniformity of the optical system is accordingly suppressed.

As shown in Figure 6.7(b), an object in the upper half of the image is mirrored to its lower half. This is suspected to be the moon outside the FOV as a source of stray light. A rough estimation based on the geometry indicates that the diameter of the moon imaged on the detector corresponds to about 335 pixels, which fits quite well to the size of this object.

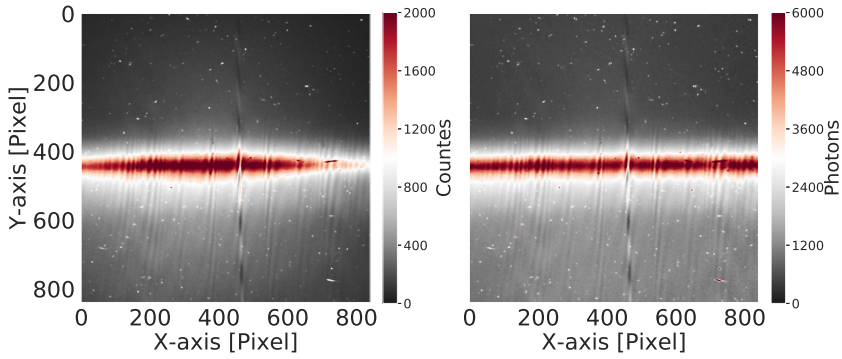

(a) Radiometric calibration for the interferogram in Figure 6.4(a)

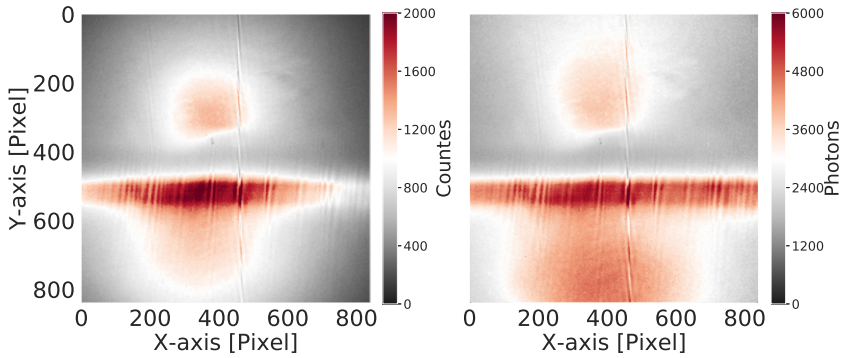

(b) Radiometric calibration for the interferogram in Figure 6.4(b)

Figure 6.7: Radiometric calibration of the interferograms on the selected region in Figure 6.4. Left subplots: interferograms recorded on the detector in counts. Right subplots: interferograms after radiometric calibration in number of photons.

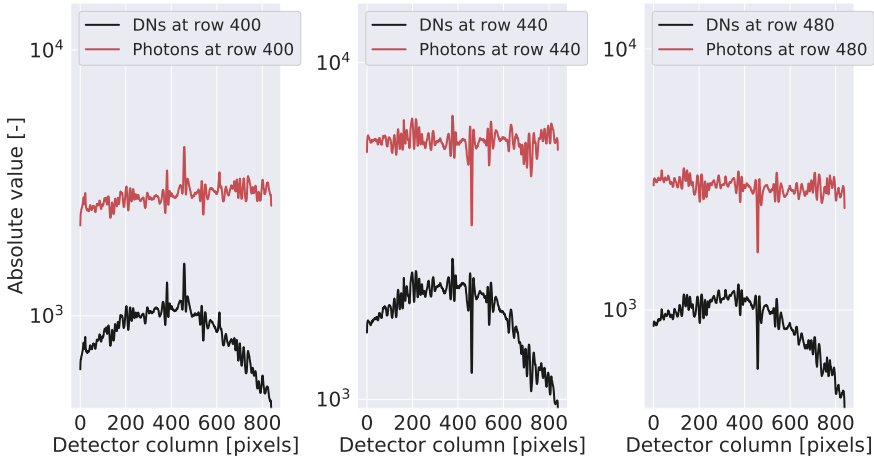

Figure 6.8: Radiometric calibration performance at different rows in Figure 6.4(a). Black curves correspond to the recorded interferogram intensity in counts (DNs), red curves correspond to the estimated photons on the instrument in number of photons. The detector fixed pattern is subtracted before radiometric calibration. For each subplot, 20 rows are binned to improve the SNR.

The lunar phase at the measured time was nearly full (>95 % at 0h33mins, Dec 23, 2018). The radiation from the moon also partly spreads over the O_2A-band emission layer, the counted photons in this region are larger than the unaffected area.

6.2.3 Spectral analysis

The interferograms obtained in space have to go through a series of corrections before they are converted to the calibrated spectrum for scientific analysis. Since the parameters such as the temperature and pressure of the instrument characterized on ground may be different from those in the actual space environment, the verification of the corresponding correction

procedures in orbit is also necessary. This part of the thesis analyzes the impact of these correction techniques on the accuracy of the spectrum obtained in orbit.

In orbit dark current measurements can be obtained via deep space observation by adjusting the attitude of the satellite. So far, the AtmoSHINE instrument has not applied such an observation mode. Nevertheless, through analyzing the in orbit data, the temperature of the detector is usually below $-15°C$. Under this condition, the dark current generated by the detector is much lower than the received photons from the nominal limb radiance. Operating under the manual calibration mode, the correction of the detector effect only requires the subtraction of the detector offset. Afterwards, corrections in spatial domain including the image distortion correction, the phase correction and the ghost removal are implemented before Fourier transform. The filter curve (A.4) and the visibility variation are later calibrated in spectral domain.

Figure 6.9 shows the converted spectra with and without ghost correction based on 2-D Fourier transformation. The uncorrected spectral intensity shows an overall higher intensity than the corrected one, especially in the shorter wavelength region (lower spatial frequency). Due to the filter characteristic, part of the emissions from the other side of Littrow also contributes to the converted spectrum, which results in the deviation of the spectral intensity and the deformation of the spectral shape. In this case, the correction of the ghost lines is essential to retrieve the atmospheric parameters.

Note that the intensities of the emission lines in each pair are partly reversed to some extent at longer wavelengths, which does not occur in the theoretical simulations under normal atmospheric temperatures without considering the real ILS. As characterized on ground (Figure 5.10 in Section 5.4, Appendix A.5), a combination of the image distortion and localized phase distortion enables most of the distortion effect to be corrected. The temperature sensors on the optics reveal that the operational temperature in orbit is more than 40 K lower than the room temperature for calibration. This might result in the change of the overall phase distribution.

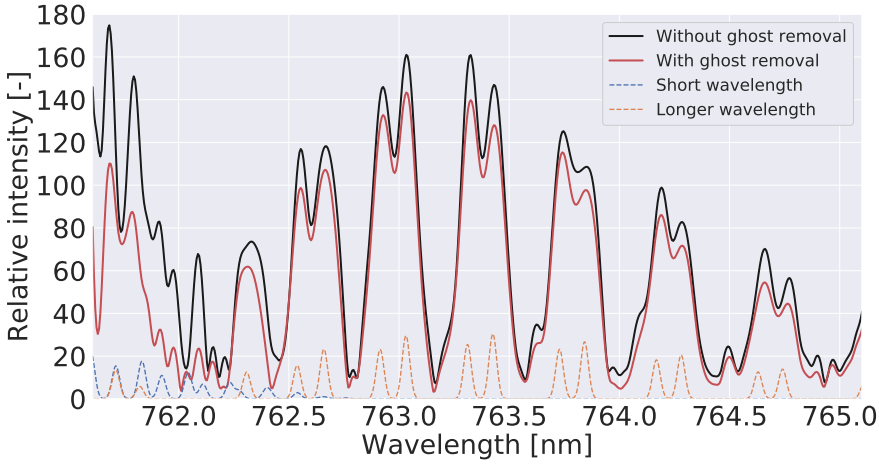

Figure 6.9: Converted spectra from Figure 6.7(a) (after radiometric calibration) with (red) and without (black) ghost removal. 20 rows around the highest emission layer are binned to improve the SNR. The fringe patterns are Hamming apodized and zero padded before FFT. Dashed blue and orange lines represent the simulated O_2A-band emission from shorter and longer wavelength side of the Littrow.

This effect could be further verified with the qualification model (QM) in the lab. To maintain the total energy inside each line pair, adjacent emission lines should be combined in the temperature retrieval. Once the emission lines for real measurements can be well separated one by one in spectral domain, their phase functions can also be characterized and corrected in orbit.

6.2.4 SNR analysis

The estimation of the measurement SNR can be performed individually for each interferogram. In general, the measured noise is mainly caused by the detector dark current noise and the shot noise counting incom-

ing photons. For images that are integrated over relative long time, the readout noise for each pixel can be negligible for the AtmoSHINE instrument. The detector offset is roughly identical in each measurement and does not cause uncertainty in the measurement of the modulated signals. Nevertheless, it should be removed firstly in the SNR evaluation.

The interferogram with 32s integration time shown in Figure 6.7(a) after radiometric calibration is used as a demonstration. The center 700 columns are utilized in the Fourier analysis, where the signal is binned over 20 rows around row 440 (highest emission layer). Subtracting the detector bias, the remaining 5648 photons per pixel correspond to the shot noise of $\sqrt{5648} \approx 75$ photons/pixel. Depending on the number of sampled pixels, the SNR transmission rate from spatial to spectral domain is about $\sqrt{\frac{700}{2}} \approx 18.7$. Accordingly, the noise on each DFT component can be estimated as $\frac{75}{18.7} \approx 4$ photons/pixel. The equivalent noise bandwidth (ENBW) of applying the Hamming apodization decreases the SNR to a factor of 1.36 (Table 4.1), which leads to an equivalent noise of about 5.44 photons/pixel.

Considering 13 emission lines with wavelength between 762.2 nm and 765.0 nm (Figure 6.9), the integrated intensity is about 2221 photons. The averaged emission intensity for each line is around 170 counts. The corresponding SNR can be estimated as $\frac{170}{5.44} \approx 31.4$ without binning. When 20 rows are binned, the SNR becomes $31.4 \times \sqrt{20} \approx 140$. The equivalent SNR in spatial domain is about $\frac{139.7}{18.7} \approx 7.5$ with 20 rows binning. This fits roughly to the simulated scenario with 32s integration at lower detector temperature, as shown in Figure 5.18.

In a shot noise limited system, doubling the integration time in principle increases the SNR by a factor of $\sqrt{2}$. Longer integration time generally requires higher stability of the satellite attitude system and it also means a decrease in the spatial resolution. Therefore, a trade-off between the SNR of the measured signal and the spatial resolution of the image has to be made in practice. For an ideal O_2A-band night glow observation with 20 rows in each altitude bin, an amplitude error between 1% and 2%

in spectral domain corresponds to the integration time of around 10s to 20s.

6.2.5 Limb radiance intercomparison

In this part, the limb radiance measurements obtained by the AtmoSHINE instrument in the first test phase are compared with the data from the SCIAMACHY instrument, which also measured the O_2A-band emissions until 2012. Since the SCIAMACHY measurements are not available for mesospheric night glow in the southern hemisphere on December over years, an alternative profile is displayed for the averaged radiance at 32.5° S over different longitudes in September, 2005.

Two AtmoSHINE measurement examples are taken from Figure 6.7 after radiometric calibration. Ghosts from other side of Littrow are corrected before applying FFT. The measured spectra between 762 nm and 765 nm (13 emission lines together) are integrated for each row. Simulation results (as demonstrated in Figure 1.2) show that the emission lines between 762 nm and 765 nm account for about 51% of the entire O_2A-band emissions. This factor is used to scale the AtmoSHINE measurement to the whole O_2A-band emissions. For AtmoSHINE measurments the peak emission rows on the detector are in aligned with altitude 90 km in this demonstration.

As shown in Figure 6.10, the vertical profiles derived from two instruments are quite similar, and the corresponding limb radiance stays within the same order of magnitude. The measurements for altitude over 100 km near the south polar region exhibit an additional offset, which might be associated with the stray light that has a continuous spectrum, as suspected to be the moon effect in Figure 6.7(b). Note that the amount of limb radiance estimated also depends on the utilized instrument spectral response function (optical filter and visibility), since only the modulated part of the emissions will be counted in the measured spectrum.

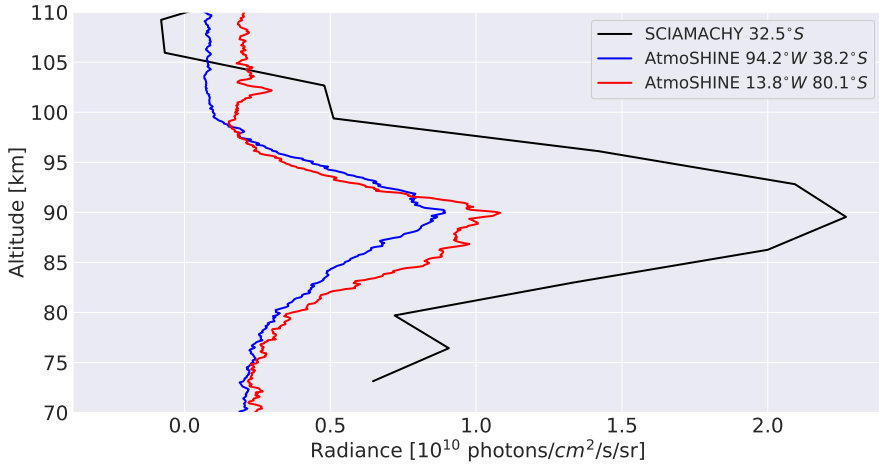

Figure 6.10: Limb radiance of the estimated O_2A-band emissions at different altitudes. The AtmoSHINE measurements are taken at different longitudes/altitudes, the peak emission rows on the detector are in aligned with altitude 90 km in the demonstration. The profile from SCIAMACHY measurement is represented by the mean value at 37.5° S, averaged over different longitudes in September, 2005.

6.2.6 Temperature retrieval

Under the local thermal equilibrium condition, the rotational temperature of the emission layer approximately equals to its kinetic temperature. The intensity of each emission line in the vibration-rotation spectrum follows the temperature-dependent Boltzmann distribution (*Song et al.*, 2017):

$$\eta_{rot} = \eta \frac{g'}{Q(T)} A_i \exp\left(\frac{-hcE'}{kT}\right) \tag{6.1}$$

with h the Planck constant, c the speed of light and k the Boltzmann constant. E' and g' correspond to the upper state energy and degeneracy, respectively. A_i is the Einstein coefficient of the transition, $Q(T)$ is the rotational partition function and η is the total number density. Utilizing

the paramters derived from the HITRAN database (*Gordon et al.*, 2017), the O_2A-band spectrum can be generated at different temperatures via simulation (Figure 1.2).

The retrieval of the rotational temperature can be categorized into two classes: the direct calculation and the spectral fitting methods. Based on the former approach, the temperature can be directly calculated based on the relative intensity of the emission lines. This method is suitable when each line can be well distinguished, and the spectral resolution of the instrument is relatively high. Considering the line shape of the instrument and other broadening effects, using the spectral fitting method to retrieve the rotational temperature is commonly more preferred in practice.

This section mainly focuses on the preliminary temperature retrieval results and their accuracy associated with the effect of the relevant instrument characteristics. In order to improve the SNR in this process, the upper and lower ten lines of the strongest radiation row on the detector are binned, which corresponds to about 2 km altitude bin. Note that this process does not include a forward model for the line path integral, so the converted spectrum represents a superposition of the spectra at several heights.

For a preliminary comparison, a model is used to generate the temperature dependent Boltzmann distribution of the O_2A-band. In this process, the ILS in spectral domain is considered as Gaussian-like. Figure 6.11 shows the measured spectrum along with the simulated spectra at different temperatures. The processor in spatial domain contains most of calibration and correction steps shown previously, e.g. the detector offset removal, radiometric calibration, interferogram and phase distortion correction and ghost removal. In spectral domain, the spectral response functions including the visibility function and the filter characteristic are corrected based on the measurement on ground. The wavelength is recalibrated according to the measurements in space.

As discussed in Section 6.2.3, the measured spectrum exhibits a redistribution of energy from two separate lines in one pair. As a fair compar-

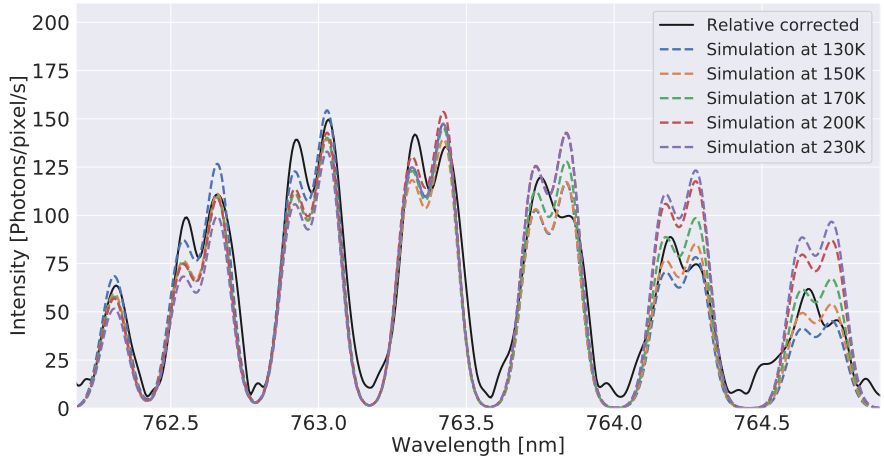

Figure 6.11: Measured spectrum from Figure 6.4(a) and simulated spectra at different temperatures. The spectra from the simulation are scaled approximately to the mean intensity of the measured spectral pair between 763.2 nm and 763.6 nm. The upper and lower ten lines of the strongest emission row (row 480 in 840 rows) on the detector are binned.

ison, the simulated spectra are scaled approximately to the mean intensity of the measured spectrum between 763.2 nm and 763.6 nm in the filter center region. The simulated spectra with higher temperatures display larger amount of photons at longer wavelength region, their partitions at shorter wavelength are relatively small. Intuitively, the measured spectrum corresponds to a lower atmospheric temperature.

Besides optimizing the temperature parameter, a scaling factor should also be included in the optimization procedure to achieve the optimal result. As the ILS may not be perfectly represented by an ideal Gaussian line shape, the broadening factor for each emission line is set as a fixed value to avoid overfitting. To reduce the influence of the filter response curve on both sides of the roll-off (edge) area on the measurement uncertainty, the emission lines within the relative flat area of the filter curve are selected: 5 line pairs between 762.5 nm and 764.5 nm. The simulated spectra are

generated with the same wavelength axis as that in the converted spectrum from real measurements. The expected emission spectrum in each iteration is generated utilizing the forward model. The 2-norm of the residual between the generated spectrum and the real measured one are defined as the objective function.

As shown in Figure 6.12, the optimization on each spectral point results in a temperature value of about 140 K. Due to the spectral leakage effect and the imperfect ILS, the spectral components are spread outside the Gaussian-like region as the side lobe effect. These components can hardly be captured by the spectral fitting method with an ideal ILS. To reduce the impact of the irregular ILS, the sum of each integrated spectral interval is used as the objective function. This optimization delivers relative higher temperature values (145 K). In addition, accurate estimation also requires the removal of the spectral offset, e,g, the background and the stray light effect.

Figure 6.13 displays a study on the relationship between the retrieved temperature values and the number of pixels included in the Fourier analysis. The relative difference of about 7K in the obtained temperatures utilizing the spectral and integral methods does not change significantly with the sampling number. The temperature results obtained from the retrieval are relatively stable as long as no less than 400 samples are included in the processing. For O_2A-band spectrum, only two lines inside one pair share similar temperature dependency, the intensity distribution differs remarkably between each line pair at different temperatures. Stemmed from the limited spectral resolution for limited number of samples, the retrieved temperatures become higher than the normal level due to the interference between adjacent line pairs. Therefore, accurate temperature retrieval requires at least different pairs of the emission lines to be separated in spectral domain.

For the current in-orbit measurements, the uncertainty of the retrieved absolute temperature may be mainly related to the utilized spectral response curve for the calibration. Due to the limited time for on-ground characterization, the calibration could not cover all possible conditions in

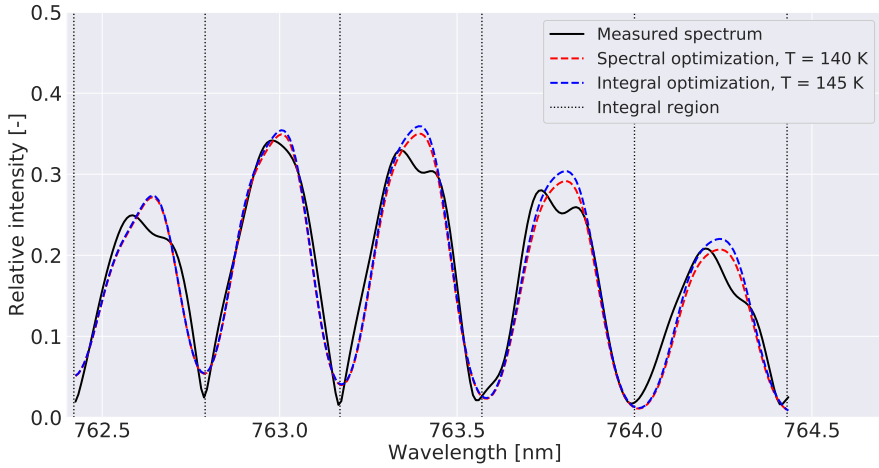

Figure 6.12: Spectra reconstructed with the optimized parameters including the scaling factor. The red dashed curve shows the spectrum retrieved based on the residual for each spectral point. The blue dashed curve uses the sum of each spectral interval as the objective function, the boundaries are marked with the black dashed dots. 400 pixels are used for the Fourier transform with Hamming apodization function.

space, especially for the instrument visibility and the filter characteristics. Depending on the real orbit environment, the spectral response curve may exhibit different behavior from that characterized in the laboratory. In this regard, an alternative in orbit verification of the instrument spectral characteristics needs to be implemented by the cross-calibration with the temperature products from other satellite data covering the same area.

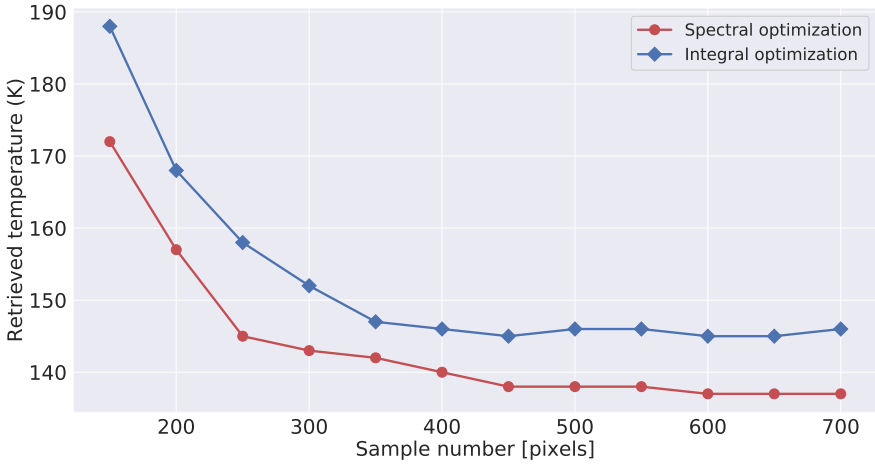

Figure 6.13: Temperature retrieval results with different number of samples for the Fourier analysis. The sampled pixels are picked around the image center.

Chapter 7

Summary and outlook

7.1 Summary

The AtmoSHINE instrument is a miniaturized satellite payload based on the spatial heterodyne spectroscopy for atmospheric temperature measurements in the MLT region. The throughput for a field-widened spatial heterodyne spectrometer is typically more than 2 orders of magnitude larger than for typical grating spectrometers of the same size. This allows the interferogram to be measured with shorter integration time. The vertical temperature profile can be derived from the spectrally resolved O_2A-band emission in a single 2D image according to their temperature dependent intensity distribution.

Characterization of a commercial COTS CMOS detector dark current, readout noise, gain and offset shows that the detector parameters meet the product specifications provided by the manufacturer. The detector chip has been qualified as part of this thesis by laboratory measurements up to a radiation of 85 krads. This fulfills the requirement of a three to five years low earth orbit mission. A blackbody and a specified calibration unit were utilized under laboratory conditions for the study of several instrument characteristics such as the radiometric performance, the instrument

flatfield, the instrument line shape, the image and phase distortion and the modulation efficiency function.

A data processing framework is developed for the AtmoSHINE data products up to Level-1B. The level-0A processing chain mainly includes the spatial correction procedures sequentially applied on the measured interferograms. This processor includes newly developed algorithms for the interferogram distortion correction (*Liu et al.*, 2019) and ghost removal, which have been verified to correct for the corresponding artifacts of the instrument effectively. The emission spectrum after Level-1A processing (spectral response correction and wavelength calibration) allows the temperature information to be retrieved from its relative intensity distribution.

The AtmoSHINE instrument was successfully deployed into orbit on 22th December, 2018. Data from the first in orbit test phase indicates that the instrument worked nominally. The detector reveals similar performance as characterized on ground, whereas the the radiation effect within the south Atlantic anomaly region is quite remarkable. Applying the corresponding algorithms for the data processing, the emission lines of interested in the O_2A-band spectrum can be resolved. Due to the tight schedule, the instrument was not calibrated for the environmental conditions of the first measurement phase. Therefore, discrepencies seen between the in-orbit measurements and the ground measurements are difficult to assess quantatively. A preliminary temperature retrieval using these measurements gave typical mesospheric values of that quantity. Since not all instrument parameters could have been verified so far, the retrieval of the atmospheric temperature can be carried out based on in orbit calibration with other satellite data. As a precursor of future satellite payloads, the AtmoSHINE instrument is deemed as a successful in orbit verification of this technique and provides valuable measurements for further analysis.

7.2 Outlook

The measured data and the developed algorithms have shown potential scientific applications, which are applicable for real SHS measurements from space. Further work is to automate the processing chain considering the needs for different observational scenarios and real-time computation. Beside the standard measurements, dedicated calibration measurements are expected to be implemented, such as the deep-space observation and the astronomical target observation, to further characterize the instrument dark current, line of sight and radiometric performance in orbit.

Based on the experience gained from this mission, the next generation of this instrument may be improved in some aspects. The internal and external stray light effect should be further verified and improved in the further design. The optical distortion of the system should be reduced so that the instrument line shape does not exhibits a strong side lobe effect. Laboratory characterization of the instrument should cover as much as possible the in-orbit conditions, especially for the characterization of the temperature dependent visibility function and filter curve.

The launch of the AtmoSHINE payload marks the start of the development of an improved six-unit (6U) CubeSat, the AtmoCube A1 (*Olschewski et al.*, 2019). In this concept, an albedo cloud camera will be included to detect the stray light reflected from lower atmospheric clouds. The agility of the CubeSat enables the measurement on specific regions from different viewing angles. The 3-D atmospheric volume and the gravity wave structures can be characterized based on horizontally sweeping the instrument LOS from different angles (*Song et al.*, 2018). This finally leads to a CubeSat constellation concept for further observations.

Appendix A

A.1 Amplitude estimation

A signal composed of several sinus functions with different phase shift parameter can be written as:

$$\mathbf{I}(x) = \sum_{i=1}^{K} \mathbf{A}(i) \cos(\omega_i \mathbf{x} + \varphi_i) \tag{A.1}$$

where $\omega_i = 2\pi f_i$ represents the frequency of the signal, the relationship can also be written as a sum of sinus and cosinus function for each frequency component:

$$\mathbf{I}(x) = \sum_{i=1}^{K} (\mathbf{A_c}(i) \cos(\omega_i \mathbf{x}) + \mathbf{A_s}(i) \cos(\omega_i \mathbf{x})) \tag{A.2}$$

where the original amplitude and phase can be recovered by two components as:

$$\mathbf{A}(i) = \sqrt{\mathbf{A_c}^2(i) + \mathbf{A_s}^2(i)}, \qquad \varphi_i = \tan^{-1}\left(\frac{\mathbf{A_s}(i)}{\mathbf{A_c}(i)}\right) \tag{A.3}$$

Considering a measurement sequence on the detector:

$$\mathbf{I} = [I(0), I(1), \ldots, I(N-1)]^T \in R^{N \times 1} \tag{A.4}$$

each measurement can be divided into a combination of sinus and cosinus function:

$$\mathbf{I}(\mathbf{x}) = \sum_{\mathbf{k=1}}^{\mathbf{K}} \mathbf{A_c V_c} + \mathbf{A_s V_s} \tag{A.5}$$

where $\mathbf{V_c}$ and $\mathbf{V_s}$ are vectors representing a combination of cosine and sine functions, separately. The parameter matrix $\mathbf{H} \in R^{N \times 2K}$ can be represented as:

$$\mathbf{H} = \begin{bmatrix} \cos_1(0\omega_i) & \sin_1(0\omega_i) & \cos_2(0\omega_i) & \sin_2(0\omega_i) & \dots & \dots & \cos_K(0\omega_i) & \sin_K(0\omega_i) \\ \cos_1(1\omega_i) & \sin_1(1\omega_i) & \cos_2(1\omega_i) & \sin_2(1\omega_i) & \dots & \dots & \cos_K(1\omega_i) & \sin_K(1\omega_i) \\ \dots & \dots & \dots & \dots & \dots & \dots & \dots & \dots \\ \cos_1((N-1)\omega_i) & \sin_1((N-1)\omega_i) & \cos_2((N-1)\omega_i) & \sin_2((N-1)\omega_i) & \dots & \dots & \cos_K((N-1)\omega_i) & \sin_K((N-1)\omega_i) \end{bmatrix} \tag{A.6}$$

Therefore, the measurement can be expressed in matrix form as $\mathbf{I} = \mathbf{HA}$ where $\mathbf{A} = [A_{c1}, A_{s1}, A_{c2}, A_{s2}, \dots, A_{cN}, A_{sN}]^T \in R^{2K \times 1}$. The amplitude vector can be estimated from the parameter matrix $\mathbf{H}$ and measurements $\mathbf{I}$ by the least square :

$$\mathbf{A} = \left(\mathbf{H}^T \mathbf{H}\right)^{-1} \mathbf{H}^T \mathbf{I} \tag{A.7}$$

accordingly, the amplitude and phase for each component can be recovered. Notice that this estimation is equivalent to the Maximum Likelihood Estimation (MLE) when the noise is AWGN.

A.2 O2A-band emission lines inside the filter range

This appendix shows several O2A-band emission lines inside the AtmoSHINE filter range between 762 nm and 765 nm. The corresponding spatial frequencies on the grating and on the detector are estimated based on the characterization results on ground, as indicated in Section 5.6.

Table A.1: O2A-band emission lines inside the AtmoSHINE filter range

Wavelength	Wavenumber	Spatial frequency (grating)	Spatial frequency (detector)
nm	cm^{-1}	fringes/cm	fringes/cm
762.31	13118.04	28.69	49.47
762.54	13114.10	36.79	63.44
762.66	13112.02	41.07	70.81
762.91	13107.63	50.09	86.37
763.03	13105.62	54.23	93.50
763.31	13100.82	64.09	110.51
763.43	13098.85	68.14	117.49
763.73	13093.66	78.81	135.89
763.84	13091.71	82.82	142.80
764.17	13086.13	94.29	162.57
764.28	13084.20	98.26	169.42
764.63	13078.22	110.55	190.61
764.74	13076.32	114.46	197.34

A.3 Global coverage

The satellite data received in the first test phase covers a latitude range from 80° S to 60° N with 4s integration time. Figure A.1 shows layer-wise intensity variation in the received detector counts at different altitudes and latitudes. Each analyzed interferogram contains 840*840 pixels, the intensity of each row is shown for the averaged value over columns. In this comparison, the ghost removal technique is implemented to separate the emissions from two sides of Littrow. Figure A.1 (b) represents the measured emissions between 762.2 nm and 765.0 nm. Figure A.1 (c) contains the modulated emission lines that are smaller than the Littrow wavelength.

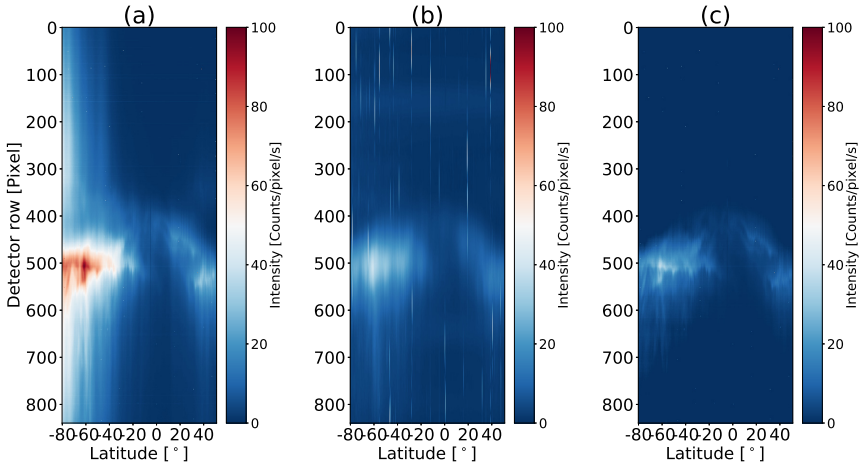

Figure A.1: Row-wise emission intensity measured at different satellite latitudes. The detector offsets are removed. Negative/positive latitude values correspond to the south/north hemisphere. Detector row 0 represents the upper altitude region, row 800 represents the lower altitude region. (a): Total emission intensity. (b): Emissions between 762.2 nm and 765.0 nm. (c): Emissions from other side of the Littrow wavelength (<761.2 nm).

Figure A.1 (a) shows quite strong global inhomogeneity, especially in the

south polar region. According to the orbit simulation result, although the tangent point was not illuminated by the sun light, the sun light covered part of the instrument LOS. Other possible reasons are the reflected moon light from the sun, or the aurora effect in the polar region that generate more O_2A-band emissions. Taking the Fourier transform on the row 250 in Figure A.1 (a), the corresponding spectrum (Figure A.2) do not show prominent O_2A-band spectral characteristics. Its spectrum can be considered as the background spectrum in the O_2A-band measurements.

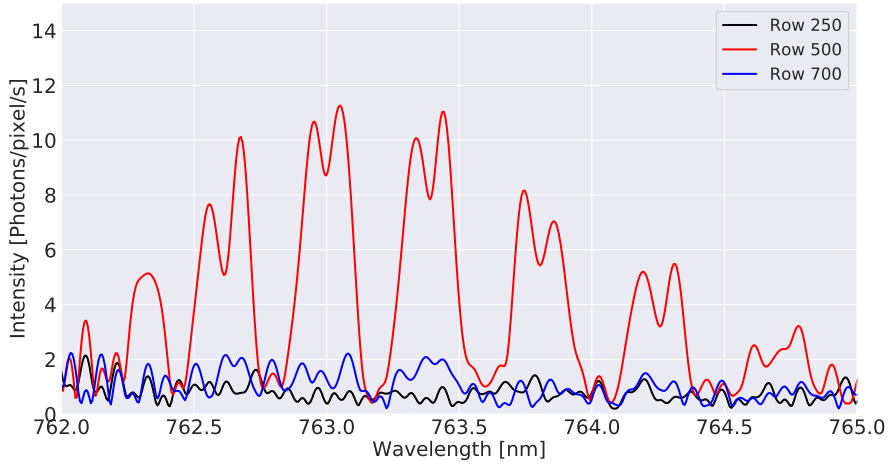

Figure A.2: Converted spectra from Figure 6.7(b) at different rows, 20 rows are binned to improve the SNR. Row 250 corresponds to the row containing stray light out of field. Row 500 represents a strong emission layer in the O_2A-band. Row 700 is taken at the lower image region where the interference pattern still apears in the presence of the stray light effect.

A major constituent of the signal presented in the lower image region (around row 700 in Figure A.1 (a)) may be the stray light (scatting) effect, which mirrors the radiation that should have been presented in the upper part of the interferogram. This effect might be the ice particles of the polar mesospheric clouds (PMCs) in the polar summer mesosphere region as the scattering effect (*Pérot et al.*, 2010). This is considered to be a kind of stray light effect outside the instrument and has to be verified with more measurements in orbit. Row 700

in Figure A.2 only contains a small portion of O_2A-band emission lines. It is speculated that most of the O_2A-band emissions from lower layers are blocked or scattered by the PMCs.

Since the satellite is operating approximately in a circular orbit, the variation in the tangent point altitude is mainly associated with the Earth radius at different locations. The faint emission layers around the equator shown in Figure A.1 (c) stay at around row 400, whereas the center emission layers in polar regions locates at around row 600. This difference corresponds to a tangent altitude change of about 20 km. As the Earth equatorial radius is around 22km longer than its polar radius, the O_2A-band emission layers recorded on the detector is expected to be lower at polar regions. A satellite orbit simulation shows that the tangent point variation is about 20 km under this orbit condition, which fits to this emission layer variation on the detector at different rows.

A.4 Filter characterization

The response function of the optical filter integrated inside the AtmoSHINE instrument was characterized based on the ACU calibration setup (Figure 5.3). In the experiment, the output power of the tunable laser was monitored by connecting the other end of the optical fiber splitter to a power meter. For each tested wavelength, the energy of the tunable laser was manually adjusted to be identical. Figure A.3 shows the relative response of the filter functions in the region of interest.

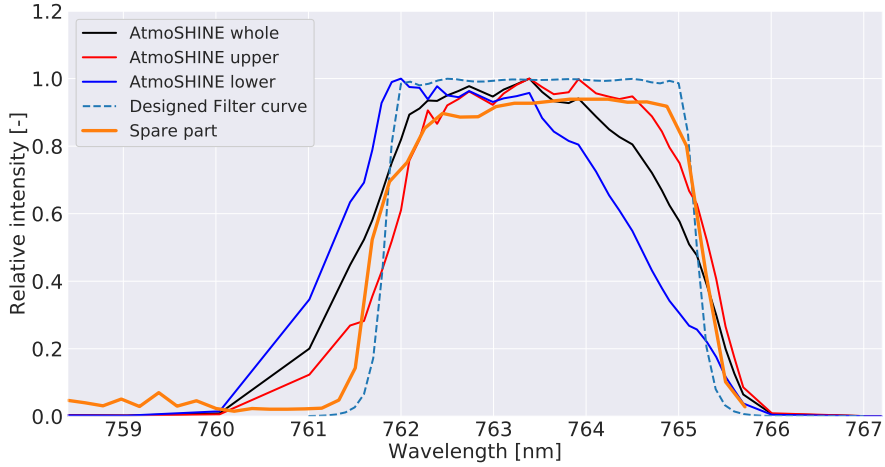

Figure A.3: Filter response functions characterized using different regions of the interferograms for AtmoSHINE instrument. Response curve marked with "AtmoSHINE whole" uses 840 $\times$ 840 pixels in the interferogram center region. "AtmoSHINE upper"and"AtmoSHINE lower" takes 100 $\times$ 100 pixels with the same readout column in "AtmoSHINE whole" while starting from row 200 and row 600, respectively. The curve labeled with "spare part" shows the response curve of another filter sample manufactured in the same batch process. A theory curve provided by the manufacturer is also plotted in the dashed curve.

The filter curve obtained from the overall interferogram, or from the lower

region of the interferogram, indicates a shift to shorter wavelength region. Conversely, the filter center wavelength obtained from the upper part of the image is closer to the theoretical calculation. It is speculated that this effect is associated with the incident angle to the instrument after the ACU due to misalignment in the calibration setup. Later experiments (made after the delivery of the AtmoSHINE instrument) also indicate that when the incident angle has a deviation of more than 5 degrees, the corresponding blue shift is quite remarkable.

Another optical filter sample, manufactured in the same batch process, is utilized for further verification. Since this filter can be tested independently from the integrated instrument, the corresponding filter function can be characterized by illuminating the detector in the presence or absence of the filter. Compared with the theoretically simulated curve, the one measured on ground reveals a slight decrease in the flat-top short-wave region. In addition, the reception of the radiation to the left of the cutoff wavelength (<760 nm) is also evident. This leakage effect agrees with the spectrum components in the measurements in orbit without ghost correction (Figure 6.9). Subsequent data analysis shows that using the filter curve obtained from the characterized "spare part" can deliver more reasonable atmospheric temperature information.

A.5 Composed spectrum with ACU

In this section, several interferograms generated using the ACU setup are superposed to produce the spectrum containing multiple signals. For each interferogram, 700 pixels in the center area is chosen, the Hanning, Hamming and Blackman apodization functions are evaluated. The image distortion and phase distortion are implemented before spectral analysis.

Figure A.4 shows the converted spectra (row 420) from Hanning windowed interferogram when different correction procedures are applied. Similar plots for Hamming apodization function and Blackman apodization function are shown in Figure A.5 and Figure A.6. When the emission lines are closely located within the FWHM of each spectral line, the interference between the emission lines lead to the redistribution of the spectral intensities. A small left side lobe can be seen in the spectra without any correction. This side lobe effects are almost removed for the measured wavelength up to 764.7 nm after applying both correction techniques.

The composed spectra are then fitted based on a mixed model containing multiple Gaussian profiles. As shown in Figure A.7, each spectral component can be distinguished from the multiple emission spectrum. The mean amplitude estimation is about 3% for the dense located spectrum in Figure A.7(a), and about 1.5% for the sparse located spectrum (Figure A.7(b)). The amplitude deviation for single fitted spectrum (Figure A.7(c)) is about 0.9%.

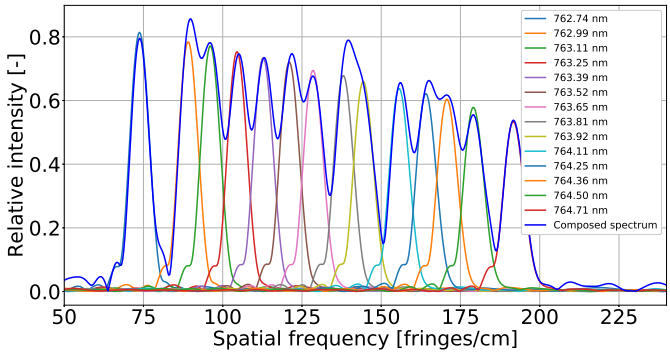

(a) Hanning, without corrections

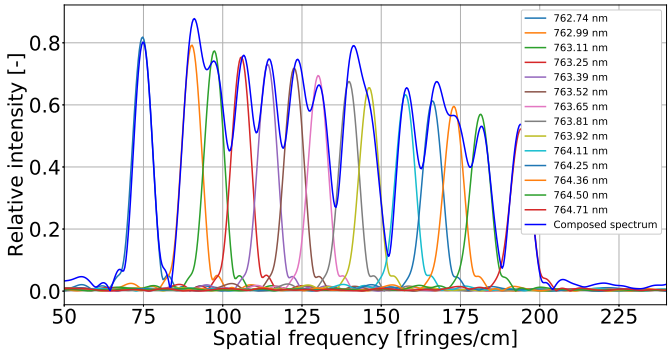

(b) Hanning, image distortion correction

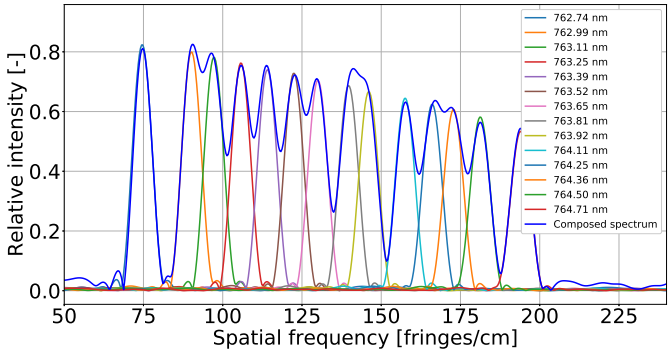

(c) Hanning, image and phase distortion correction

Figure A.4: Composed spectrum with Hanning apodization function, in comparison with individual emission line.

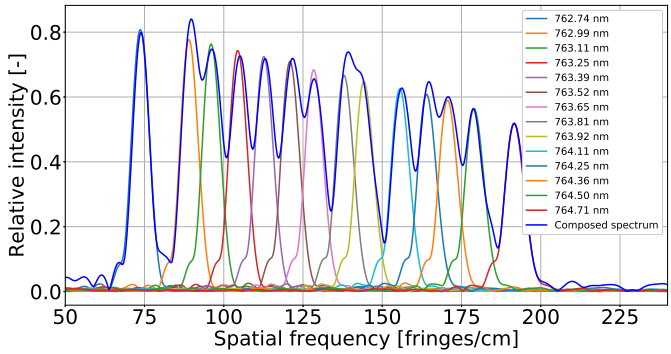

(a) Hamming, without corrections

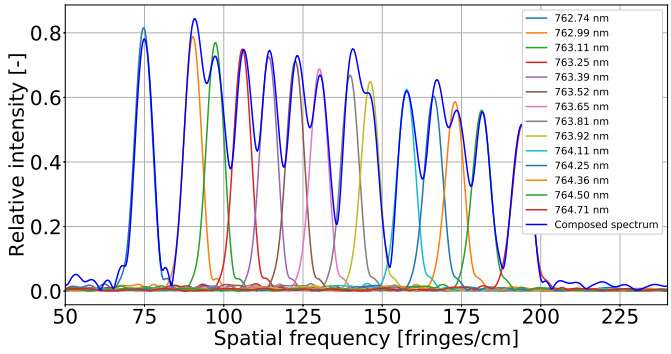

(b) Hamming, image distortion correction

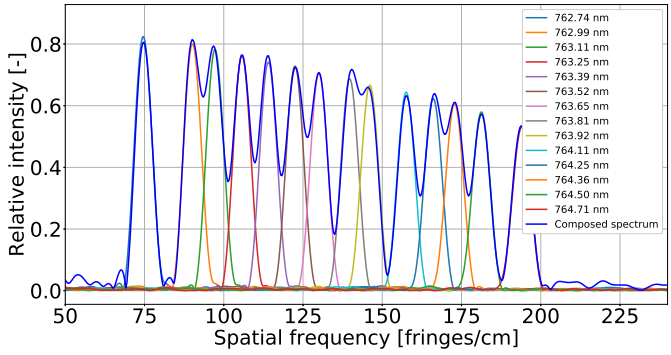

(c) Hamming, image and phase distortion correction

Figure A.5: Composed spectrum with Hamming apodization function.

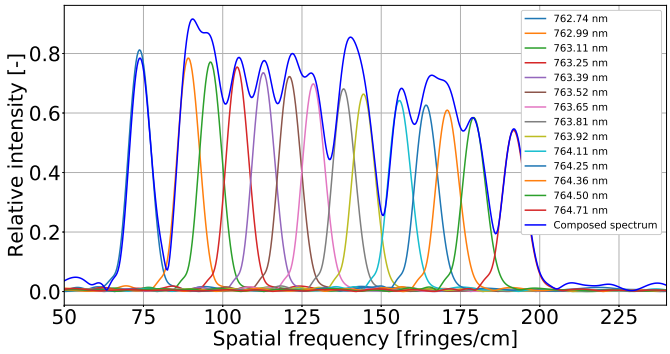

(a) Blackman, without corrections

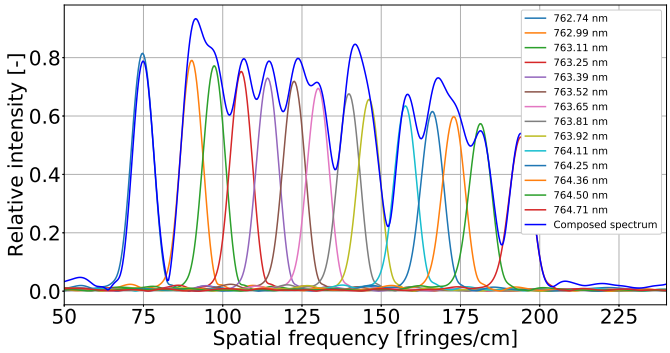

(b) Blackmann, image distortion correction

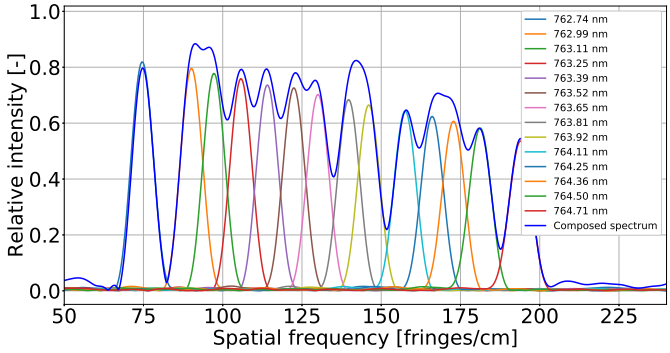

(c) Blackmann, image and phase distortion correction

Figure A.6: Composed spectrum with Blackman apodization function.

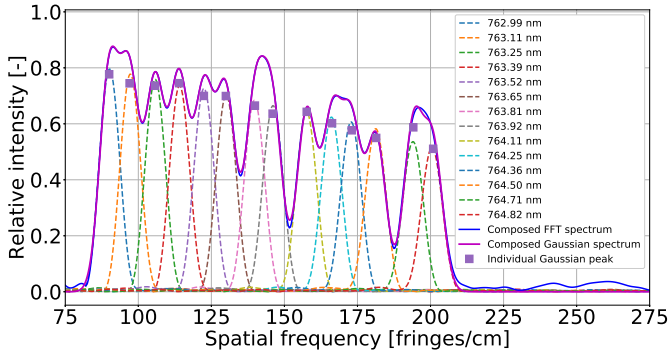

(a) Gaussian fitted spectrum with dense components

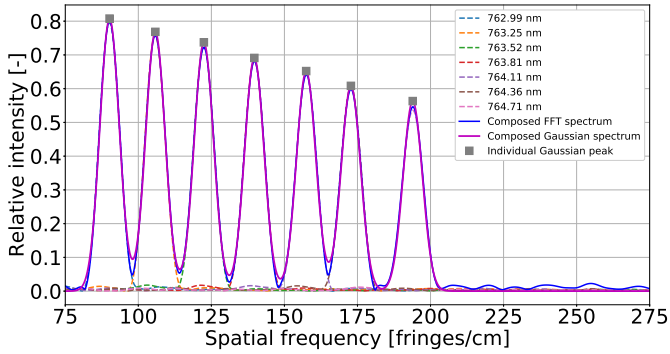

(b) Gaussian fitted spectrum with sparse components

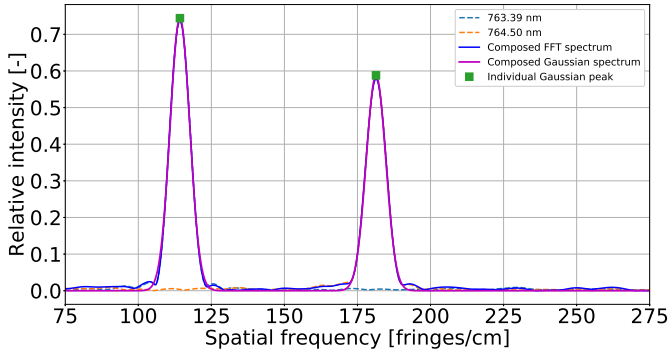

(c) Gaussian fitted spectrum with two components

Figure A.7: Composed spectrum with Hanning apodization function. The Gaussian parameters are derived from each element in the fitted spectrum. (a) Composed dense spectrum. (b) Composed sparse spectrum

Acknowledgements

First and foremost, I wish to express my deep and sincere gratitude towards my supervisor Prof. Martin Riese for bringing me into this topic and providing me the continuous support of my Ph.D project and related researches at IEK-7, FZJ. A similar gratitude belongs to Prof. Ralf Koppmann, who has provided invaluable guidance throughout the study at the BUW. It was a great privilege and honor to study and work under their guidance. I am extending my sincere thanks to Prof. Francesco Knechtli and Prof. Andreas Frommer for their suggestions on the thesis and being members on my graduate committee.

I would like to express my special thanks to my academic supervisor, Dr. Martin Kaufmann, who gave me constant support on research, career and daily life during my Ph.D study. I could never find the entrance into this interesting and meaningful topic without him. My thanks also goes to Friedhelm Olschewski and Peter Knieling for sharing their expertise and providing precious advice and discussion on the instrument, teaching volumes of knowledge and techniques during series of experiments.

Many thanks to my ZEA-2 colleagues, Dr. Heinz Rongen, Tom Neubert, Dennis Froehlich and Georg Schardt, for their support on the electronic components and experiments at ZEA-2. I thank Dr. Christian Monte for providing the chance to make the experiment at the National Metrology Institute of Germany (PTB). I would also like to thank Dr. Klaus Mantel in the Max-Planck-Institute for the Science of light for his suggestions on the optics.

It is my honor to work with all my colleagues at IEK-7 and the University of Wuppertal who have supported me to complete the research work directly or indirectly. Especially, I would like to thank my colleagues in our research group:

Qiuyu Chen, Dr. Michael Deiml, Qiucheng Gong, Dr. Rui Song, Daikang Wei, Oliver Wroblowski, and Dr. Yajun Zhu. They are great teammates and friends during my Ph.D study.

Finally and most importantly, I am extremely grateful to my parents for their loving considerations and great confidence in me all through these years. They tried their best to support and encourage me to do what I want. Without their constant help, I would never have had a chance to accomplish my study in Germany.

Bibliography

Abe, M., and J. O. Smith III (2004), Design criteria for the quadratically interpolated FFT method (i): Bias due to interpolation.

Alemn-Flores, M., L. Alvarez, L. Gomez, and D. Santana-Cedres (2013), Wide-angle lens distortion correction using division models, in *Iberoamerican Congress on Pattern Recognition*, pp. 415–422, Springer.

Barabell, A. (1983), Improving the resolution performance of eigenstructure-based direction-finding algorithms, in *Acoustics, Speech, and Signal Processing, IEEE International Conference on ICASSP'83.*, vol. 8, pp. 336–339, Citeseer.

Barth, C. A. (1966), Rocket measurement of nitric oxide in the upper atmosphere, *Planetary and Space Science*, *14*(7), 623–630.

Becker, S. C., and V. M. Bove Jr (1995), Semiautomatic 3D-model extraction from uncalibrated 2D-camera views, in *IS&T/SPIE's Symposium on Electronic Imaging: Science & Technology*, pp. 447–461, International Society for Optics and Photonics.

Beecken, B., and E. Fossum (1996), Determination of the conversion gain and the accuracy of its measurement for detector elements and arrays, *Applied optics*, *35*(19), 3471–3477.

Bovensmann, H., J. Burrows, M. Buchwitz, J. Frerick, S. Noël, V. Rozanov, K. Chance, and A. Goede (1999), SCIAMACHY: Mission objectives and measurement modes, *Journal of the atmospheric sciences*, *56*(2), 127–150.

Brown, D. C. (1966), Decentering distortion of lenses, *Photometric Engineering*, *32*(3), 444–462.

Burg, J. P. (1972), The relationship between maximum entropy spectra and maximum likelihood spectra, *Geophysics*, *37*(2), 375–376.

Calin, T., M. Nicolaidis, and R. Velazco (1996), Upset hardened memory design for submicron cmos technology, *IEEE Transactions on nuclear science*, *43*(6), 2874–2878.

Canny, J. (1986), A computational approach to edge detection, *IEEE Transactions on pattern analysis and machine intelligence*, (6), 679–698.

Cerna, M., and A. F. Harvey (2000), The fundamentals of FFT-based signal analysis and measurement, *National Instruments, Junho*, p. 54.

Connes, P. (1958), Spectromètre interférentiel à sélection par l'amplitude de modulation, *Journal de Physique et le Radium*, *19*(3), 215–222.

Cooke, B. J., B. W. Smith, B. E. Laubscher, P. V. Villeneuve, and S. D. Briles (1999), Analysis and system design framework for infrared spatial heterodyne spectrometers, in *Infrared Imaging Systems: Design, Analysis, Modeling, and Testing X*, vol. 3701, pp. 167–192, International Society for Optics and Photonics.

Damiani, C., P. Drossart, A. Sémery, J.-M. Réess, and J.-P. Maillard (2007), An imaging heterodyne spectrometer for planetary exploration, in *Fourier Transform Spectroscopy*, p. FTuC3, Optical Society of America.

Daniels, M. (2010), Convex optimization in sinusoidal modeling for audio signal processing.

De Villiers, J. P., F. W. Leuschner, and R. Geldenhuys (2008), Centi-pixel accurate real-time inverse distortion correction, in *International Symposium on Optomechatronic Technologies*, pp. 726,611–726,611, International Society for Optics and Photonics.

Debevec, P. E., C. J. Taylor, and J. Malik (1996), Modeling and rendering architecture from photographs: A hybrid geometry-and image-based approach, in

Proceedings of the 23rd annual conference on Computer graphics and interactive techniques, pp. 11–20, ACM.

Derbenwick, G., and B. Gregory (1975), Process optimization of radiation-hardened CMOS integrated circuits, *IEEE Transactions on Nuclear Science*, *22*(6), 2151–2156.

Devernay, F., and O. Faugeras (2001), Straight lines have to be straight, *Machine vision and applications*, *13*(1), 14–24.

Englert, C. R., and J. M. Harlander (2006), Flatfielding in spatial heterodyne spectroscopy, *Applied optics*, *45*(19), 4583–4590.

Englert, C. R., J. M. Harlander, J. G. Cardon, and F. L. Roesler (2004), Correction of phase distortion in spatial heterodyne spectroscopy, *Applied optics*, *43*(36), 6680–6687.

Englert, C. R., J. M. Harlander, J. G. Cardon, and F. L. Roesler (2005), Correction of phase distortion in spatial heterodyne spectroscopy (shs), in *Fourier Transform Spectroscopy*, p. FTuB2, Optical Society of America.

Faccio, F. (2000), COTS for the LHC radiation environmentain: The rules of the game.

Felix, J. A., P. E. Dodd, M. R. Shaneyfelt, J. R. Schwank, and G. L. Hash (2006), Radiation response and variability of advanced commercial foundry technologies, *IEEE transactions on nuclear science*, *53*(6), 3187–3194.

Fitzgibbon, A. W. (2001), Simultaneous linear estimation of multiple view geometry and lens distortion, in *Computer Vision and Pattern Recognition, 2001. CVPR 2001. Proceedings of the 2001 IEEE Computer Society Conference on*, vol. 1, pp. I–125, IEEE.

Gonzalez, R. C., and R. E. Woods (2002), Digital image processing second edition, *Beijing: Publishing House of Electronics Industry*, *455*.

Gordon, I. E., L. S. Rothman, C. Hill, R. V. Kochanov, Y. Tan, P. F. Bernath, M. Birk, V. Boudon, A. Campargue, K. Chance, et al. (2017), The HITRAN2016 molecular spectroscopic database, *Journal of Quantitative Spectroscopy and Radiative Transfer*, *203*, 3–69.

Harlander, J. M., F. L. Roesler, C. R. Englert, J. G. Cardon, R. R. Conway, C. M. Brown, and J. Wimperis (2003), Robust monolithic ultraviolet interferometer for the SHIMMER instrument on STPSat-1, *Applied optics*, *42*(15), 2829–2834.

Harlander, J. M., C. R. Englert, D. D. Babcock, and F. L. Roesler (2010), Design and laboratory tests of a Doppler Asymmetric Spatial Heterodyne (DASH) interferometer for upper atmospheric wind and temperature observations, *Optics Express*, *18*(25), 26,430–26,440.

Harris, F. J. (1978), On the use of windows for harmonic analysis with the discrete fourier transform, *Proceedings of the IEEE*, *66*(1), 51–83.

Heynderickx, D., B. Quaghebeur, E. Speelman, and E. Daly (2000), ESA's space environment information system (spenvis)-a www interface to models of the space environment and its effects, in *38th Aerospace Sciences Meeting and Exhibit*, p. 371.

Hofmann, D., T. Deshler, F. Arnold, and H. Schlager (1990), Balloon observations of nitric acid aerosol formation in the arctic stratosphere: II. aerosol, *Geophysical Research Letters*, *17*(9), 1279–1282.

Holst, G. C., and T. S. Lomheim (2007), *CMOS/CCD sensors and camera systems*.

Jain, V. K., W. L. Collins, and D. C. Davis (1979), High-accuracy analog measurements via interpolated FFT, *IEEE Transactions on Instrumentation and Measurement*, *28*(2), 113–122.

Kalicinsky, C., P. Knieling, R. Koppmann, D. Offermann, W. Steinbrecht, J. Wintel, and J. Laštovicka (2016), Long-term dynamics of OH* temperatures over central europe: trends and solar correlations., *Atmospheric Chemistry & Physics*, *16*(23).

Kaufmann, M., J. Blank, T. Guggenmoser, J. Ungermann, A. Engel, M. Ern, F. Friedl-Vallon, D. Gerber, J.-U. Grooß, G. Günther, et al. (2015), Retrieval of three-dimensional small-scale structures in upper-tropospheric/lower-stratospheric composition as measured by GLORIA, *Atmospheric measurement techniques*, *8*(1), 81–95.

Kaufmann, M., F. Olschewski, K. Mantel, B. Solheim, G. Shepherd, M. Deiml, J. Liu, R. Song, Q. Chen, O. Wroblowski, et al. (2018), A highly miniaturized satellite payload based on a spatial heterodyne spectrometer for atmospheric temperature measurements in the mesosphere and lower thermosphere, *Atmospheric Measurement Techniques*, *11*(7), 3861–3870.

Kokin, G., and E. Lysenko (1994), On temperature trends of the atmosphere from rocket and radiosonde data, *Journal of Atmospheric and Terrestrial Physics*, *56*(9), 1035–1040.

Lacoe, R., J. Osborn, D. Mayer, S. Brown, and D. Hunt (1998), Total-dose radiation tolerance of a commercial 0.35/spl mu/m cmos process, in *Radiation Effects Data Workshop, 1998. IEEE*, pp. 104–110, IEEE.

Lin, Y., G. Shepherd, B. Solheim, M. Shepherd, S. Brown, J. Harlander, and J. Whiteway (2005), Introduction to spatial heterodyne observations of water (SHOW) project and its instrument development, in *Proc. XIV Int. TOVS Study Conf., 25-31 May 2005, Beijing, China*, pp. 835–843.

Liu, J., D. Wei, Y. Zhu, M. Kaufmann, F. Olschewski, K. Mantel, J. Xu, and M. Riese (2018), Effective wind and temperature retrieval from doppler asymmetric spatial heterodyne spectrometer interferograms, *Applied optics*, *57*(30), 8829–8835.

Liu, J., D. Wei, O. Wroblowski, Q. Chen, K. Mantel, F. Olschewski, M. Kaufmann, and M. Riese (2019), Analysis and correction of distortions in a spatial heterodyne spectrometer system, *Applied Optics*, *58*(9), 2190–2197.

Luenberger, D. G., Y. Ye, et al. (1984), *Linear and nonlinear programming*, vol. 2, Springer.

Magnan, P. (2003), Detection of visible photons in CCD and CMOS: A comparative view, *Nuclear Instruments and Methods in Physics Research Section A: Accelerators, Spectrometers, Detectors and Associated Equipment*, *504*(1-3), 199–212.

Mauersberger, K. (1981), Measurement of heavy ozone in the stratosphere, *Geophysical Research Letters*, *8*(8), 935–937.

Mehrparvar, A., D. Pignatelli, J. Carnahan, R. Munakat, W. Lan, A. Toorian, A. Hutputanasin, and S. Lee (2014), Cubesat design specification rev. 13, *The CubeSat Program, Cal Poly San Luis Obispo, US*, *1*(2).

Melo, S. M., I. C. McDade, and H. Takahashi (2001), Atomic oxygen density profiles from ground-based nightglow measurements at 23 S, *Journal of Geophysical Research: Atmospheres*, *106*(D14), 15,377–15,384.

Norton, C. D., S. Pellegrino, M. Johnson, M. Arya, J. Steeves, S. Kulkarni, and C. D. Martin (2014), Small satellites: A revolution in space science.

Offermann, D. (1987), The MAP/GLOBUS campaign 1983: Introduction, *Planetary and space science*, *35*(5), 515–524.

Olschewski, F., M. Kaufmann, K. Mantel, T. Neubert, R. Heinz, M. Riese, and R. Koppmann (2019), Atmocube A1: Airglow measurements in the mesosphere and lower thermosphere by spatial heterodyne interferometry, *Journal of Applied Remote Sensing*, *13*(2), 1 – 12 – 12, doi:10.1117/1.JRS.13.024501.

Ortland, D., P. Hays, W. Skinner, and J.-H. Yee (1998), Remote sensing of mesospheric temperature and O_2 ($^1\sum$) band volume emission rates with the high-resolution doppler imager, *Journal of Geophysical Research: Atmospheres*, *103*(D2), 1821–1835.

Pérot, K., A. Hauchecorne, F. Montmessin, J.-L. Bertaux, L. Blanot, F. Dalaudier, D. Fussen, and E. Kyrölä (2010), First climatology of polar mesospheric clouds from GOMOS/ENVISAT stellar occultation instrument, *Atmospheric Chemistry and Physics*, *10*(6), 2723–2735.

Pisarenko, V. F. (1973), The retrieval of harmonics from a covariance function, *Geophysical Journal International*, *33*(3), 347–366.

Rader, C., and N. Brenner (1976), A new principle for fast fourier transformation, *IEEE Transactions on Acoustics, Speech, and Signal Processing*, *24*(3), 264–266.

Riese, M., H. Oelhaf, P. Preusse, J. Blank, M. Ern, F. Friedl-Vallon, H. Fischer, T. Guggenmoser, M. Höpfner, P. Hoor, et al. (2014), Gimballed limb observer for radiance imaging of the atmosphere (GLORIA) scientific objectives, *Atmospheric measurement techniques*, *7*(7), 1915–1928.

Roesler, F., and J. Harlander (1990), Spatial heterodyne spectroscopy-interferometric performance at any wavelength without scanning, in *Optical spectroscopic instrumentation and techniques for the 1990s-Applications in astronomy, chemistry, and physics*, vol. 1318, pp. 234–243.

Roy, R., and T. Kailath (1989), ESPRIT-estimation of signal parameters via rotational invariance techniques, *IEEE Transactions on Acoustics, Speech, and Signal Processing*, *37*(7), 984–995.

Russell, J. M., M. G. Mlynczak, L. L. Gordley, J. J. Tansock, and R. W. Esplin (1999), Overview of the saber experiment and preliminary calibration results, in *Optical Spectroscopic Techniques and Instrumentation for Atmospheric and Space Research III*, vol. 3756, pp. 277–289, International Society for Optics and Photonics.

San Choi, K., E. Y. Lam, and K. K. Wong (2006), Automatic source camera identification using the intrinsic lens radial distortion, *Optics express*, *14*(24), 11,551–11,565.

Schmidt, R. (1986), Multiple emitter location and signal parameter estimation, *IEEE transactions on antennas and propagation*, *34*(3), 276–280.

Selva, D., and D. Krejci (2012), A survey and assessment of the capabilities of cubesats for earth observation, *Acta Astronautica*, *74*, 50–68.

Sheese, P., E. Llewellyn, R. Gattinger, A. Bourassa, D. Degenstein, N. Lloyd, and I. McDade (2010), Temperatures in the upper mesosphere and lower thermosphere from OSIRIS observations of O_2 A-band emission spectra, *Canadian Journal of Physics*, *88*(12), 919–925.

Shepherd, G. G., G. Thuillier, W. Gault, B. Solheim, C. Hersom, J. Alunni, J.-F. Brun, S. Brune, P. Charlot, L. Cogger, et al. (1993), WINDII, the wind imaging interferometer on the upper atmosphere research satellite, *Journal of Geophysical Research: Atmospheres*, *98*(D6), 10,725–10,750.

Smit, H. G., W. Straeter, B. J. Johnson, S. J. Oltmans, J. Davies, D. W. Tarasick, B. Hoegger, R. Stubi, F. J. Schmidlin, T. Northam, et al. (2007), Assessment of the performance of ECC-ozonesondes under quasi-flight conditions in the environmental simulation chamber: Insights from the Juelich Ozone Sonde

Intercomparison Experiment (JOSIE), *Journal of Geophysical Research: Atmospheres*, *112*(D19).

Smith, J. O., and X. Serra (1987), Parshl: An analysis/synthesis program for non-harmonic sounds based on a sinusoidal representation, in *Proceedings of the 1987 International Computer Music Conference, ICMC; 1987 Aug 23-26; Champaign/Urbana, Illinois.[Michigan]: Michigan Publishing; 1987. p. 290-7.*, International Computer Music Conference.

Song, R., M. Kaufmann, J. Ungermann, M. Ern, G. Liu, and M. Riese (2017), Tomographic reconstruction of atmospheric gravity wave parameters from airglow observations, *Atmospheric Measurement Techniques*, *10*(12), 4601–4612.

Song, R., M. Kaufmann, M. Ern, J. Ungermann, G. Liu, and M. Riese (2018), Three-dimensional tomographic reconstruction of atmospheric gravity waves in the mesosphere and lower thermosphere (mlt), *Atmospheric Measurement Techniques*, *11*(5), 3161–3175.

Srour, J., R. Hartmann, and K. Kitazaki (1986), Permanent damage produced by single proton interactions in silicon devices, *IEEE Transactions on Nuclear Science*, *33*(6), 1597–1604.

Stark, B., B. Noelting, H. Jahn, and K. Andert (1992), Method for determining the electron number in charge-coupled measurement devices, *Optical Engineering*, *31*(4), 852–857.

Stoica, P., and A. Nehorai (1989), MUSIC, maximum likelihood, and Cramer-rao bound, *IEEE Transactions on Acoustics, Speech, and Signal Processing*, *37*(5), 720–741.

Swindlehurst, A. L., P. Stoica, and M. Jansson (2001), Exploiting arrays with multiple invariances using MUSIC and MODE, *IEEE Transactions on Signal Processing*, *49*(11), 2511–2521.

Tsai, R. (1987), A versatile camera calibration technique for high-accuracy 3D machine vision metrology using off-the-shelf TV cameras and lenses, *IEEE Journal on Robotics and Automation*, *3*(4), 323–344.

Tufts, D., A. Kot, and R. Vaccaro (1988), The threshold analysis of SVD-based algorithms, in *Acoustics, Speech, and Signal Processing, 1988. ICASSP-88., 1988 International Conference on*, pp. 2416–2419, IEEE.

Ungermann, J., J. Blank, J. Lotz, K. Leppkes, L. Hoffmann, T. Guggenmoser, M. Kaufmann, P. Preusse, U. Naumann, and M. Riese (2011), A 3-D tomographic retrieval approach with advection compensation for the air-borne limb-imager GLORIA, *Atmospheric Measurement Techniques*, *4*(11), 2509–2529.

Wang, C. (2010), New chains of space weather monitoring stations in china, *Space Weather*, *8*(8).

Zhang, Z. (2000), A flexible new technique for camera calibration, *IEEE Transactions on pattern analysis and machine intelligence*, *22*(11), 1330–1334.

Band / Volume 454
Reformierung von BtL-Kraftstoffen für die HT-PEFC in luftfahrttechnischen Systemen
C. Wilbrand (2019), IV, 312 pp
ISBN: 978-3-95806-387-7

Band / Volume 455
Entwicklung von thermischen Spritzprozessen für fortschrittliche Schutz- und Funktionsschichten
G. Mauer (2019), vi, 57 pp
ISBN: 978-3-95806-388-4

Band / Volume 456
Columnar Structured Thermal Barrier Coatings Deposited by Axial Suspension Plasma Spraying
D. Zhou (2019), VI, 126 pp
ISBN: 978-3-95806-391-4

Band / Volume 457
Modellierung zeitlich aufgelöster Ladeenergienachfragen von batterie-elektrischen Fahrzeugen und deren Abbildung in einem Energiesystemmodell
J. F. Linßen (2019), VIII, 189 pp
ISBN: 978-3-95806-395-2

Band / Volume 458
Synthesis and Analysis of Spinel Cathode Materials for High Voltage Solid-State Lithium Batteries
A. Windmüller (2019), iv, 142 pp
ISBN: 978-3-95806-396-9

Band / Volume 459
Monazite-type ceramics as nuclear waste form: Crystal structure, microstructure and properties
Y. Arinicheva (2019), 194 pp
ISBN: 978-3-95806-397-6

Band / Volume 460
Coupling a Solid Oxide Fuel Cell with a Biomass Gasifier: Degradation Mechanisms and Alternative Anode Materials
H. Jeong (2019), II, 112 pp
ISBN: 978-3-95806-398-3

Band / Volume 461
Model-based Source Partitioning of Eddy Covariance Flux Measurements
A. Klosterhalfen (2019), XVI, 132 pp
ISBN: 978-3-95806-401-0

Band / Volume 462
Entwicklung von großflächigen PECVD-Prozessen zur kontrollierten, homogenen Abscheidung dünner Siliziumschichten für die Photovoltaik
B. O. Grootoonk (2019), 154 pp
ISBN: 978-3-95806-402-7

Band / Volume 463
Simulation of Transport Processes through an Asymmetric Gas Separation Membrane
U. V. Unije (2019), xiv, 101 pp
ISBN: 978-3-95806-403-4

Band / Volume 464
Development, calibration and deployment of an airborne chemical ionization mass spectrometer for trace gas measurements
T. Khattatov (2019), 14, 125 pp
ISBN: 978-3-95806-404-1

Band / Volume 465
IEK-3 Report 2019 – Maßgeschneiderte Energieumwandlung für nachhaltige Kraftstoffe
D. Stolten, B. Emonts (Eds.) (2019), 171 pp
ISBN: 978-3-95806-410-2

Band / Volume 466
Initialinfrastruktur für Wasserstoffmobilität auf Basis von Flotten
F. Grüger (2019), V, 209 pp
ISBN: 978-3-95806-413-3

Band / Volume 467
Techno-ökonomische Analyse alternativer Wasserstoffinfrastruktur
M. E. Reuß (2019), 205 pp
ISBN: 978-3-95806-414-0

Band / Volume 468
Study on a miniaturized satellite payload for atmospheric temperature measurements
J. Liu (2019), 153 pp
ISBN: 978-3-95806-415-7

Energie & Umwelt / Energy & Environment
Band / Volume 468
ISBN 978-3-95806-415-7

Mitglied der Helmholtz-Gemeinschaft

JÜLICH
Forschungszentrum